ERDC/GSL TR-01-6

Geotechnical and Structures
Laboratory

**US Army Corps
of Engineers**®
Engineer Research and
Development Center

Dynamic Response of Brittle Materials from Penetration and Split Hopkinson Pressure Bar Experiments

Danny J. Frew

May 2001

20010809 123

The contents of this report are not to be used for advertising, publication, or promotional purposes. Citation of trade names does not constitute an official endorsement or approval of the use of such commercial products.

The findings of this report are not to be construed as an official Department of the Army position, unless so designated by other authorized documents.

Dynamic Response of Brittle Materials from Penetration and Split Hopkinson Pressure Bar Experiments

by   Danny J. Frew

Geotechnical and Structures Laboratory
U.S. Army Engineer Research and Development Center
3909 Halls Ferry Road
Vicksburg, MS 39180-6199

Final report

Approved for public release; distribution is unlimited

TABLE OF CONTENTS

iv

APPENDIX

LIST OF TABLES

LIST OF FIGURES

PREFACE

CHAPTER 1

INTRODUCTION

This research program began with a suite of penetration experiments into Indiana limestone targets with ogive-nose, steel rod projectiles. Three sets of experiments were conducted with geometrically similar projectiles that had length-to-diameter ratios of ten and 7.1, 12.7, and 25.4-mm-diameters. A comparison of these data and a previously developed analytical penetration model (Forrestal, Altman, Cargile, and Hanchak, 1994) showed that the target resistance depended on the projectile shank diameter. This scale effect was observed by others (Warren and Forrestal, 1998) and strongly suggested a strain-rate dependence of the target material strength. Data from these penetration experiments and discussion of the results are presented in Chapter 2.

In order to study the strain-rate effect of Indiana limestone, improved experimental and analytic techniques for the dynamic testing of brittle materials in uniaxial compression were required. As a first step, a split Hopkinson pressure bar (SHPB) or Kolsky bar facility was designed and built for dynamic compression testing of brittle materials. In Chapter 3, the theory and experimental set-up for the SHPB apparatus is described, preliminary results from a conventional SHPB experiment are presented, and the critical experimental modifications that are necessary for valid tests with brittle materials are discussed. Brittle samples loaded dynamically with a SHPB apparatus should be in dynamic stress equilibrium and have a nearly constant strain rate over the test duration.

In Chapter 4, two analytic models that predict the evolutionary process for sample equilibrium and constant strain rate in brittle materials that have a linear stress-strain response to failure are presented. These models and subsequent experiments show that a ramp stress pulse in the incident bar is required to obtain sample equilibrium and constant strain rate over most of the duration of the experiment. The first model assumes that the sample is in dynamic stress equilibrium and predicts strain and strain-rate versus time. The second model uses a wave propagation analysis on the interaction of the sample with the incident and transmission bars to predict the stress-time histories on either side of the sample. Model predictions for an Indiana limestone and a machineable glass ceramic, Macor are presented in later chapters and are shown to be in good agreement with data.

In Chapter 5, pulse shaping techniques that are used to shape the incident stress pulse and obtain valid compressive stress-strain data for brittle materials with the modified SHPB apparatus are presented. The conventional SHPB apparatus is modified by placing a thin disk of annealed or hard C11000 copper on the impact surface of the incident bar. After impact by the striker bar, the copper disk deforms plastically and spreads the pulse in the incident bar. An analytic model and data show that a wide variety of incident strain pulses can be produced by varying the geometry of the copper disks and the length and striking velocity of the striker bar. Model predictions are in good agreement with measurements.

Another benefit to pulse shaping is that the loading durations can be controlled such that samples are unloaded just prior to catastrophic failure. Thus, intact samples that experience strains beyond the elastic region and post-peak stresses can be retrieved for

microstructural evaluation. This soft-recovery loading technique is demonstrated with experiments on an Indiana limestone and a machineable glass ceramic material, Macor.

In Chapter 6, unconfined compressive strength data on Indiana limestone specimens for strain rates between 10^{-5} to 3×10^2 s^{-1} are presented. The dynamic unconfined compressive strength for this material is about double that obtained from the quasi-static experiments. Possible mechanisms for this large strength enhancement are discussed. In addition, the versatility of these methods are shown in Chapter 7 where experimental and model results are presented for the machineable glass ceramic, Macor.

In Chapter 8, the results of this thesis are summarized.

CHAPTER 2

PENETRATION EXPERIMENTS WITH LIMESTONE TARGETS AND OGIVE-
NOSE STEEL PROJECTILES

2.1   BACKGROUND

Several authors have written review articles that discuss the many analytical,
computational, and experimental methods used to study the broad field of penetration
mechanics (Backman and Goldsmith, 1978; Anderson and Bodner, 1988; Hohler and
Stilp, 1990; Recht, 1990; Corbett, Reid, and Johnson, 1996). The responses of the
projectiles and targets depend strongly on the problem geometry, materials, and impact
conditions. Because many penetration mechanisms are possible, experimental
observations usually precede and guide analytical or computational models. For this
study with limestone targets, post-test target observations showed a conical entry crater
with a depth of two or more projectile diameters followed by a circular penetration
channel or tunnel with nearly the projectile diameter. For recent penetration studies with
6061-T6511 aluminum targets (Warren and Forrestal, 1998; Piekutowski, Forrestal,
Poormon, and Warren, 1999), post-test radiographs of the penetration channels could be
obtained. However, we made post-test observations of the limestone penetration
channels only after the targets were split with the techniques used by stone masons. The
projectiles recovered from the targets had small mass losses due to abrasion, but the
overall nose shapes prior to and after penetration looked very similar. We previously
observed similar post-test, target channels and abraded projectiles with our studies on

concrete targets (Forrestal, Frew, Hanchak, and Brar, 1996; Frew, Hanchak, Green, and Forrestal, 1998). However, the concrete targets abraded the nose tips more severely than the limestone targets.

The limestone targets used in this study were quarried and cut by the Elliot Stone Company, Bedford, IN. In the rock mechanics literature, this particular limestone is often called Salem, Indiana, or Bedford limestone. For this study, we conducted unconfined compressive tests and some triaxial compression tests on samples cored from representative blocks. Material properties from our targets are nearly the same as those reported by Fossum, Senseny, Pfeifle, and Mellegard (1995).

Based on data sets from three projectile scales, we developed an empirical penetration equation that describes the target by its density and an empirical strength constant determined from penetration depth versus striking velocity data. While this methodology provides an accurate and convenient engineering equation, the detailed response mechanisms for the target are not modeled. We are not aware of any rigorous target models for rock penetration problems, but Lagrangian computational models that use adaptive meshing techniques (Ortiz, 1996; Camacho and Ortiz, 1997) and particle dynamic simulations (Mastilovic and Krajcinovic, 1999) have shown promise for brittle targets. Detailed computational approaches that model target responses also require a broad array of quasi-static and dynamic material properties data. For limestone, examples of some materials experiments and data include (1) quasi-static, triaxial compression experiments (Fossum, Senseny, Pfeifle, and Mellegard, 1995), (2) split Hopkinson bar experiments (Green and Perkins, 1968; Lindholm, Yeakley, and Nagy, 1974; and Lipkin, Grady, and Campbell, 1977), (3) plane shock wave studies (Larson and

Anderson, 1979), (4) dynamic tensile failure with planar-impact techniques (Grady and Hollenbach, 1979; Ahrens and Rubin, 1993), and (5) compression-shear loading with plate impact experiments (Aidun and Gupta, 1995). Data from other experimental techniques may also be required for a careful target analysis.

Next, we describe the penetration model, discuss the experiments, and present our results and conclusions.

2.2   PENETRATION MODEL

For both limestone and concrete targets, post-test observations showed a conical entry crater with a depth of two or more projectile diameters followed by a circular channel or tunnel with nearly the projectile diameter. The limestone penetration equations are similar to the previously published concrete penetration equations. From Forrestal, Altman, Cargile, and Hanchak (1994), depth of penetration P for an ogive-nose projectile and a concrete target is given by

$$P = \frac{m}{2\pi a^2 \rho N} \ln\left(1 + \frac{N\rho V_1^2}{R}\right) + 4a, \text{ for } P > 4a \tag{2.1a}$$

$$N = \frac{8\psi - 1}{24\psi^2}, \quad V_1^2 = \frac{mV_s^2 - 4\pi a^3 R}{m + 4\pi a^3 N\rho} \tag{2.1b}$$

in which the ogive-nose rod projectile is described by mass m, shank radius a, and caliber-radius-head ψ. The target is described by density ρ and the target strength constant R. The strength constant is determined from

$$R = \frac{N\rho V_s^2}{\left(1 + \dfrac{4\pi a^3 N\rho}{m}\right)\exp\left[\dfrac{2\pi a^2 (P - 4a)N\rho}{m}\right] - 1} \qquad (2.2)$$

where V_s is striking velocity. For a set of experiments, we hold all parameters constant and vary striking velocity. From each experiment, we measure striking velocity V_s and penetration depth P, so R can be determined from eq (2.2) for each experiment. We then take the average value of R from each experiment in the data set and compare the prediction from eq (2.1) with the individual measured values of V_s and P. For the concrete penetration equations (Forrestal, Altman, Cargile, and Hanchak, 1994), we found it convenient to let $R = S f_c'$ where f_c' is the unconfined compressive strength of the concrete target and S is a dimensionless parameter.

Frew, Hanchak, Green, and Forrestal (1998) showed that for concrete targets with nearly equal unconfined compressive strengths, ogive-nose steel rod projectiles had nearly the same constant value of $R = S f_c'$ for 20.3- and 30.5-mm-diameter projectiles with a length-to-diameter ratio of ten. However, for this study with limestone targets, ogive-nose steel rod projectiles with 7.1, 12.7, and 25.4-mm-diameters and a length-to-diameter of ten have values of R = 913, 787, and 693 MPa, respectively. Thus, the target

resistance decreases as projectile shank diameter increases. Warren and Forrestal (1998) studied the effects of strain hardening and strain-rate effects on the penetration of aluminum targets. Results from that study show the same dependence of projectile diameter on target strength. Guided by the models in Warren and Forrestal (1998), we found that for these limestone targets

$$R = K + k(2a_o / 2a) \qquad (2.3)$$

in which K and k are constants obtained from data fits, $2a_o$ is a reference projectile diameter, and $2a$ is the projectile diameter. We show later that with $K = 607$ MPa, $k = 86$ MPa, and $2a_o = 25.4$ mm, we recover the measured values of R for each of the three data sets.

In summary, the procedure used to calculate R from penetration depth data for a fixed projectile is the same for concrete or limestone targets. However, for limestone targets, R depends on the projectile shank diameter. Thus, we can use the penetration eqs (2.1a) and (2.1b) for limestone when R is given by eq (2.3).

2.3   EXPERIMENTS

We conducted three sets of penetration experiments (a total of 30 experiments) with ogive-nose, steel rod projectiles and limestone targets. All projectiles had a total length-to-diameter ratio of ten and 3.0 caliber-radius-head (CRH) nose shapes. The shank

diameters and masses for each of the three sets of experiments were 7.1 mm, 0.020 kg; 12.7 mm, 0.117 kg; and 25.4 mm, 0.931 kg.

2.3.1   Limestone Targets

The limestone targets were quarried and cut by the Elliot Stone Company of Bedford, Indiana. We obtained the targets in three batches from nearby sites. Nominal material properties for the three target batches given in Table 2.1 show minimal variations among the batches.

Table 2.1 Nominal material properties for the limestone targets

Batch	Density ρ (Mg/m^3)	Porosity η (%)	Unconfined Strength σ_{cf}(MPa)
1	2.32	14.4	60
3	2.30	15.1	63
4	2.31	14.8	61

Figure 2.1 shows data from triaxial material tests for samples from batch 3. For these experiments a 51-mm-diameter, 108-mm-long cylinder of limestone is loaded with two stress paths: isotropic compression followed by triaxial shear (Farmer, 1983, and Jaeger and Cook, 1979). The limestone cylinders are loaded with axial stress σ_a and radial stress σ_r. For the triaxial data shown in Fig. 2.1, the limestone cylinders are first loaded with isotropic compression, $\sigma_a = \sigma_r$, and then the axial stress σ_a is increased while the radial stress σ_r is held constant. Figure 2.1 shows plots of principal stress difference (true stress), $\sigma_a - \sigma_r$, versus axial strain (engineering strain) for $\sigma_r = 20$, 50, and 100 MPa.

For a radial stress or confining pressure of 20 MPa, the principal stress difference, $\sigma_a - \sigma_r$, reaches a maximum at about 96 MPa, and then the sample fractures. For radial stresses of 50 and 100 MPa, the sample deforms with a ductile response. The brittle to ductile transition confining pressure is about 50 MPa.
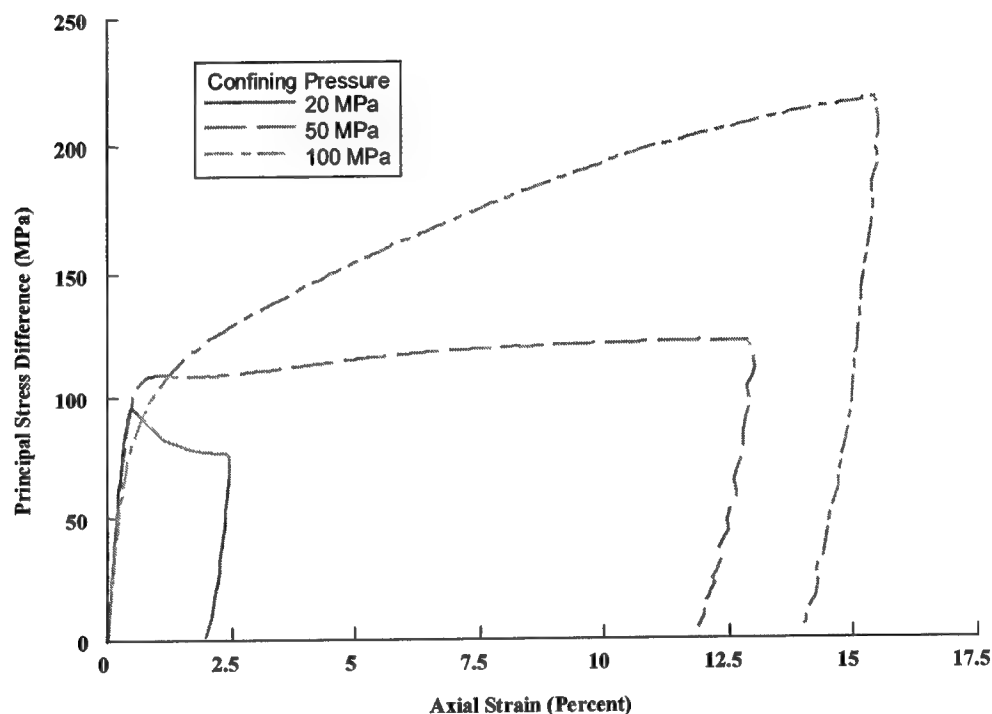
Figure 2.1 Batch 3 limestone triaxial compression data

2.3.2   12.7-mm-Diameter, 0.117 kg, 3.0 CRH Projectiles

Our first set of experiments was conducted with steel projectiles machined from 4340 R_c 45 (Brown, Mindlin, and Ho, 1996) round stock. Figure 2.2 shows the projectile geometry, and for this set of experiments $2a = 12.7$ mm, $L = 106$ mm, and $l = 21$ mm. The limestone target impact surface was 0.51-m-square, and the target lengths and other

data are given in Table 2.2. The sides and bottom of the targets were surrounded by 0.10-m-thick concrete placed between a steel form and the limestone. Six unconfined compressive tests were conducted with 51-mm-diameter, 107-mm-long samples cored from a representative limestone block from Batch 1 and the average strength was $\sigma_{cf} =$ 60 MPa.
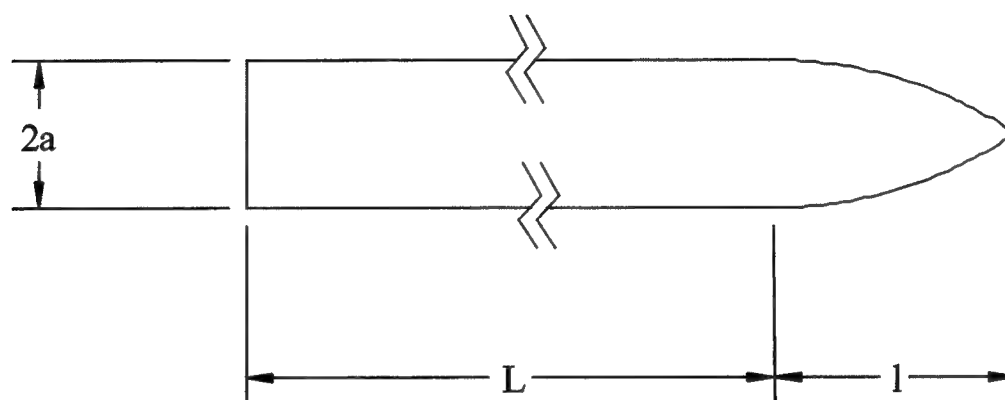
Figure 2.2 Projectile geometries

Table 2.2 Penetration data for the 12.7-mm-diameter, 0.117 kg projectiles. For pitch and yaw, D=down, U=up, R=right, L=left

Shot, Batch Number	Target Length (m)	Striking Velocity (m/s)	Pitch Yaw (degrees)	Penetration Depth (m)	Projectile Mass Loss (%)	R (GPa)
1-0370, 1	0.61	459	1.9D, 3.0L	0.141	0.16	0.733
1-0371, 1	0.61	608	1.0U, 1.0R	0.232	0.24	0.734
1-0372, 1	0.91	853	0, 0	0.362	0.96	0.875
1-0377, 1	0.91	956	0, 0.3L	0.523	1.29	0.719
1-0373, 1	0.91	1134	1.0U, 1.9R	0.562	2.59	0.930
1-0376, 1	1.22	1269	0, 0	0.812	3.87	0.745
1-0375, 1	1.22	1404	0, 0.7R	0.924	5.25	0.775
1-0374, 1	1.22	1502	0.7U, 0	1.017	5.90	0.783

A 32-mm-diameter powder gun launched the 0.117 kg projectiles to the striking velocities recorded in Table 2.2. An additional experiment was conducted at V_s = 1605 m/s, but the trajectory was curved and the projectile exited the side of the target at a depth of about 0.65 m. The projectiles were fitted with sabots and obturators that separated from the projectiles prior to impact. Four laser diode systems measured striking velocities and orthogonal radiographs measured pitch and yaw angles. The target resistance R was calculated from eq (2.2) for each experiment and recorded in Table 2.2. The average target resistance parameter for this set of experiments is R = 787 MPa.

2.3.3   7.1-mm-Diameter, 0.020 kg, 3.0 CRH Projectiles

Our second set of experiments was conducted with steel projectiles machined from both 4340 R_c 45 and Aer Met 100 R_c 53 (Dahl, 1991) round stock. Figure 2.2 shows the projectile geometry, and for this set of experiments $2a$ = 7.11 mm, L = 59.3 mm, and l = 11.8 mm. A 20-mm-powder gun launched the 0.020 kg projectiles to striking velocities of 1230 m/s. For the larger striking velocities recorded in Table 2.3, a two-stage, 50/20 mm, light-gas gun launched the projectiles. The same target geometries and ballistics measurements as those described for the 12.7-mm-diameter, 0.117 kg projectiles were used for this set of experiments.

Table 2.3 Penetration data for the 7.1-mm-diameter, 4340 (HRC = 44-46) or Aer Met 100 (HRC = 53) (Shots 4-1847 and 4-1846), 0.0205 kg, 3.0 CRH projectiles. For pitch and yaw: D = down, U = up, R = right, L = left

Shot, Batch Number	Target Length (m)	Striking Velocity (m/s)	Pitch Yaw (degrees)	Penetration Depth (m)	Projectile Mass Loss (%)	R (GPa)	Compressive Strength σ_{cf} (MPa)
1-0422, 3	0.30	497	0, 0.75R	0.067	0.34	1.033	
1-0418, 3	0.61	597	0.5U, 0	0.105	0.34	0.895	64.7
1-0419, 3	0.61	787	0, 1.25R	0.165	0.78	0.937	
1-0420, 3	0.61	1037	0.75U, 0.5R	0.271	2.11	0.927	
4-1835, 3	1.02	1365	2.0D, 1.6R	0.430	4.90	0.926	58.2
4-1836, 3	1.02	1516	0.9U, 1.1R	0.516	7.34	0.903	
1-0439, 1	0.46	795	0.5U, 0	0.178	0.83	0.877	60.1
1-0440, 1	0.61	1060	0.25U, 0.5R	0.294	2.49	0.877	60.3
1-0441, 1	0.61	1230	0, 0.25R	0.392	3.76	0.837	55.7
4-1845, 1	1.02	1340	1.75D, 1.0L	0.437	4.84	0.870	57.5
4-1847, 3	1.02	1266	1.0D, 1.5R	0.379	4.59	0.925	63.8
4-1846, 3	1.02	1674	0.5U, 0	0.581	10.85	0.944	63.9

For this second set of experiments, we performed unconfined compressive tests on two samples cored from the targets. The compressive strengths listed in Table 2.3 are the average of two, unconfined compression tests conducted with 50-mm-diameter, 107-mm-long cores. In addition, we conducted penetration experiments from both Batch 1 and Batch 3 limestone targets to compare results from the two batches. We show later negligible differences in the penetration data from both batches. The average target resistance parameter for this set of experiments is R = 913 MPa.

We also conducted an experiment with a 4340 (HRC = 45) projectile at V_s = 1649 m/s. That projectile severely bent and turned within the target. Table 2.3 shows two experiments conducted with Aer Met 100 (HRC = 53) projectiles. Shot 4-1846 with a striking velocity of 1674 m/s had a nearly straight trajectory. We then conducted experiments at V_s = 1749, 1826, and 1863 m/s with Aer Met 100 (HRC = 53) projectiles

and these projectiles severely bent and turned within the targets. Piekutowski, Forrestal, Poormon, and Warren (1999) discusses in detail the better performance of the Aer Met 100 HRC 53 projectiles.

2.3.4 The 25.4-mm-Diameter, 0.931 kg, 3.0 CRH Projectiles

Our third set of experiments was conducted with steel projectiles machined from 4340 R_c 45 round stock. Figure 2.2 shows the projectile geometry, and for this set of experiments $2a = 25.4$ mm, $L = 212$ mm, and $l = 42$ mm. The limestone target impact surface was 1.02-m-square and the target lengths are given in Table 2.4. An 83-mm powder gun launched the 0.931 kg projectiles to the striking velocities recorded in Table 2.4. The same experimental methods used for the other data sets were also used to obtain the results given in Table 2.4. Data in Table 2.4 were limited to $V_s = 1177$ m/s because of the size and mass of the targets. The average value of R for this set of experiments was R = 693 MPa.

Table 2.4 Penetration data for the 25.4-mm-diameter, 4340 (HRC = 45–46), 0.931 kg, 3.0 CRH projectiles. For pitch and yaw: D = down, U = up, R = right, L = left

Shot, Batch Number	Target Length (m)	Striking Velocity (m/s)	Pitch Yaw (degrees)	Penetration Depth (m)	Projectile Mass Loss (%)	R (GPa)	Compressive Strength σ_{cf} (MPa)
LROD99-1, 4	0.61	407	0.4D, 0.5L	0.260	0.00	0.617	56.2
LROD99-2, 4	0.76	566	0.6U, 0	0.390	0.10	0.769	61.9
LROD99-3, 4	1.07	800	0.6D, 0.1L	0.790	0.30	0.693	66.7
LROD99-6, 4	1.52	917	–, 0.3R	1.020	1.10	0.681	59.8
LROD99-7, 4	1.98	1177	0, 0.3R	1.500	2.80	0.705	61.2

2.4   RESULTS AND DISCUSSION

As previously discussed, post-test target observation for the experiments summarized in Tables 2.2, 2.3, and 2.4 showed a conical entry crater with a depth of two or more projectile diameters followed by a circular penetration tunnel with nearly the projectile diameter. However, we made post-test observations only after the targets were split with the techniques used by stone masons. Figure 2.3 shows post-test photographs of the 25.4-mm-diameter projectiles, and mass losses are given in Table 2.4. These recovered projectiles lost mass due to abrasion, but the nose shapes prior to and after penetration have similar shapes. Post-test projectiles from the other data sets (Tables 2.2 and 2.3) had shapes similar to those shown in Fig. 2.3.

Figure 2.4 shows depth of penetration P versus striking velocity V_s for the data in Tables 2.2, 2.3, and 2.4. For the model, we use the average value of R calculated from eq (2.2) for the experiments in each data set. For the 7.1, 12.7, and 25.4-mm-diameter projectiles the average target resistance parameter is R = 913, 787, and 693 MPa, respectively. As discussed in section 2.2, these diameter dependent results suggest a strain-rate effect for the target resistance. For projectile diameters not tested in this study, we recommend eq (2.3) be used to calculate R. Equation (2.3) with $K = 607$ MPa, $k = 86$ MPa, and $2a_o = 25.4$ mm recover the measured values of R from each of the three data sets. We hypothesize that the penetration eqs (2.1, 2.2, and 2.3) for this limestone target will be reasonably accurate for larger scale projectiles, but data from much more expensive field tests with larger diameter projectiles must be obtained to confirm our hypothesis.

As previously discussed, our current penetration model contains a target strength constant that is determined from penetration depth versus striking velocity data. Thus, the detailed response mechanisms for the target are not modeled. As a first step towards providing a mechanics based understanding of the target response, a new split Hopkinson pressure bar (SHPB) facility was designed and built to study the dynamic behavior of brittle materials. The remainder of this research will be devoted towards developing the appropriate experimental methods for testing brittle materials, such as limestone, with the SHPB technique. In addition, dynamic stress-strain and failure data for brittle materials over a broad range of strain rates will be presented.
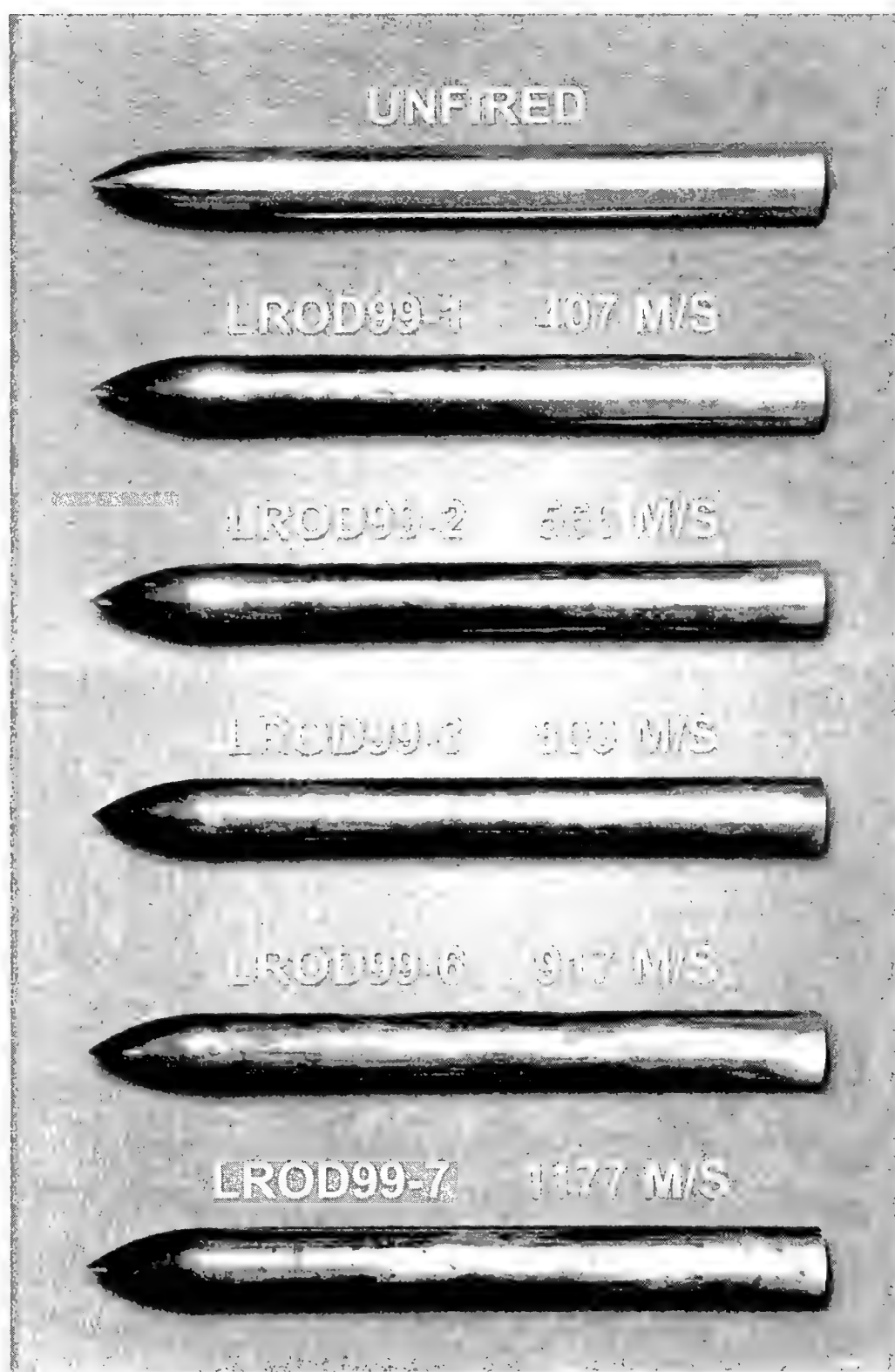
Figure 2.3 Post-test photographs of the 25.4-mm-diameter projectiles
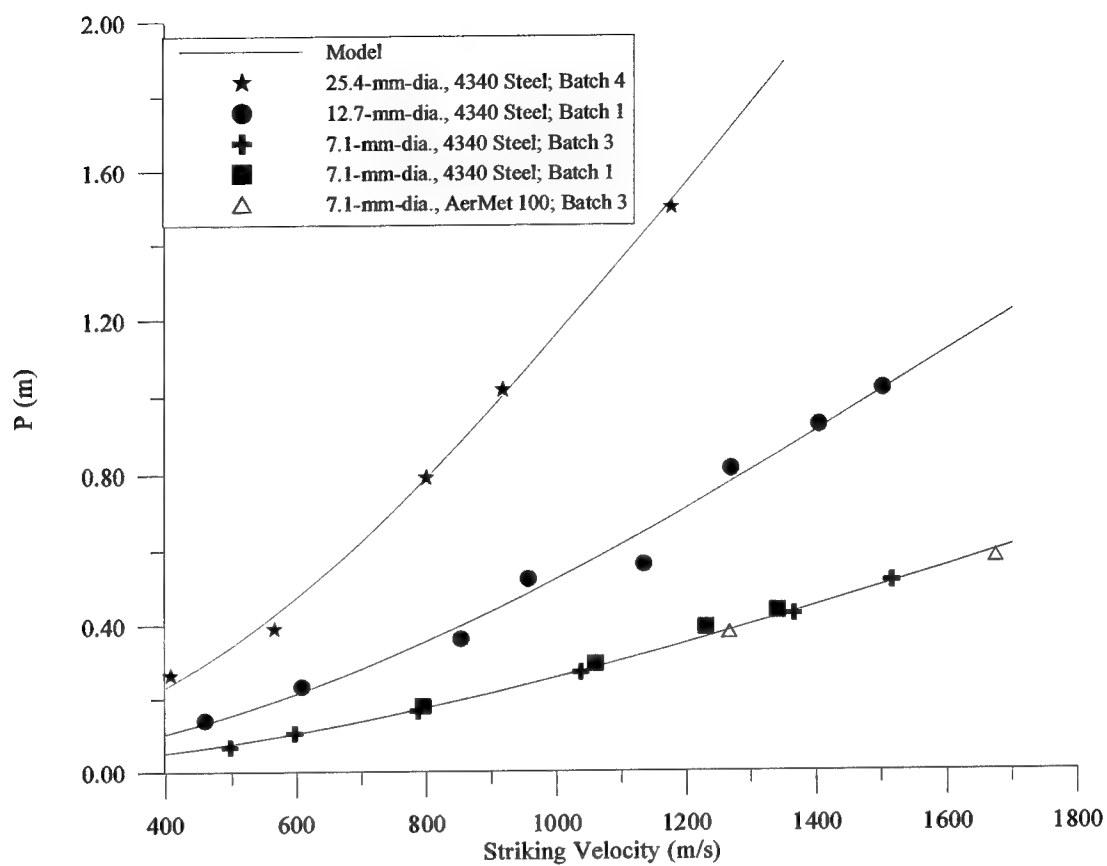
Figure 2.4 Data and model predictions for limestone targets

CHAPTER 3

SPLIT HOPKINSON PRESSURE BAR OR KOLSKY BAR

3.1   BACKGROUND

The split Hopkinson pressure bar (SHPB) technique originally developed by Kolsky (1949, 1963) has been used by many investigators to obtain dynamic compression properties of solid materials.   The evolution of this experimental method and recent advances are discussed by Lindolm (1964), Nicholas (1982), Follansbee (1985), Nemat-Nasser, Isaacs, and Starrett (1991), Ramesh and Narasimhan (1996), Gray (1999), and Gray and Blumenthal (1999). This technique has mostly been used to study the plastic flow stress of metals that undergo large strains at strain rates between $10^2 - 10^4$ s^{-1}. As discussed by Yadav, Chichili, and Ramesh (1995), data for the compressive flow stress of metals are typically obtained for strains larger than a few percent because the technique is not capable of measuring the elastic and early yield behavior. By contrast, most of the material behavior of interest for relatively brittle materials such as ceramics and rocks occurs at strains less than about 1.0 percent.

This chapter discusses elastic wave propagation in long cylindrical bars, describes the split Hopkinson pressure bar (SHPB) technique and experimental set-up, shows preliminary results from a conventional SHPB experiment with a limestone specimen, and discusses critical experimental modifications to the conventional SHPB apparatus that are necessary for valid tests with brittle materials.

3.2   ONE-DIMENSIONAL STRESS WAVES IN A BAR

Figure 3.1 shows a differential element of a long, cylindrical bar under a transient compressive load P. If we assume that the cross-sections of the element remain plane during loading and the lateral inertial effects are neglected, the equation of motion is given by

$$-\frac{\partial P}{\partial x}\Delta x = \rho A \Delta x \frac{\partial^2 u}{\partial t^2},$$

(3.1)

where A is the area of cross section and ρ the mass density of the bar. With the definitions of axial stress, axial strain, and Hooke's Law

$$\sigma_x = \frac{P}{A}$$

(3.2a)

$$\varepsilon_x = -\frac{\partial u}{\partial x}$$

(3.2b)

$$\sigma_x = E\varepsilon_x$$

(3.2c)

eq (3.1) can be written as

$$\rho \frac{\partial^2 u}{\partial t^2} = E \frac{\partial^2 u}{\partial x^2}.$$

(3.3)
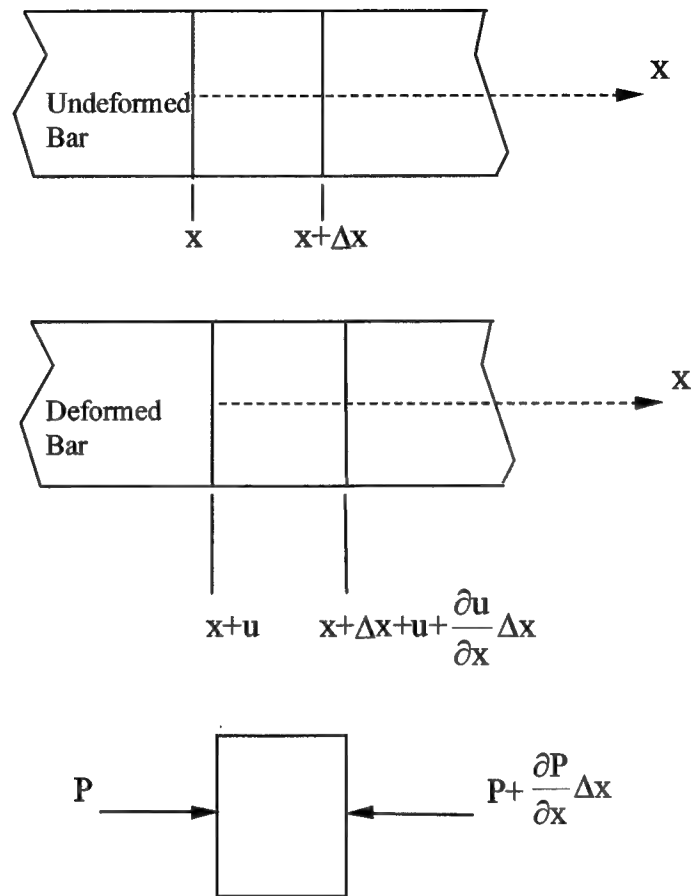
Figure 3.1 Differential element in cylindrical bar

Equation (3.3) reduces to the classical wave equation in displacement

$$\frac{\partial^2 u}{\partial t^2} = c_o^2 \frac{\partial^2 u}{\partial x^2}$$
(3.4)

by defining the one-dimensional wave speed in the bar as $c_o = (E / \rho)^{\frac{1}{2}}$. Equation (3.4)

has a general solution

$$u(x,t) = f(c_o t + x) + F(c_o t - x) \tag{3.5}$$

in which f and F are independent arbitrary functions for left and right travelling waves, respectively. For simplicity, we consider only a compressive stress wave travelling to the right in the bar. Differentiating eq (3.5) with respect to x yields

$$\frac{\partial u}{\partial x} = -F'(c_o t - x) \tag{3.6}$$

where $F'(c_o t - x)$ is the derivative with respect to the argument of F. Taking the derivative of eq (3.5) with respect to t yields

$$\frac{\partial u}{\partial t} = c_o F'(c_o t - x). \tag{3.7}$$

Substituting eqs (3.2) and (3.6) into eq (3.7) results in the following expression for the axial stress in the bar

$$\sigma_x = \frac{E}{c_o} \frac{\partial u}{\partial t} \tag{3.8}$$

which simplifies to

$$\sigma_x = \rho c_o \frac{\partial u}{\partial t}. \tag{3.9}$$

The term $\partial u/\partial t$ in eq (3.9) is the particle velocity v in the x-direction in the bar and should not be confused with the wave propagation velocity c_o. As their names state, v is the velocity of an individual particle in the medium, while c_o is the velocity at which waves propagate through the medium. Quantitatively, v is several orders of magnitude less than c_o. As shown in eq (3.9), the elementary theory of wave propagation yields a linear relationship between stress and particle velocity. Equation (3.9) will be used extensively throughout this work.

3.3   IMPACT OF TWO CYLINDRICAL BARS

In the previous section, the elementary equations for a stress pulse propagating through an elastic, circular bar were derived. The following analysis describes the compressive pulses that are created in a traditional SHPB, by the impact of two cylindrical bars. We build on these analyses in Chapter 5 to develop a pulse shaping model.

A short bar with length L, circular cross-section area A_{st}, mass density ρ_{st}, and bar wave speed c_{st} is propelled into one end of a longer, stationary bar having a cross-sectional area A_i, mass density ρ_i and bar wave speed c_i. The short bar is designated as the striker bar and the long bar the incident.

Figure 3.2a shows the striker bar travelling from left to right toward the free end of the stationary incident bar with some known rigid body velocity, V_o. Before the bars impact , $t < 0$, the bars are stress free and the particle velocity in the striker bar is equal to its rigid body velocity,

$$v = V_o .$$ (3.10)

After impact, $t > 0$, compressive waves travel into the striker and incident bars as shown in Fig. 3.2b. In this formulation, we define stress as positive in compression and particle velocities as positive when travelling to the right. Two conditions must be satisfied at the interface between the striker and incident bars. The first is the condition of continuity, which requires that the two bars to stay in contact during loading. If the interface velocity after impact is defined as v, then the particle velocity in the striker bar at the striker/ incident bar interface is

$$v = V_o - v_{st} .$$ (3.11)

The particle velocity in the incident bar at the striker/ incident bar interface is

$$v = v_i .$$ (3.12)

Combining eqs (3.12) and (3.11), yields

$$v_i = V_o - v_{st} .$$ (3.13)
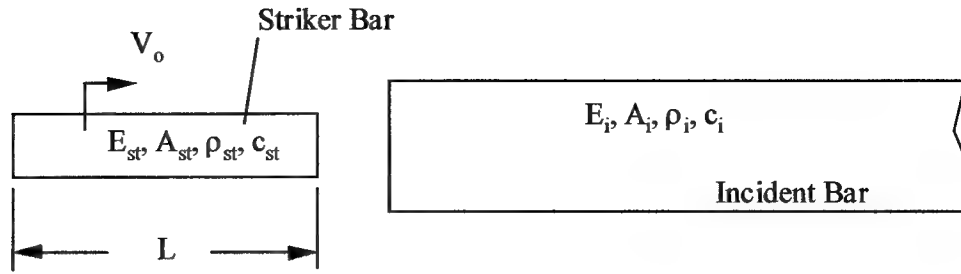
(Valid for t < 0)

a) Striker and incident bars before impact
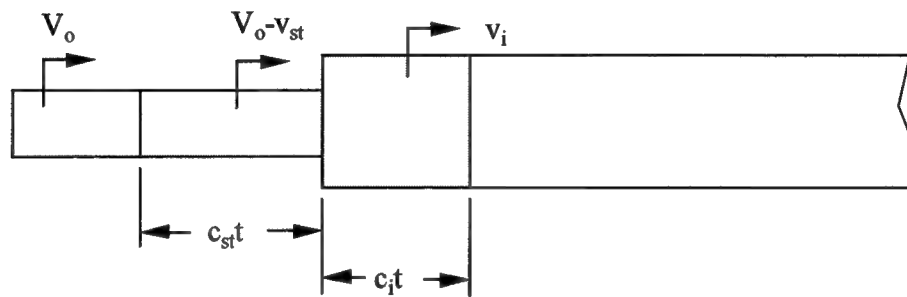
(Valid for $0 < t < L/c_{st}$)

b) Striker and incident bars after impact

Figure 3.2 Impact of two cylindrical bars

The second interface condition is that the forces across the interface must be equal, i.e.

$$P_{st} = P_i \tag{3.14}$$

where P_{st} and P_i are the axial compressive forces in the striker and incident bars, respectively.   Combining eqs (3.2), (3.9), (3.13), and (3.14) yields the following expressions for v_i and v_{st}

$$v_i = \frac{\rho_{st} A_{st} c_{st} V_o}{\rho_i A_i c_i + \rho_{st} A_{st} c_{st}},$$ (3.15a)

$$v_{st} = \frac{\rho_i A_i c_i V_o}{\rho_i A_i c_i + \rho_{st} A_{st} c_{st}}.$$ (3.15b)

From eq (3.9), the striker and incident bar stresses at the interface are given by

$$\sigma_{st} = \rho_{st} c_{st} \frac{\rho_i A_i c_i V_o}{\rho_i A_i c_i + \rho_{st} A_{st} c_{st}}$$ (3.16a)

$$\sigma_i = \rho_i c_i \frac{\rho_{st} A_{st} c_{st} V_o}{\rho_i A_i c_i + \rho_{st} A_{st} c_{st}}.$$ (3.16b)

If the two bars have the same material and cross-sectional area, the relationships simplify to

$$\rho_{st} c_{st} A_{st} = \rho_i c_i A_i = \rho c_o A$$ (3.17)

$$\sigma_{st} = \sigma_i = \sigma$$ (3.18)

$$v_{st} = v_i = \frac{1}{2} V_o$$ (3.19)

$$\sigma_{st} = \sigma_i = \frac{1}{2} \rho c_o V_o.$$ (3.20)

The stress pulse duration τ can be determined by examining the pressure pulse as it propagates through the striker bar. Figure 3.3a shows the impact stress wave as it travels from right to left in the striker bar at times, $0 < t < L/c_o$. As the leading edge of the pulse reaches the free end of the striker bar, at $t = L/c_o$, the entire bar will be travelling to the right with a particle velocity

$$v_{st} = \frac{1}{2}V_o.$$

(3.21)

Since the free end of the striker bar cannot support stress, a reflected tensile wave will travel from left to right in the striker bar. The superposition of these two stress waves satisfies the boundary condition at the free end.

The superposition of stresses at some later time, $L/c_o < t < 2L/c_o$, is illustrated in Fig. 3.3b. Figure 3.3b shows the left travelling compressive stress wave being cancelled by the right travelling tensile wave. When the tensile wave reaches the striker bar/ incident bar interface at $t = 2L/c_o$, the stress and the particle velocity of the entire striker bar will be zero. The striker bar will therefore separate from the incident bar because the impact surface of the incident bar has particle velocity v_i. The duration τ of the pressure pulse from the impact of two bars with the same impedance $\rho c_o A$ is therefore equal to two wave transit times in the striker bar,

$$\tau = \frac{2L}{c_o}.$$

(3.22)
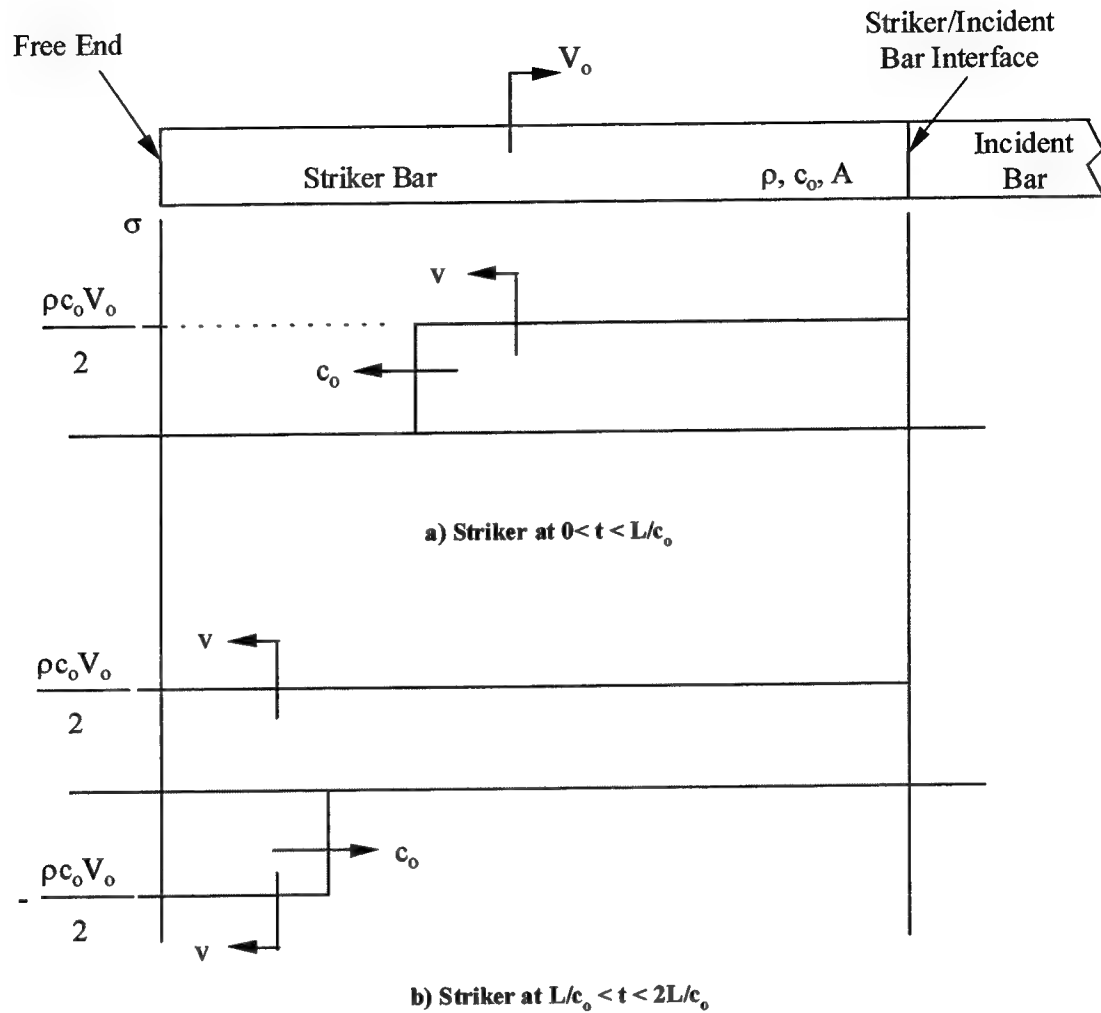
Figure 3.3 Stress waves propagating through striker bar

Thus for bars with the same impedances, a square, stress pulse propagates to the right at wave velocity c_o. As shown by eqs (3.20) and (3.22), the amplitude is controlled by the striking velocity and the duration is controlled by the striker bar length.

3.4   SPLIT HOPKINSON PRESSURE BAR TECHNIQUE

As shown in Fig. 3.4, a conventional split Hopkinson pressure bar (SHPB) consists of a striker bar, an incident bar, a transmission bar, and a sample placed between the incident and transmission bars. A gas gun launches the striker bar at the incident bar and that impact causes an elastic compression wave to travel in the incident bar towards the sample. When the impedance of the sample is less than that of the bars, an elastic tensile wave (Graff (1975)) is reflected into the incident bar and an elastic compression wave is transmitted into the transmission bar through the specimen. If the elastic stress pulses in the bars are nondispersive, the elementary theory for wave propagation in bars can be used to calculate the sample response from measurements taken with strain gages mounted on the incident and transmission bars. Strain gages mounted on the incident bar measure the incident ε_i and reflected ε_r strain pulses, and strain gages mounted on the transmission bar measure the transmitted ε_t strain pulse. Nicholas (1982), Follansbee (1985), and Gray (1999) present equations that describe the sample response in terms of the measured strain signals.

For this study the incident and transmission bars were made from the same material with equal cross-sectional areas. As shown in Fig. 3.1, the incident and transmission bars have density ρ, Young's modulus E, bar wave speed c, and cross-sectional area A. Since we only focus on limestone and ceramic samples that have failure strains less than about 1.0 percent, we need only use engineering stress, strain, and strain-rate measures. In addition, we take stress positive in compression, strain positive in contraction, and particle velocity positive to the right in Fig. 3.4. Figure 3.4 also shows

the sample has cross-sectional area A_s and initial length l_o. We take subscripts 1 and 2 to represent the locations of the ends of the sample.
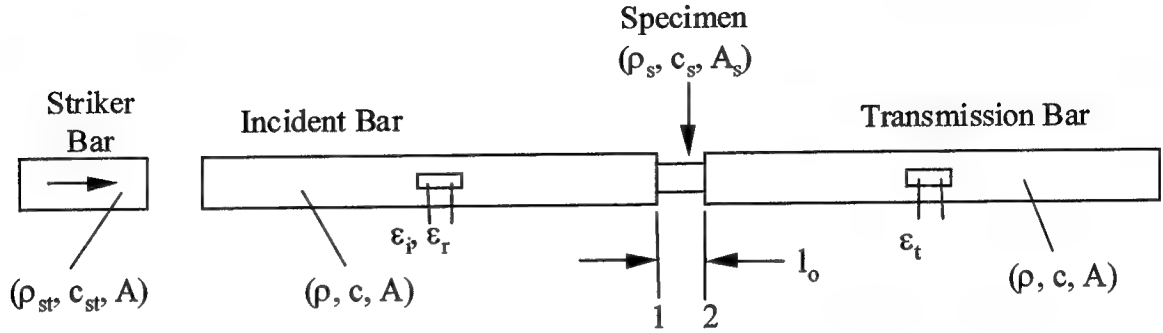
Figure 3.4 Schematic of a conventional split Hopkinson pressure bar (SHPB) or Kolsky bar

For homogeneous deformation, strain rate of the sample is given by

$$\frac{d\varepsilon_s}{dt} = \frac{v_1 - v_2}{l_o}, \tag{3.23}$$

where v_1 and v_2 are the particle velocities at the sample/bar interfaces. In terms of the measured strain pulses

$$\frac{d\varepsilon_s}{dt} = \frac{c}{l_o}(\varepsilon_i - \varepsilon_r - \varepsilon_t). \tag{3.24}$$

Forces at the ends of the sample are

$$P_1 = EA(\varepsilon_i + \varepsilon_r) \tag{3.25a}$$

$$P_2 = EA\varepsilon_t \tag{3.25b}$$

and the average force is

$$P_a = \frac{EA}{2}\left(\varepsilon_i + \varepsilon_r + \varepsilon_t\right). \tag{3.25c}$$

Similarly, stresses at the ends of the sample are

$$\sigma_1 = \frac{EA}{A_s}\left(\varepsilon_i + \varepsilon_r\right) \tag{3.26a}$$

$$\sigma_2 = \frac{EA}{A_s}\varepsilon_t \tag{3.26b}$$

and the average sample stress is

$$\sigma_a = \frac{EA}{2A_s}\left(\varepsilon_i + \varepsilon_r + \varepsilon_t\right). \tag{3.26c}$$

If $P_1 = P_2$, the forces on both ends of the sample are equal and $\varepsilon_i + \varepsilon_r = \varepsilon_t$. So if the sample is in dynamic stress equilibrium, the stress, strain rate, and strain are given by

$$\sigma_s = \frac{EA}{A_s}\varepsilon_t \tag{3.27}$$

$$\frac{d\varepsilon_s}{dt} = \frac{-2c}{l_o}\varepsilon_r \tag{3.28}$$

$$\varepsilon_s = \frac{-2c}{l_o}\int_0^t \varepsilon_r(\tau)\,d\tau. \tag{3.29}$$

As discussed in detail by Ravichandran and Subash (1994), Gray (1999), and Gray and Blumenthal (1999), eqs (3.27), (3.28), and (3.29) assume that the sample is in dynamic stress equilibrium. Equilibrium should first be examined by comparing the stresses σ_1 and σ_2 at the ends of the sample given by eqs (3.26a) and (3.26b). If σ_1 and σ_2 are in reasonable agreement, only then it is reasonable to use eqs (3.27), (3.28), and (3.29) to calculate sample stress, strain rate, and strain. The dynamic stress equilibrium condition for the sample will be discussed in detail in Chapter 4.

3.5   EXPERIMENTAL SET-UP

A split Hopkinson pressure bar was built at the U.S. Army Engineer Research and Development Center, Waterways Experiment Station (WES). The system, shown in Figure 3.5, was designed and built from the ground up for dynamic compression testing of metallic and geologic materials at strain rates ranging from 5 to 6,000 s^{-1}. Figure 3.6 is a schematic of the split Hopkinson pressure bar (SHPB).
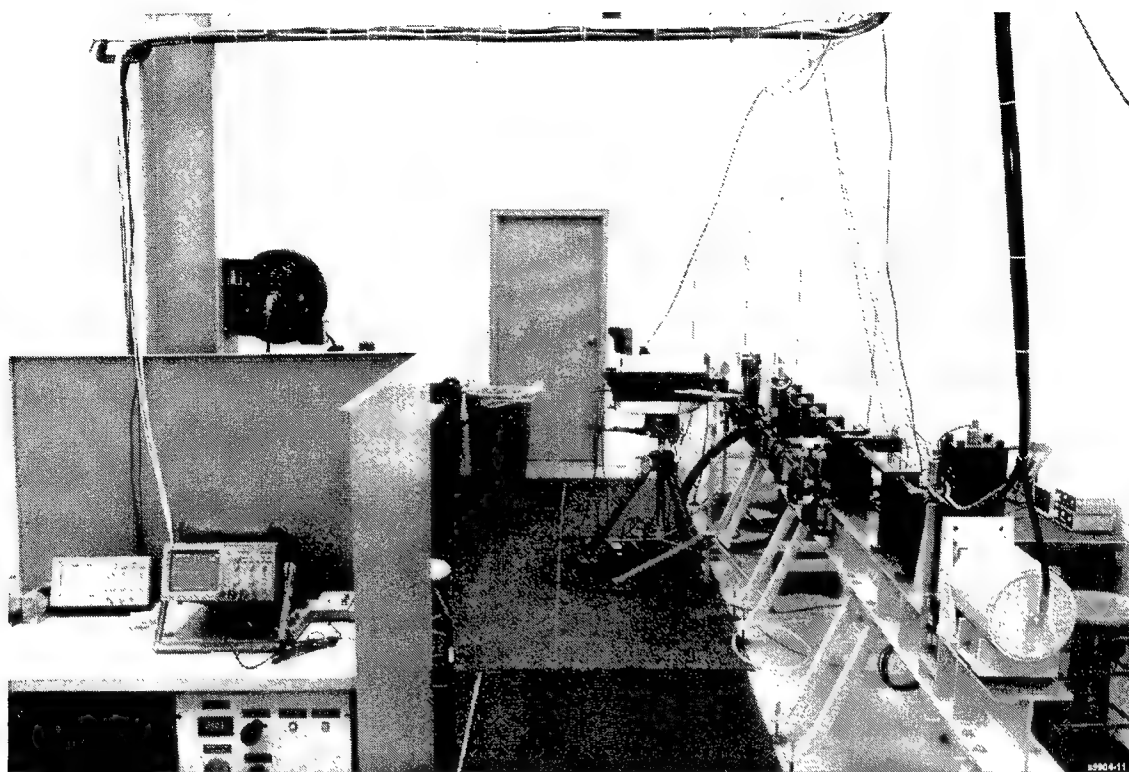
Figure 3.5 Photograph of WES split Hopkinson pressure bar facility
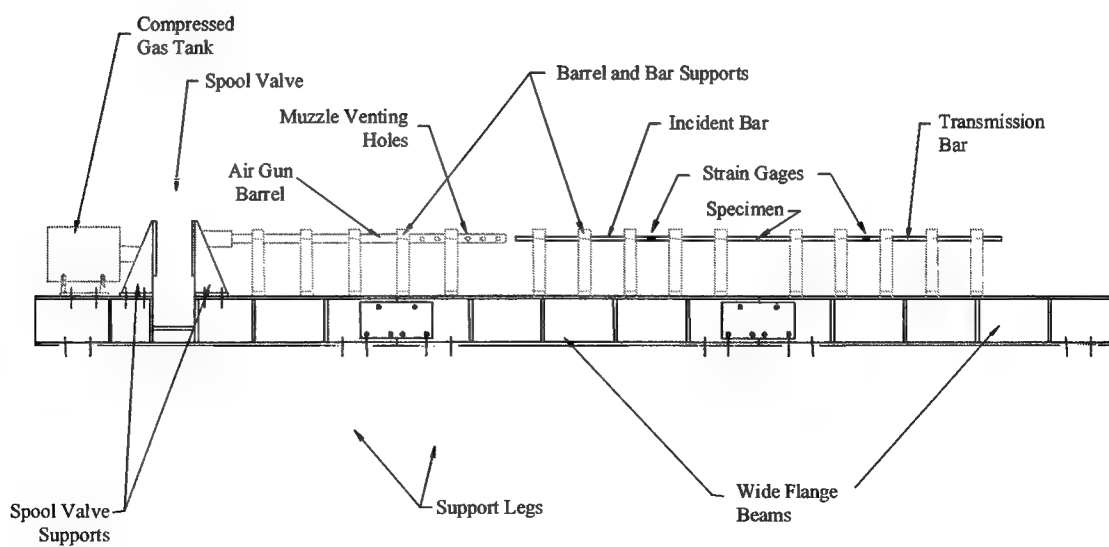
Figure 3.6 Split Hopkinson pressure bar schematic

The bars are supported by a frame consisting of 4, 203-mm-wide by 1.5-m-long, steel I-beams that rest on a total of 8 support legs. Extra stiffness was added to each beam by welding 8, 12.7-mm-thick, steel plates between the flanges. The tops of the beams were then machined flat to within 0.08 mm/m (0.001 in/ft). The support legs contact the ground through adjustable leveling pads. During assembly, the pads were used to adjust the height of each of the beams top surface until they were all level to the ground and parallel to one another to within 0.04 mm/m (0.0005 in/ft).

The barrel of the gas gun and the incident and transmission bars rest on aluminum supports with centers 241.3 mm above the top surface of the I-beams. Figure 3.7 shows a diagram of a support that contains a brass bushing for the barrel and bars to rest in. The bar bushings were designed to have a 0.08-mm diametrical clearance with the bar in order to carry the load of the bar but not inhibit the stress pulses travelling through. The bar supports were spaced along the length of the bars approximately every 200 mm. The striker and incident bars were aligned with one another by adjusting the positions of the barrel and incident bar supports until the faces of the bars were flush with one another and the incident bar slid freely through all the bushings. The supports were then fixed to the top surface of the I-beam with 100 mm "C" clamps. The transmission bar was aligned with the incident bar following the same procedure.
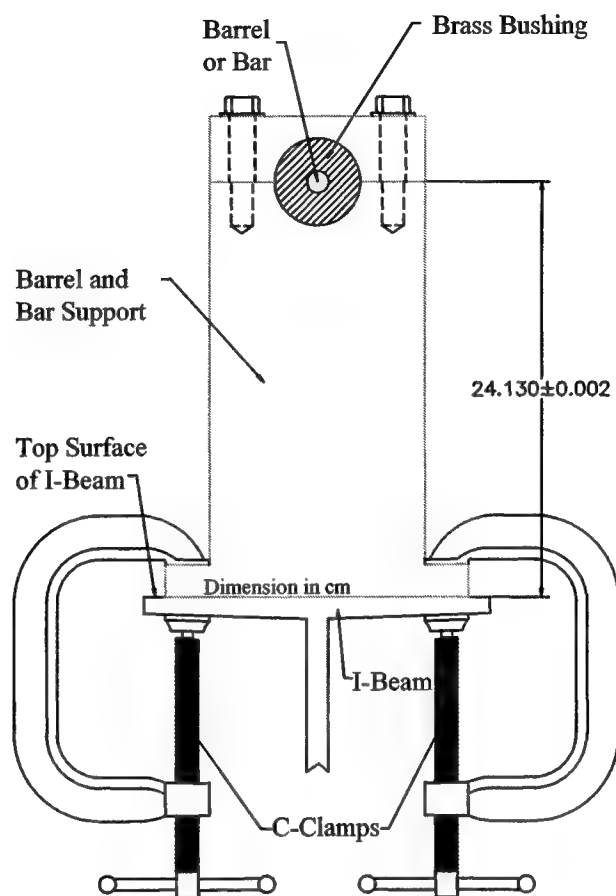
Figure 3.7 Barrel and bar support diagram

The gas gun assembly is composed of a gas tank, fast acting spool-valve, barrel, striker bar, and laser velocity system. The volume of the gas tank is 0.0125 m^3 with a maximum pressure rating of 7 MPa (1,000 psi). Operating pressure is provided to the gas tank via compressed air or nitrogen. The gas pressure is controlled through a 20 MPa (3,000 psi) Standard Pneumatic, Hemet, CA regulator (LC-2-98) and a differential pressure transducer (Model Z) and digital readout (Model GM) both from Sensotec, Inc., Columbus, OH. Resolution of the pressure transducer and digital readout is 2.58x10^{-3} MPa (0.38 psi) and 6.89x10^{-5} MPa (0.01 psi), respectively.

A normally closed 50-mm-diameter spool valve connects the gas tank to the barrel of the gun and is initiated through an electrical command. The Model 498 valve from SECO-DYN, Inc., Rancho Cucamonga, CA, is capable of completely opening within 1.5 ms regardless of the inlet (tank) pressure. Combining the performance of the valve with the resolution of the controls used for inlet pressure, the gas gun system can consistently produce striker bar velocities ranging from 3 to 75 m/s.

The gun barrel is a 38.1-mm-outside-diameter by 1.524-m-long tube of 1026 steel. The tube was straightened and then honed to a final inside diameter of 25.43 mm. A total of 20, 19-mm-diameter, venting holes were drilled near the muzzle of the barrel to vent the gas from behind the striker bar. The striker bar is loaded from the muzzle end of the barrel, and pushed in with a flexible hose until the striker rests on a collar placed between the spool valve and the tank end of the barrel. The barrel can accept striker bars up to 25.4-mm in diameter and lengths up to 500 mm.

A schematic of the laser velocity system used to measure the striking velocity of the striker bar is shown in Figure 3.8. The system consists of a pair of 0.8 mW helium-neon lasers (F61318) from Edmund Scientific, Barrington, NJ and photo detector units from the University of Dayton, Dayton, OH. Each laser and photo detector is positioned perpendicular to the flight path of the striker bar between the muzzle of the barrel and the free end of the incident bar. As the striker bar exits the muzzle of the barrel, its leading edge will begin to disrupt the laser signal for detector #1. Further down range and at some later time, detector #2 will trigger in the same manner. The output signals are recorded on a two channel, 100MHz Tektronix TDS220 digital oscilloscope. The photo detector units have a light-to-dark response time of about 1.5 μs, and by accurately

measuring the distance, X, between the two laser beams and the time difference between the two triggers, the striking velocity of the striker bar can be accurately measured to within 0.01 m/s.
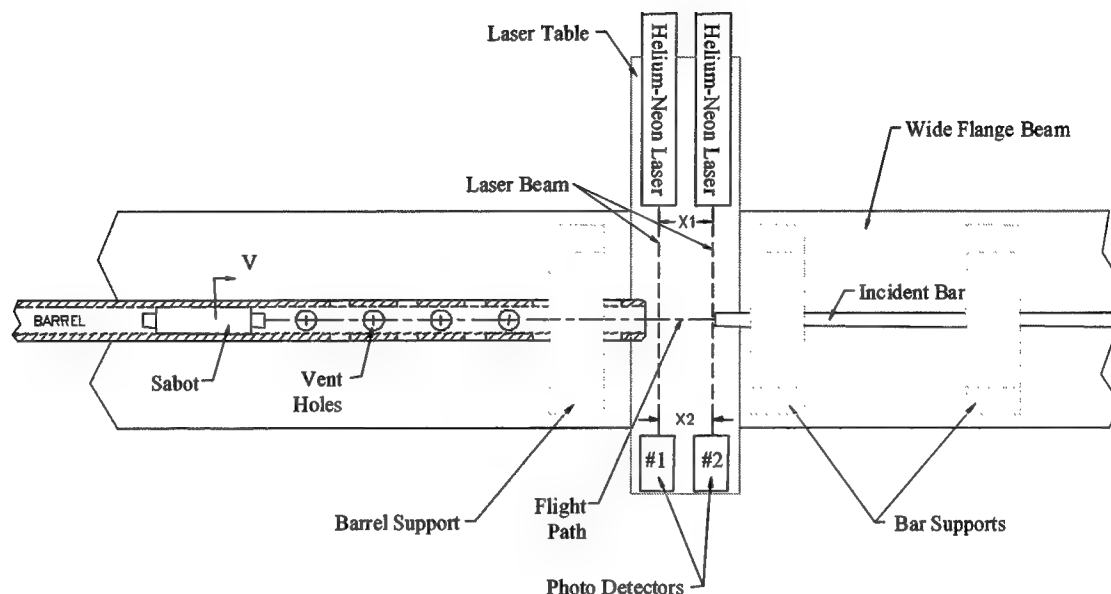
Figure 3.8 Schematic of laser velocity measurement system

The bars were made of VascoMax C-350 maraging steel (HRC = 58) having a uniaxial compressive yield strength, Young's modulus, and density of 2.7 GPa, 200 GPa and 8100 kg/m^3 (Vasco-Pacific, 1998), respectively. The diameters of all the bars were centerless ground and straight to within 0.42-mm/m. After grinding, the bars were faced to length and end-faces polished to a mirror finish. Striker bar lengths for these studies varied from 38.1 mm to 398.4 mm based on the desired shape and duration of the incident pulse. The striker bar is fitted with a shrunk fit nylon sabot that is machined to have an outside diameter of 25.36 ± .03 mm. The tight tolerance of the sabot diameter helps align the striker bar for impact with the incident bar.

Diametrically opposed strain gages positioned on the incident and transmission bars form part of two Wheatstone half-bridges. The output signals from the bridges are recorded using a 4 channel Tektronix 420A digitizing oscilloscope with ADA400A differential preamplifiers. The gages used in this study were manufactured by Measurements Group, Inc., Raleigh, NC (WK-06-250BF-10C) and had a nominal resistance of 1000 Ω. The 30 Volt DC excitation for the Wheatstone bridge was provided by an Hewlett Packard (Englewood, CO) E3611A power supply.

3.6   CONVENTIONAL SPLIT HOPKINSON PRESSURE BAR RESULTS

We present results from a conventional SHPB experiment with an Indiana limestone sample. Pettijohn (1975), and Podnieks, Chamberlain, and Thill (1972) describe this limestone as a carbonate rock that contains over 90 percent calcite and less than 10 percent quartz, having a porosity of about 15 percent, and a grain size ranging between 0.15 and 1.0 mm. For this study, the limestone samples had density $\rho_s = 2300$ kg/m^3, Young's modulus $E_s = 24$ GPa, and bar wave velocity $c_s = 3200$ m/s. Young's modulus was estimated from quasi-static compression data shown in Chapter 6.

Limestone cores, 13-mm in diameter, were drilled from a block perpendicular to the bedding plane, with a thin walled diamond core barrel. The core was cut to a rough length and the ends ground flat and parallel to within ±0.025 mm. The outside diameter and length of the sample was then machined to 12.7 mm with the sides perpendicular to the ends of the sample to within 0.1°. A photograph of a prepared limestone sample is

shown in Figure 3.9. To maximize the magnitude of the strain pulse transmitted from this weak specimen, the bar diameter was chosen as the sample diameter.
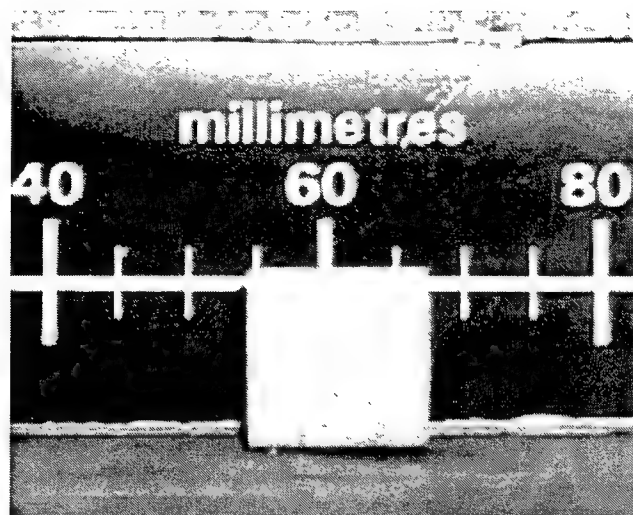
Figure 3.9 Pretest photograph of Indiana limestone sample

The strain gages shown in Fig. 3.4 are located at 1060 mm from the impact surface on the incident bar and 229 mm from the sample/ bar interface on the transmission bar. Figure 3.10 shows incident, reflected, and transmitted strain-time signals for a limestone test with a striking velocity of 8.05 m/s. The incident pulse has a fast rise time of about 10 μs and a pulse width of about 60 μs that corresponds to the two wave transit times in the striker bar. Figure 3.11 shows stress versus time at the ends of the sample calculated from eqs (3.26a) and (3.26b) and the average strain rate calculated from eq (3.24). For an ideal SHPB experiment, the sample should be in equilibrium and should deform at a constant strain rate over most of the duration of the test. However, Fig. 3.11 shows that σ_1 and σ_2 are not in close agreement and that the strain rate is not constant over the duration of the test. It is therefore apparent that improved testing

techniques need to be developed in order to conduct valid SHPB experiments on brittle materials.

In the next chapters, we present models and experimental results that show a ramp incident pulse is required to obtain sample equilibrium and constant strain rate over most of the test duration for Indiana limestone samples. The ramp incident pulse is produced by placing a thin copper disk on the impact surface of the incident bar. We will also describe the details of pulse shaping techniques in Chapter 5.
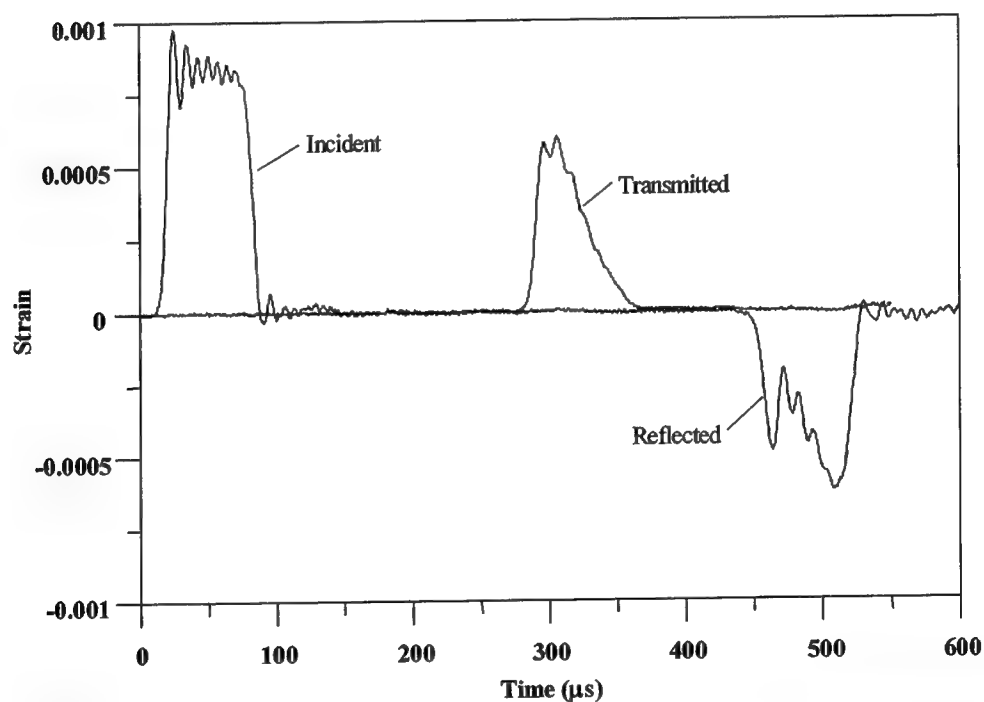
Figure 3.10 Strain-time signals for a conventional SHPB experiment with a limestone sample
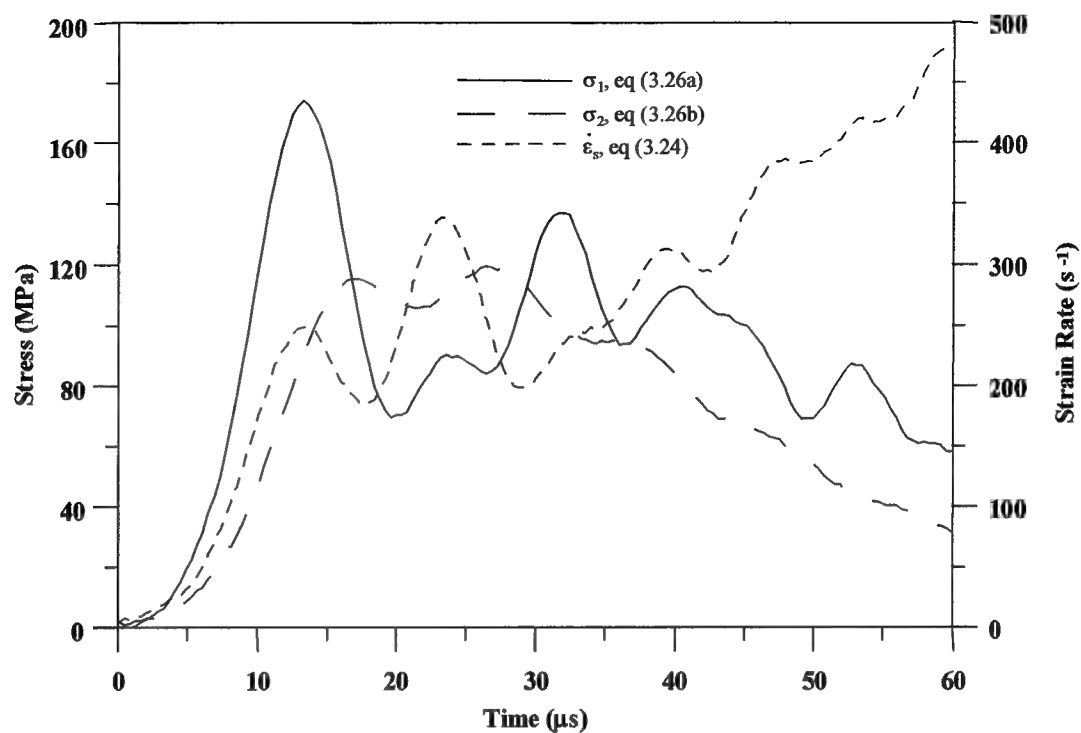
Figure 3.11 Interface stresses and strain rate from a conventional SHPB experiment with a limestone sample

CHAPTER 4

SAMPLE EQUILIBRIUM AND CONSTANT STRAIN RATE MODELS

In this chapter, we develop models that show the evolutionary process for sample equilibrium and constant strain rate for brittle materials that have a linear stress-strain response until failure. These models and subsequent experiments show that a ramp stress pulse in the incident bar is required in order to obtain sample equilibrium and constant strain rate over most of the duration of the experiment. The first model assumes that the sample is in dynamic stress equilibrium and predicts strain and strain rate versus time. For the second model, we perform a wave propagation analysis on the interaction of the sample with the incident and transmission bars. This second model predicts the stress-time histories on either side of the sample.

4.1 DYNAMIC STRESS EQUILIBRIUM MODEL

Consider a second order polynomial, stress pulse propagating in the incident bar given by

$$\sigma_i(x, t) = \left[\sigma_o + M \cdot (t - x/c) + N \cdot (t - x/c)^2\right] H(t - x/c) \qquad (4.1)$$

where σ_o, M, and N are polynomial constants and H is the Heaviside unit function. We take x = 0 at the interface between the incident bar and the sample labeled as station 1 in Fig. 3.4. If the sample is in equilibrium, $\sigma_1 = \sigma_2$, we can neglect wave propagation in the sample. The sample is assumed to have a linear stress-strain response to failure given by

$$\sigma_s = E_s \, \varepsilon_s \tag{4.2}$$

where E_s is the Young's modulus for the sample.

When the incident stress pulse reaches the sample, a tensile pulse is reflected back into the incident bar and a compressive pulse is transmitted into the transmission bar. As before, we take stress positive in compression, strain positive in contraction, and particle velocity positive to the right in Fig. 3.4. From the equations of elementary bar theory (Graff, 1975), strain rate in the sample, given by eq (3.23), can be written in terms of the incident σ_i, reflected σ_r, and transmitted σ_t stress pulses in the bars as

$$\frac{d\varepsilon_s}{dt} = \frac{1}{\rho \, c \, l_o} (\sigma_i - \sigma_r - \sigma_t). \tag{4.3}$$

For a sample in equilibrium, $\sigma_i + \sigma_r = \sigma_t$, and

$$\frac{d\varepsilon_s}{dt} = \frac{2}{\rho \, c \, l_o} (\sigma_i - \sigma_t). \tag{4.4}$$

The incident and transmitted stresses in the bars are

$$\sigma_i(t) = \sigma_o + Mt + Nt^2 \tag{4.5a}$$

$$\sigma_t = \frac{A_s E_s \varepsilon_s}{A}. \tag{4.5b}$$

From eqs (4.4) and (4.5),

$$\frac{d\varepsilon_s}{dt} + \frac{2A_s E_s}{\rho c A l_o}\varepsilon_s = \frac{2\sigma_i(t)}{\rho c l_o} \tag{4.6}$$

which has solutions

$$\frac{d\varepsilon_s}{dt} = \frac{2\sigma_o \gamma}{E_s r t_o}\exp\left(\frac{-2t}{r t_o}\right) + \frac{\gamma M}{E_s}\left[1 - \exp\left(\frac{-2t}{r t_o}\right)\right] +$$
$$\frac{N\gamma t_o r}{E_s}\left[-1 + \frac{2t}{r t_o} + \exp\left(\frac{-2t}{r t_o}\right)\right] \tag{4.7a}$$

$$\varepsilon_s = \frac{\sigma_o \gamma}{E_s}\left[1 - \exp\left(\frac{-2t}{r t_o}\right)\right] + \frac{\gamma M}{E_s}\left[t - \frac{r t_o}{2}\left(1 - \exp\left(\frac{-2t}{r t_o}\right)\right)\right] +$$
$$\frac{N\gamma(r t_o)^2}{2 E_s}\left[1 + \left(\frac{-2t}{r t_o}\right) + 2\left(\frac{t}{r t_o}\right)^2 - \exp\left(\frac{-2t}{r t_o}\right)\right] \tag{4.7b}$$

$$\gamma = \frac{A}{A_s}, \qquad r = \frac{A \rho c}{A_s \rho_s c_s}, \qquad t_o = \frac{l_o}{c_s}. \tag{4.7c}$$

Equations (4.7a) and (4.7b) give closed-form solutions for the strain rate and strain in a sample that is in dynamic stress equilibrium. Qualitatively, we can use eq (4.7a) to predict the required incident pulse necessary to test a quasi-linear, brittle sample at a constant strain rate.

First consider the incident pulse from a conventional SHPB experiment (described in section 3.6) that consists of a very sharp rise to a flat plateau (see Fig. 3.10). The shape of such a pulse can be approximated as a step input, so eq (4.5a) reduces to

$$\sigma_i(t) = \sigma_o \tag{4.8}$$

and eq (4.7a) simplifies to

$$\frac{d\varepsilon_s}{dt} = \frac{2\sigma_o \gamma}{E_s r t_o} \exp\left(\frac{-2t}{r t_o}\right). \tag{4.9}$$

Figure 4.1 shows a prediction of the normalized strain rate from eq (4.9). The strain rate is exponentially decaying and not constant. The strain rate will not reach a constant level during the experiment and thus results from such a test can not be used to describe the dynamic response of the test material at constant strain rate. Other incident pulse shapes must therefore be investigated to find an input that will produce valid SHPB results for these types of materials.

Now consider the case where we apply a linear ramp input into the sample. Equation (4.5a) is given by

$$\sigma_i(t) = Mt \qquad\qquad (4.10)$$

and eq (4.7a) takes the form

$$\frac{d\varepsilon_s}{dt} = \frac{\gamma M}{E_s}\left[1 - \exp\left(\frac{-2t}{r\,t_o}\right)\right]. \qquad\qquad (4.11)$$

Figure 4.2 shows the model prediction of normalized strain rate from eq (4.11). Unlike the case of a step input, the ramp input predicts that the strain rate in the sample will approach a constant value after some normalized time. We will show later, in Chapter 6, that experimental results on Indiana limestone correlate well with model predictions for a linear ramp input.
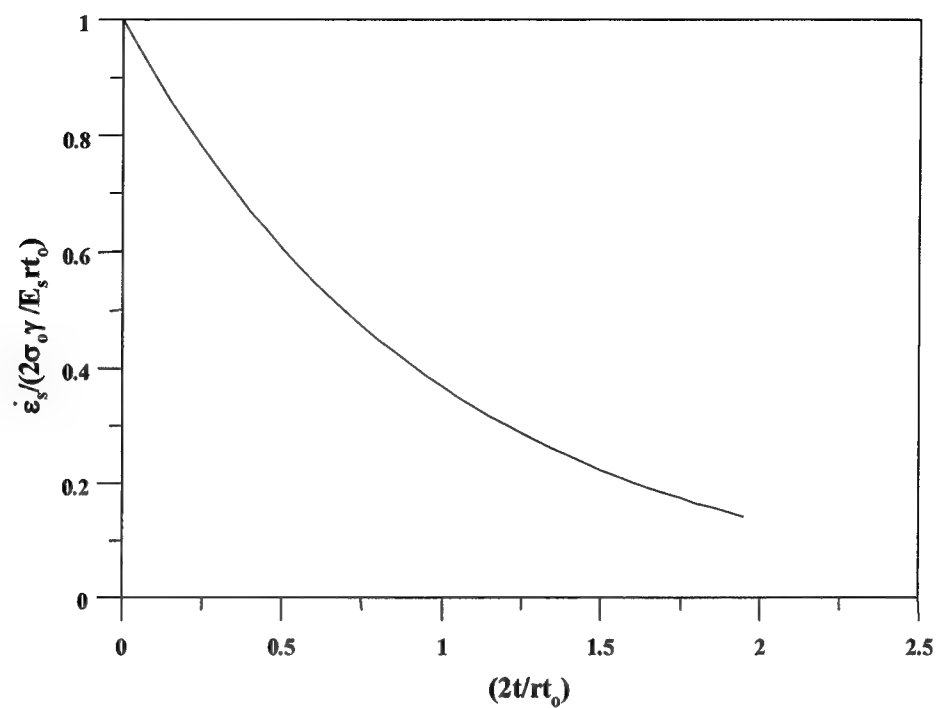
Figure 4.1 Sample equilibrium model for strain rate using a step input
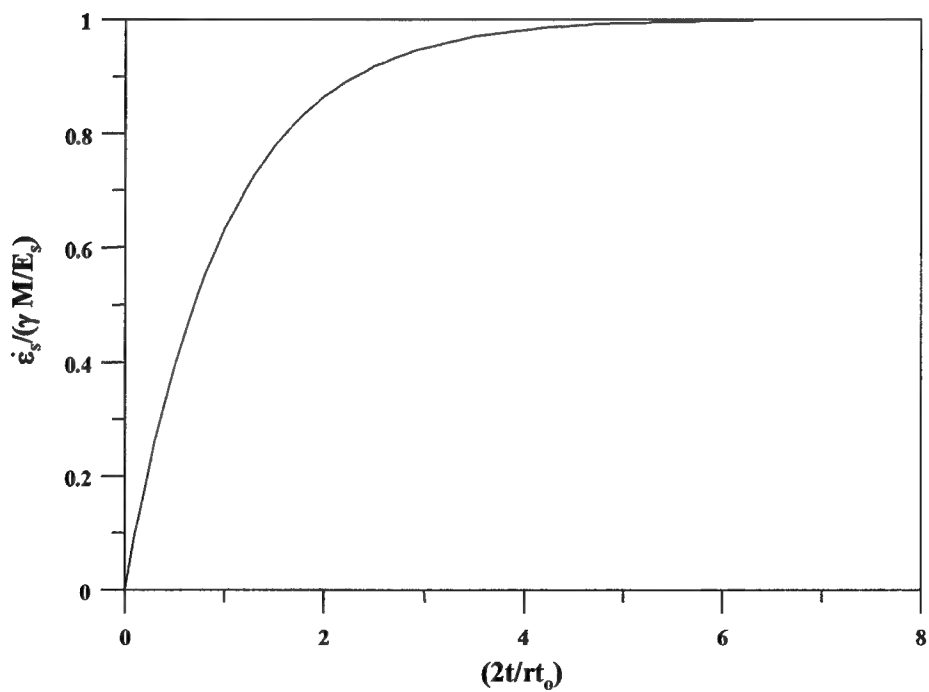
Figure 4.2 Sample equilibrium model for strain rate using a linear ramp input

4.2 WAVE ANALYSIS MODEL

For the second model, we perform a wave propagation analysis on the interaction of the sample with the incident and transmission bars. Ravichandran and Subhash (1994) present a method of characteristics solution for this problem and show results for ceramic materials. Our analysis of this same problem provides general, closed-form equations that we find more convenient for numerical applications.

We use the elementary theory of wave propagation in bars to calculate the stress-time histories at the ends of the sample. Ravichandran and Subhash (1994) and Graff (1975) present equations for the reflected and transmitted stresses at the interfaces shown in Fig. 3.4. At the incident bar/ sample interface (location 1 in Fig. 3.4), the stresses transmitted to the specimen σ_t and reflected in the incident bar σ_r are

$$\sigma_t = \left(\frac{2\gamma}{r+1}\right)\sigma_i \qquad (4.12a)$$

$$\sigma_r = -\left(\frac{r-1}{r+1}\right)\sigma_i \qquad (4.12b)$$

in which r is given by eq (4.7c) and σ_i is the incident pulse given by eq (4.1). As before, we take $x = 0$ at station 1 in Fig. 3.4, and the stress in the sample at station 1 is

$$\sigma_1 = \frac{2\gamma}{r+1}\sigma_i(t), \qquad\qquad 0 \le t < 2t_o. \quad (4.13)$$

At $t = t_o$, the stress wave in the sample reaches the sample/ transmission bar interface (location 2 in Fig. 3.4). When the stress wave in the sample interacts with the transmission bar, the stresses transmitted into the transmission bar σ_t and reflected into the sample are

$$\sigma_t = \frac{2r}{\gamma(r+1)}\sigma_1(t-\tau), \qquad t_o \le t < 3t_o \quad (4.14a)$$

$$\sigma_r = \left(\frac{r-1}{r+1}\right)\sigma_1(t-\tau), \qquad t_o \le t < 3t_o \quad (4.14b)$$

where σ_1 is given by eq (4.13). The stress in the sample at station 2 consists of the incident and reflected stress waves and is given by

$$\sigma_2(t) = \frac{2\gamma}{r+1}\sigma_i(t-t_o) + \left(\frac{r-1}{r+1}\right)\frac{2\gamma}{r+1}\sigma_i(t-t_o), \, t_o \le t < 3t_o. \quad (4.15)$$

We repeat this interaction process several times and obtain the stresses in the sample at interface 1 shown in Fig. 3.4 are

$$\sigma_1 = \frac{2\gamma}{r+1}\sigma_i(t), \qquad 0 \le t < 2t_o \quad (4.16a)$$

$$\sigma_1 = \frac{2\gamma}{r+1}\sigma_i(t) + \frac{2\gamma}{r+1}\left[\left(\frac{r-1}{r+1}\right) + \left(\frac{r-1}{r+1}\right)^2\right]\sigma_i(t-2t_o), \, 2t_o \le t < 4t_o \quad (4.16b)$$

$$\sigma_1 = \frac{2\gamma}{r+1}\sigma_i(t) + \frac{2\gamma}{r+1}\left[\left(\frac{r-1}{r+1}\right) + \left(\frac{r-1}{r+1}\right)^2\right]\sigma_i(t-2t_o) +$$

$$\frac{2\gamma}{r+1}\left[\left(\frac{r-1}{r+1}\right)^3 + \left(\frac{r-1}{r+1}\right)^4\right]\sigma_i(t-4t_o), \quad 4t_o \le t < 6t_o \quad (4.16c)$$

and that at interface 2 are

$$\sigma_2 = 0, \qquad\qquad 0 \le t < t_o \quad (4.17a)$$

$$\sigma_2 = \frac{2\gamma}{r+1}\left[1 + \left(\frac{r-1}{r+1}\right)\right]\sigma_i(t-t_o), \qquad t_o \le t < 3t_o \quad (4.17b)$$

$$\sigma_2 = \frac{2\gamma}{r+1}\left[1 + \left(\frac{r-1}{r+1}\right)\right]\sigma_i(t-t_o) + \frac{2\gamma}{r+1}\left[\left(\frac{r-1}{r+1}\right)^2 + \left(\frac{r-1}{r+1}\right)^3\right]\sigma_i(t-3t_o),$$

$$3t_o \le t < 5t_o. \quad (4.17c)$$

The nth term for eqs (4.16) and (4.17) is

$$\frac{2\gamma}{r+1}\left[\left(\frac{r-1}{r+1}\right)^{n-1} + \left(\frac{r-1}{r+1}\right)^n\right]\sigma_i(t-nt_o), \quad \text{for } nt_o \le t < (n+2)t_o,$$

where t_o is given by eq (4.7c) and corresponds to one wave travel time through the sample. Therefore, σ_1 and σ_2 can easily be calculated for times greater than those given by eqs (4.16) and (4.17).

For the polynomial incident stress pulse given by eq (4.1), we obtain

$$\sigma_1 = \frac{2\gamma}{r+1}\{\sigma_o + Mt + Nt^2\}, \qquad 0 \le t < 2t_o \quad (4.18a)$$

$$\sigma_1 = \frac{2\gamma\sigma_o}{r+1}\left\{1 + \left(\frac{r-1}{r+1}\right) + \left(\frac{r-1}{r+1}\right)^2\right\} + \frac{2\gamma M}{r+1}\left\{t + \left[\left(\frac{r-1}{r+1}\right) + \left(\frac{r-1}{r+1}\right)^2\right](t-2t_o)\right\} +$$

$$\frac{2\gamma N}{r+1}\left\{t^2 + \left[\left(\frac{r-1}{r+1}\right) + \left(\frac{r-1}{r+1}\right)^2\right](t-2t_o)^2\right\}, \quad 2t_o \le t < 4t_o \quad (4.18b)$$

$$\sigma_1 = \frac{2\gamma\sigma_o}{r+1}\left\{1 + \left(\frac{r-1}{r+1}\right) + \left(\frac{r-1}{r+1}\right)^2 + \left(\frac{r-1}{r+1}\right)^3 + \left(\frac{r-1}{r+1}\right)^4\right\} +$$

$$\frac{2\gamma M}{r+1}\left\{t + \left[\left(\frac{r-1}{r+1}\right) + \left(\frac{r-1}{r+1}\right)^2\right](t-2t_o) + \left[\left(\frac{r-1}{r+1}\right)^3 + \left(\frac{r-1}{r+1}\right)^4\right](t-4t_o)\right\} +$$

$$\frac{2\gamma N}{r+1}\left\{t^2 + \left[\left(\frac{r-1}{r+1}\right) + \left(\frac{r-1}{r+1}\right)^2\right](t-2t_o)^2 + \left[\left(\frac{r-1}{r+1}\right)^3 + \left(\frac{r-1}{r+1}\right)^4\right](t-4t_o)^2\right\},$$

$$4t_o \le t < 6t_o \quad (4.18c)$$

and

$$\sigma_2 = 0, \qquad 0 \le t < t_o \quad (4.19a)$$

$$\sigma_2 = \frac{2\gamma\sigma_o}{r+1}\left\{1 + \left(\frac{r-1}{r+1}\right)\right\} + \frac{2\gamma M}{r+1}\left\{\left[1 + \left(\frac{r-1}{r+1}\right)\right](t-t_o)\right\} +$$

$$\frac{2\gamma N}{r+1}\left\{\left[1 + \left(\frac{r-1}{r+1}\right)\right](t-t_o)^2\right\}, \qquad t_o \le t < 3t_o \quad (4.19b)$$

$$\sigma_2 = \frac{2\gamma\sigma_o}{r+1}\left\{1 + \left(\frac{r-1}{r+1}\right) + \left(\frac{r-1}{r+1}\right)^2 + \left(\frac{r-1}{r+1}\right)^3\right\} +$$

$$\frac{2\gamma\,M}{r+1}\left\{\left[1 + \left(\frac{r-1}{r+1}\right)\right](t-t_o) + \left[\left(\frac{r-1}{r+1}\right)^2 + \left(\frac{r-1}{r+1}\right)^3\right](t-3t_o)\right\} +$$

$$\frac{2\gamma\,N}{r+1}\left\{\left[1 + \left(\frac{r-1}{r+1}\right)\right](t-t_o)^2 + \left[\left(\frac{r-1}{r+1}\right)^2 + \left(\frac{r-1}{r+1}\right)^3\right](t-3t_o)^2\right\},$$

$$3t_o \le t < 5t_o \quad (4.19c)$$

The nth term for eqs (4.18) and (4.19) is

$$\frac{2\gamma\sigma_o}{r+1}\left(\frac{r-1}{r+1}\right)^n + \frac{2\gamma\,M}{r+1}\left[\left(\frac{r-1}{r+1}\right)^{n-1} + \left(\frac{r-1}{r+1}\right)^n\right](t-nt_o) + \frac{2\gamma\,N}{r+1}\left[\left(\frac{r-1}{r+1}\right)^{n-1} + \left(\frac{r-1}{r+1}\right)^n\right](t-nt_o)^2$$

for the time interval $nt_o \le t < (n+2)t_o$.

Figures 4.3 and 4.4 show model predictions for sample stresses and strain rate versus time for a linear ramp incident pulse. These predictions correspond to experiments with steel bars and limestone samples ($r = 5.5$) and with equal sample and bar diameters ($\gamma = 1$). In addition, we know from test data that the sample fails or starts to fail at a sample stress $\sigma_s > 120$ MPa. For Fig. 4.3, the incident ramp pulse, given by eq (4.10), has a loading rate $M = 3.3$ MPa/μs and corresponds to the loading on a limestone sample discussed in Chapter 6. Figure 4.3 shows that the stresses at the incident bar/ sample interface σ_1 and the sample/ transmission bar interface σ_2 are nearly equal for $t/t_o > 2$. In addition, the sample stress predicted by the model that assumes sample equilibrium given by eqs (4.2) and (4.7b) lies between σ_1 and σ_2. The strain rate rapidly

increases from $0 < t/t_o < 4$ and is nearly constant for $4 < t/t_o < 12$, so the strain rate is nearly constant for a sample stress between about 20 and 120 MPa. Figure 4.4 shows model predictions for stresses and strain rate versus time for a stress loading rate of M = 9.9 MPa/μs. A comparison of the results in Figs. 4.3 and 4.4 show that as the loading rate increases from 3.3 to 9.9 MPa/μs, the interface stresses σ_1 and σ_2 begin to differ from each other and the strain rate varies significantly over most of the duration of the test. Figure 4.4 also suggests that it is easier to obtain sample equilibrium than a nearly constant strain rate over most of the test duration. In Chapter 6, we will compare these model predictions with experimental data.
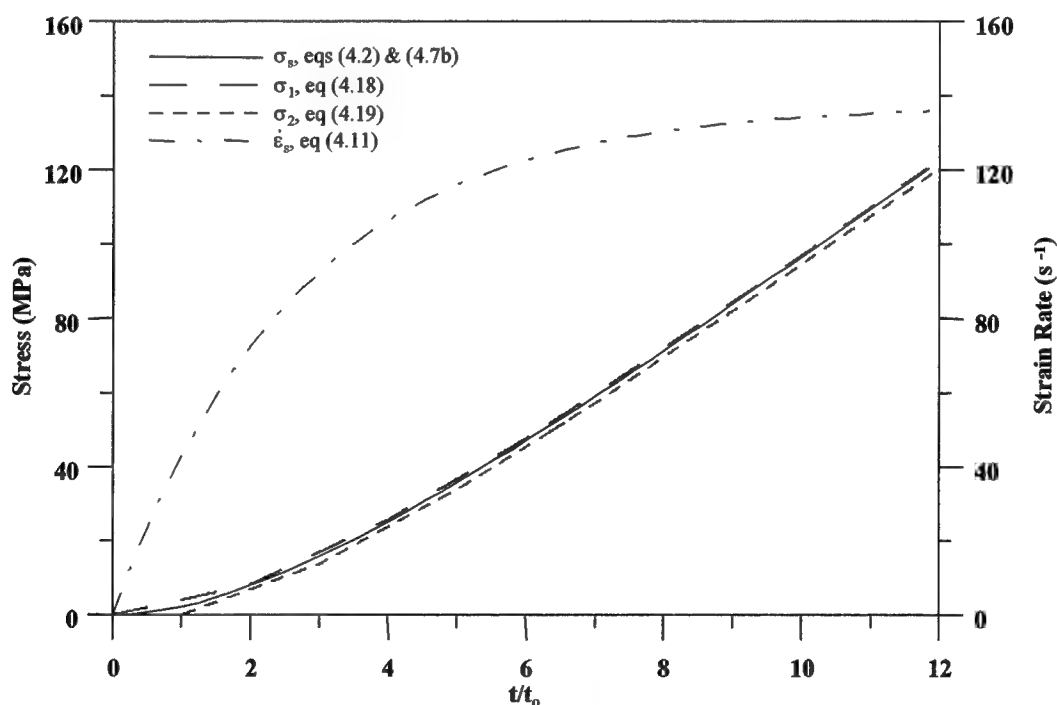
Figure 4.3 Stress and strain rate model predictions for a limestone sample loaded by a ramp incident pulse with a stress loading rate of M= 3.3 MPa/μs
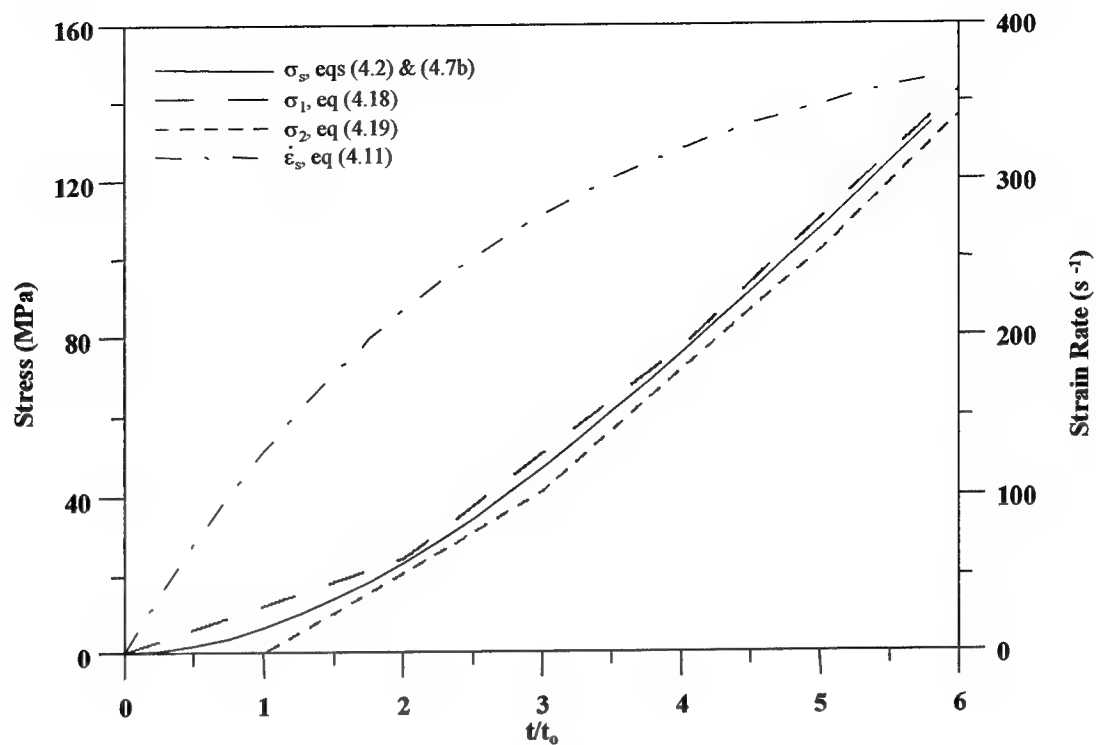
Figure 4.4 Stress and strain rate model predictions for a limestone sample loaded by a ramp incident pulse with a stress loading rate of $M = 9.9$ MPa/μs

CHAPTER 5

PULSE SHAPING

5.1 BACKGROUND

For an ideal Kolsky compression bar experiment, the sample should be in dynamic stress equilibrium and deform at a nearly constant strain rate over most of the test duration. To approximate these ideal conditions for brittle materials, Nemat-Nasser, Isaacs, and Starrett (1991) modified the conventional Kolsky compression bar by placing an oxygen-free-copper (OFHC) disk on the impact surface of the incident bar. When the striker bar impacts the copper disk, the large plastic deformation of the disk spreads the pulse in the incident bar and allows time for the brittle sample to achieve dynamic stress equilibrium. Thus, shaping the pulse in the incident bar is an essential modification for testing brittle materials with the compression Kolsky bar technique. Experiments that attempt to obtain high-rate, stress-strain data for ceramic materials at constant strain rates are reported by Rogers and Nemat-Nasser (1990), and Chen and Ravichandran (1997). In addition, Nemat-Nasser, Isaacs, and Starrett (1991) present a model that predicts the strain pulse in the incident bar for an OFHC (Lewis, 1979) copper pulse shaper, and Ravichandran and Subhash (1994) present a sample equilibrium model for ceramic materials.

While pulse shaping techniques have been successfully used to achieve the goals of many different experiments, pulse shapers are usually designed by experimental trials

that exclude a model to guide the design parameters. For example, Duffy, Campbell, and Hawley (1971) used a pulse shaper to smooth pulses generated by explosive loading for torsional Hopkinson bar experiments, and Wu and Gorham (1997) used paper on the impact surface of the incident bar to eliminate high frequency oscillations in the incident pulse for Kolsky compression bar experiments. Togami, Baker, and Forrestal (1996) used a thin, plexiglass disk to produce nondispersive compression pulses in an incident bar, and Chen, Zhang, and Forrestal (1999) used a polymer disk to spread the incident compressive pulses for experiments with elastomers. Christensen, Swanson, and Brown (1972) used striker bars with a truncated cone on the impact end in an attempt to produce ramp pulses. In contrast to other pulse shaping studies, Nemat-Nasser, Isaacs, and Starrett (1991) model the plastic deformation of an OFHC copper pulse shaper, predict the incident strain pulse, and show good agreement with some measured incident strain pulses.

In this chapter, we extend the analytical model of Nemat-Nasser, Isaacs, and Starrett (1991) and present new data for annealed and hard C11000 (Lewis, 1979) copper pulse shapers. Experiments conducted with both OFHC and C11000 copper pulse shapers showed a superior performance by the C11000 materials. In particular, the C11000 pulse shapers could be driven to larger strains without breakup or fracture and remained more circular after deformation. We found that with both annealed and hard C11000 pulse shapers, we could obtain a broad range of strain rates for testing brittle ceramic and rock (Frew, Forrestal, and Chen, 2000) materials. The previous model (Nemat-Nasser, Isaacs, and Starrett, 1991) was extended to accommodate the large strains obtained in the C11000 copper materials. In addition, we modified the equations

that govern wave propagation in the striker bar to incorporate the added mass from the sabot and include elastic, rather than rigid, unloading in the pulse shaping analysis. Incident stress pulse model predictions are shown to be in good agreement with measurements from several tests.

5.2 PULSE SHAPING MODEL

Figure 5.1 shows a schematic of the impact end of the SHPB apparatus with a pulse shaper that is attached with a light coating of grease. In Fig. 5.1, ρ_{st}, c_{st}, and A are the density, bar wave velocity, and cross-sectional area of the striker bar, respectively; V_o is the striker velocity at impact; a_o and h_o are the initial cross-sectional area and thickness of the pulse shaper; and ρ, c, A, and E are the properties for the incident bar, respectively. When the striker bar impacts the pulse shaper, compressive forces are gradually transferred from the pulse shaper to the incident bar. The deformation of the pulse shaper increases its load carrying capacity by increasing its cross-sectional area and by the strain hardening of the pulse shaping material. As will be shown later, the monotonic increase of the load carrying capacity of the pulse shaper causes longer duration loading pulses in the incident bar.
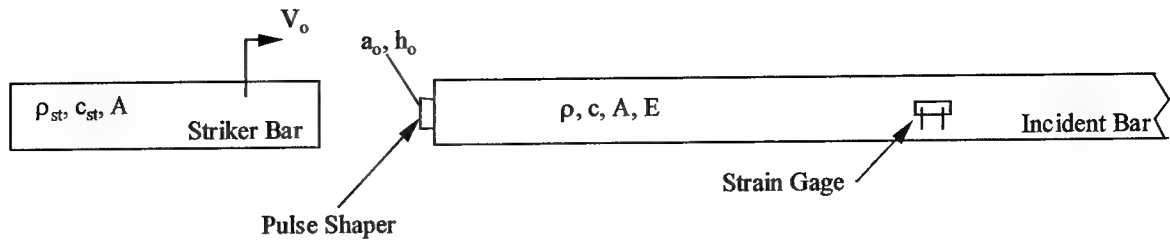
Figure 5.1 Schematic of the loading end of a SHPB with a pulse shaper

For an incompressible material and a homogeneous deformation, mass conservation gives

$$a_o h_o = a(t)h(t), \tag{5.1}$$

where $a(t)$ and $h(t)$ are the current cross-sectional area and thickness of the pulse shaper. The axial engineering strain in the pulse shaper is given by

$$\varepsilon_p(t) = \frac{h_o - h(t)}{h_o} = 1 - \frac{h(t)}{h_o} \tag{5.2}$$

which is positive in contraction. From eqs (5.1) and (5.2), the current cross-sectional area of the pulse shaper can be written in terms of the original area and axial strain in the pulse shaper. Thus,

$$a(t) = \frac{a_o}{1 - \varepsilon_p(t)}. \tag{5.3}$$

The axial force exerted by the pulse shaper on the ends of the striker and incident bars is

$$T(t) = \sigma_p(t)a(t) = \sigma_i(t)A = \sigma_{st}(t)A, \qquad (5.4)$$

where $\sigma_p(t)$ is the true axial stress in the pulse shaper, $\sigma_i(t)$ is from the compressive stress wave travelling to the right in the incident bar, and $\sigma_{st}(t)$ is from the compressive stress wave travelling to the left in the striker bar. From eq (5.4), the bar stresses at the pulse shaper/ bar interfaces are

$$\sigma_i(t) = \sigma_{st}(t) = \frac{\sigma_p(t)a(t)}{A}. \qquad (5.5)$$

For now, let $\sigma_p(t)$ be defined by the general form of a one-dimensional stress-strain relationship

$$\sigma_p = \sigma_o\, g(\varepsilon_p), \qquad (5.6)$$

where σ_o is a constant and $g(\varepsilon_p)$ is a function of the pulse shaper engineering axial strain. From eqs (5.2), (5.5), and (5.6)

$$\sigma_i(t) = \sigma_{st}(t) = \frac{\sigma_o\, a_o}{A}\frac{g(\varepsilon_p)}{(1-\varepsilon_p)}. \qquad (5.7a)$$

Since the incident and striker bars remain elastic, the axial strains in the bars at the bars/ pulse shaper interfaces can be written as

$$\varepsilon_i(t) = \varepsilon_{st}(t) = \frac{\sigma_o a_o}{EA} \frac{g(\varepsilon_p)}{(1-\varepsilon_p)}. \tag{5.7b}$$

The engineering strain rate in the pulse shaper is given by

$$\dot{\varepsilon}_p(t) = \frac{v_3(t) - v_4(t)}{h_o}, \tag{5.8}$$

where $v_3(t)$ and $v_4(t)$ are the particle velocities at the striker bar/pulse shaper (3) and incident bar/pulse shaper (4) interfaces, respectively shown in Fig. 5.2. From the equations that relate stress and particle velocity in the bars, $v_3(t)$ and $v_4(t)$ are given by

$$v_3(t) = V_o - v_{st}(t) = V_o - \frac{\sigma_i(t)}{\rho_{st} c_{st}} \tag{5.9a}$$

$$v_4(t) = v_i(t) = \frac{\sigma_i(t)}{\rho c}, \tag{5.9b}$$

where $v_{st}(t)$ and $v_i(t)$ are the particle velocities in the striker and incident bars. As shown in Figs. 5.1, and 5.2, the bar areas are equal. However, the striker bar is supported by a nylon sabot that fits into the gun barrel. As will be shown later, this sabot mass must be

included in the wave analysis for the striker bar. Thus, the density and wave speed for the striker bar are denoted as ρ_{st} and c_{st}, respectively.
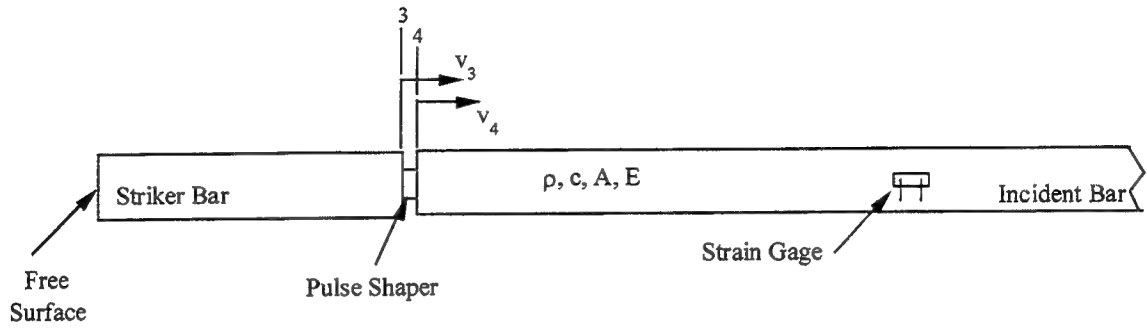
Figure 5.2 Schematic of striker bar, pulse shaper, and incident bar

From eqs (5.4), (5.8), and (5.9)

$$\frac{h_o}{V_o}\dot{\varepsilon}_p(t) = 1 - K\left[\frac{1}{\rho c} + \frac{1}{\rho_{st}c_{st}}\right]\frac{g(\varepsilon_p)}{1-\varepsilon_p}, \qquad \text{for } 0 \leq t < \tau \quad (5.10)$$

which has a solution

$$t = \frac{h_o}{V_o}\int_0^{\varepsilon_p}\left[1 - K\left[\frac{1}{\rho c} + \frac{1}{\rho_{st}c_{st}}\right]\frac{g(x)}{(1-x)}\right]^{-1} dx, \quad \text{for } 0 \leq t < \tau \quad (5.11a)$$

$$K = \frac{\sigma_o a_o}{AV_o}, \quad \text{and} \quad \tau = \frac{2L}{c_{st}} \qquad (5.11b)$$

where τ is equal to two wave transit times in the striker bar. Once $\varepsilon_p(t)$ is calculated from eq (5.11a), the strain in the incident bar can be obtained from eq (5.7b). In addition, eq (5.11a) is valid only as long as the pulse shaper does not expand beyond the bar surfaces. Equation (5.3) shows that the engineering strain in the pulse shaper is limited for a given initial pulse shaper area a_o, such that $a(t) \le A$.

Equation (5.11a) does not explicitly give values for strain in the pulse shaper as a function of time for $0 \le t < \tau$. However, we can obtain closed-form equations for some of the features of the ε_p versus t curve. For small enough values of ε_p, the second term in eq (5.10) can be neglected and

$$\varepsilon_p \approx \frac{V_o t}{h_o} \quad \text{for } t \ll 1. \tag{5.12a}$$

Also, the integral in eq (5.11a) must remain positive because time is always positive. Thus, the largest value of strain in the pulse shaper ε_{pm} is given by

$$\frac{g(\varepsilon_{pm})}{(1-\varepsilon_{pm})} = \frac{1}{K\left[\dfrac{1}{\rho c} + \dfrac{1}{\rho_{st} c_{st}}\right]}. \tag{5.12b}$$

From eqs (5.7a) and (5.12b) the maximum possible stress in the incident bar is given by

$$\sigma_{im} = \frac{V_o}{\left[\dfrac{1}{\rho c} + \dfrac{1}{\rho_{st} c_{st}}\right]}.$$

(5.12c)

Equation (5.12c) gives the value of incident stress for the problem without a pulse shaper. So if the striker bar is long enough, the stress in the incident bar will approach but not exceed σ_{im} given by (5.12c).

We now examine the pulse shaper response for $\tau \le t < 2\tau$. At $t = \tau/2$, the compressive wave travelling to the left in the striker bar shown in Fig. 5.2 reaches the free surface and reflects as a tensile pulse travelling to the right. At $t = \tau$, this right travelling tensile pulse reaches the striker bar/ pulse shaper interface and causes additional reflected and transmitted waves to propagate in the striker and incident bars. We define $-\sigma_{st}(t-\tau)$ as the interface stress from the right travelling tensile pulse. The additional reflected and transmitted interface stresses are defined as $\sigma_r^{1}(t-\tau)$ and $\sigma_t^{1}(t-\tau)$, respectively. Thus, the axial force in the pulse shaper is given by

$$T(t) = \sigma_p(t)a(t) = [\sigma_i(t) + \sigma_t^{1}(t-\tau)]A$$
$$= [\sigma_{st}(t) - \sigma_{st}(t-\tau) + \sigma_r^{1}(t-\tau)]A.$$

(5.13)

Particle velocities at the pulse shaper/ bar interfaces shown in Fig. 5.2 are

$$v_3(t) = V_o - v_{st}(t) - v_{st}(t-\tau) - v_r^1(t-\tau) \tag{5.14a}$$

$$= V_o - \frac{\sigma_{st}(t)}{\rho_{st}c_{st}} - \frac{\sigma_{st}(t-\tau)}{\rho_{st}c_{st}} - \frac{\sigma_r^1(t-\tau)}{\rho_{st}c_{st}}$$

$$v_4(t) = v_i(t) + v_t^1(t-\tau) = \frac{\sigma_i(t)}{\rho c} + \frac{\sigma_t^1(t-\tau)}{\rho c}. \tag{5.14b}$$

From eqs (5.8), (5.13), and (5.14), the engineering strain rate is

$$h_o\dot{\varepsilon}_p(t) = V_o - \frac{\sigma_{st}(t)}{\rho_{st}c_{st}} - \frac{\sigma_{st}(t-\tau)}{\rho_{st}c_{st}} - \frac{\sigma_r^1(t-\tau)}{\rho_{st}c_{st}} - \frac{\sigma_i(t)}{\rho c} - \frac{\sigma_t^1(t-\tau)}{\rho c}. \tag{5.15}$$

Now, we solve for $\sigma_r^1(t-\tau)$ from eq (5.13) and eliminate $\sigma_r^1(t-\tau)$ from eq (5.15). Thus,

$$h_o\dot{\varepsilon}_p(t) = V_o - \left[\frac{1}{\rho c} + \frac{1}{\rho_{st}c_{st}}\right]\left[\sigma_i(t) + \sigma_t^1(t-\tau)\right] - \frac{2\sigma_{st}(t-\tau)}{\rho_{st}c_{st}}. \tag{5.16}$$

From eqs (5.13), (5.6), and (5.3), the stress in the incident bar is

$$\sigma_i(t) + \sigma_t^1(t-\tau) = \frac{\sigma_p(t)a(t)}{A} = \frac{\sigma_o g(\varepsilon_p)}{(1-\varepsilon_p)}\frac{a_o}{A} \tag{5.17}$$

and from eq (5.7a)

$$\sigma_{st}(t-\tau) = \frac{\sigma_o g(\varepsilon_p(t-\tau))}{(1-\varepsilon_p(t-\tau))} \frac{a_o}{A}.$$

(5.18)

Finally, we substitute eqs (5.17) and (5.18) into eq (5.16) and obtain

$$\frac{h_o}{V_o}\dot{\varepsilon}_p(t) = 1 - K\left[\frac{1}{\rho\,c} + \frac{1}{\rho_{st}c_{st}}\right]\frac{g(\varepsilon_p(t))}{1-\varepsilon_p(t)} - \frac{2K}{\rho_{st}c_{st}}\frac{g(\varepsilon_p(t-\tau))}{1-\varepsilon_p(t-\tau)}, \text{ for } \tau \leq t < 2\tau. \quad (5.19)$$

The solution to eq (5.19) is

$$t = \tau + \frac{h_o}{V_o}\int_{\varepsilon_p^1}^{\varepsilon_p}\left[1 - K\left[\frac{1}{\rho\,c} + \frac{1}{\rho_{st}c_{st}}\right]\frac{g(x)}{1-x} - \frac{2K}{\rho_{st}c_{st}}\frac{g(\varepsilon_p(t-\tau))}{1-\varepsilon_p(t-\tau)}\right]^{-1}dx,$$

$$\text{for } \tau \leq t < 2\tau, \quad (5.20)$$

where ε_p^1 is the strain in the pulse shaper at $t = \tau$, $\varepsilon_p(t-\tau)$ is calculated from eq (5.11a) with the appropriate time shift, and K and τ are defined by eq (5.11b).

Equation (5.20) gives the total strain in the pulse shaper for $\tau \leq t < 2\,\tau$. The strain in the incident bar is calculated from eq (5.7b) using the values of ε_p for $\tau \leq t < 2\tau$ calculated from eq (5.20). As previously mentioned, the pulse shaper must not expand beyond the bar surfaces, so the engineering strain in the pulse shaper is limited by eq (5.3) for an initial pulse shaper area a_o, such that $a(t) \leq A$. In addition, eqs (5.19) and (5.20) are valid only if the pulse shaper remains in contraction or $\dot{\varepsilon}_p(t)$ remains positive

in eq (5.8). Thus for the particle velocities shown in Fig 5.2, $(v_3 - v_4) \geq 0$. When $v_3 < v_4$, the pulse shaper will be modeled as elastic unloading.

As long as a < A and $v_3 > v_4$, the pulse shaper continues to deform in compression. We repeated the previous analyses for multiple reverberations in the striker bar. For $t > 2\tau$, the general versions of eqs (5.16) and (5.19) are

$$h_o \dot{\varepsilon}_p(t) = V_o - \left[\frac{1}{\rho c} + \frac{1}{\rho_{st} c_{st}}\right]\left[\sigma_i(t) + \sigma_t{}^1(t-\tau) + \sigma_t{}^2(t-2\tau) + \ldots \sigma_t{}^n(t-n\tau)\right]$$

$$- \frac{2}{\rho_{st} c_{st}}\left[\sigma_{st}(t-\tau) + \sigma_r{}^1(t-2\tau) + \sigma_r{}^2(t-3\tau) + \ldots \sigma_r{}^{(n-1)}(t-n\tau)\right],$$

$$\text{for } n\tau \leq t < (n+1)\tau. \quad (5.21)$$

and

$$\frac{h_o}{V_o}\dot{\varepsilon}_p(t) = 1 - K\left[\frac{1}{\rho c} + \frac{1}{\rho_{st} c_{st}}\right]\frac{g(\varepsilon_p)}{1-\varepsilon_p}$$

$$- \frac{2K}{\rho_{st} c_{st}}\left[\frac{g(\varepsilon_p(t-\tau))}{1-\varepsilon_p(t-\tau)} + \frac{g(\varepsilon_p(t-2\tau))}{1-\varepsilon_p(t-2\tau)} + \ldots \frac{g(\varepsilon_p(t-n\tau))}{1-\varepsilon_p(t-n\tau)}\right],$$

$$\text{for } n\tau \leq t < (n+1)\tau. \quad (5.22)$$

Now consider the situation when $v_3 \leq v_4$ and the pulse shaper unloads during $\tau \leq t < 2\tau$ at $t = t^*$. We assume the pulse shaper unloads elastically (Fig. 5.3) and that the unloading stress is given by

$$\sigma_u(t) = \sigma_p^* - E_p(\varepsilon_p^* - \varepsilon_p) \qquad (5.23)$$

where $\sigma_p{}^*$, $\varepsilon_p{}^*$ are the peak stress and strain at $t = t^*$ when $v_3 = v_4$, and E_p is the unloading Young's modulus.

Equation (5.16) gives the strain rate of the pulse shaper in terms of stress components in the incident and transmission bars for $\tau \le t < 2\tau$. For $\tau \le t < t^*$, the stress in the incident bar at the pulse shaper/ incident bar interface is given by eq (5.17). However, for $t^* \le t < 2\tau$, the pulse shaper is unloading. From a force balance at the pulse shaper/ incident bar interface, the stress in the incident bar is

$$\sigma_i(t) + \sigma_t{}^1(t-\tau) = \frac{a_o\,\sigma_u(t)}{A(1-\varepsilon_p)}, \text{ for } t^* \le t < 2\tau. \qquad (5.24)$$

Equation (5.24) assumes that the stress-strain law for the pulse shaper is given by eq (5.23) and that $\sigma_u(t) \le \sigma_p{}^*$. The last term in eq (5.16) is the interface stress from the right travelling tensile pulse coming from the free surface of the striker bar. Since this stress component is delayed by $t = \tau$, $\sigma_{st}(t-\tau)$ is given by eq (5.18). We substitute eqs (5.18) and (5.24) into eq (5.16) and obtain

$$\frac{h_o}{V_o}\dot{\varepsilon}_p(t) = 1 - K\left[\frac{1}{\rho_i c_i} + \frac{1}{\rho_{st} c_{st}}\right]\frac{\sigma_p{}^* - E_p(\varepsilon_p{}^* - \varepsilon_p)}{\sigma_o(1-\varepsilon_p)} - \frac{2K}{\rho_{st} c_{st}}\frac{g(\varepsilon_p(t-\tau))}{1-\varepsilon_p(t-\tau)},$$
$$\text{for } t^* \le t < 2\tau \qquad (5.25)$$

which has solution

$$t = t^* + \frac{h_o}{V_o} \int_{\varepsilon_p^*}^{\varepsilon_p} \left[1 - K \left[\frac{1}{\rho_i c_i} + \frac{1}{\rho_{st} c_{st}} \right] \frac{\sigma_p^* - E_p(\varepsilon_p^* - x)}{\sigma_o(1-x)} - \frac{2K}{\rho_{st} c_{st}} \frac{g(\varepsilon_p(t-\tau))}{1 - \varepsilon_p(t-\tau)} \right]^{-1} dx,$$

$$\text{for } t^* \le t < 2\tau \quad (5.26)$$

where t^* is the time when $v_3 = v_4$ and unloading begins.

For many cases, additional wave reverberations in the striker bar are required to completely unload the pulse shaper. We repeated the previous analysis and obtained equations for the pulse shaper response for the onset of unloading between $\tau \le t < 2\tau$ and responses during $2\tau \le t < 3\tau$. Thus,

$$\frac{h_o}{V_o} \dot{\varepsilon}_p(t) = 1 - K \left[\frac{1}{\rho c} + \frac{1}{\rho_{st} c_{st}} \right] \frac{\sigma_p^* - E_p(\varepsilon_p^* - \varepsilon_p)}{\sigma_o(1-\varepsilon_p)} - \frac{2K}{\rho_{st} c_{st}} \frac{g(\varepsilon_p(t-\tau))}{1 - \varepsilon_p(t-\tau)} -$$

$$\frac{2K}{\rho_{st} c_{st}} \frac{g(\varepsilon_p(t-2\tau))}{1 - \varepsilon_p(t-2\tau)}, \qquad \text{for } 2\tau \le t < \tau + t^* \quad (5.27a)$$

$$\frac{h_o}{V_o} \dot{\varepsilon}_p(t) = 1 - K \left[\frac{1}{\rho c} + \frac{1}{\rho_{st} c_{st}} \right] \frac{\sigma_p^* - E_p(\varepsilon_p^* - \varepsilon_p)}{\sigma_o(1-\varepsilon_p)} -$$

$$\frac{2K}{\rho_{st} c_{st}} \frac{\sigma_p^* - E_p(\varepsilon_p^* - \varepsilon_p(t-\tau))}{\sigma_o(1 - \varepsilon_p(t-\tau))} - \frac{2K}{\rho_{st} c_{st}} \frac{g(\varepsilon_p(t-2\tau))}{1 - \varepsilon_p(t-2\tau)}, \text{ for } \tau + t^* \le t < 3\tau. \quad (5.27b)$$

Two response equations for $2\tau \le t < 3\tau$ are required because of time delay terms in eq (5.21) that correspond to reverberations in the striker bar. In particular, the third terms in eqs (5.27a) and (5.27b) are different and the other terms are the same. For $t \le t^*$ the pulse shaper is loading and eq (5.6) applies. By contrast, for $t \ge t^*$ the pulse shaper is unloading and eq (5.23) applies.
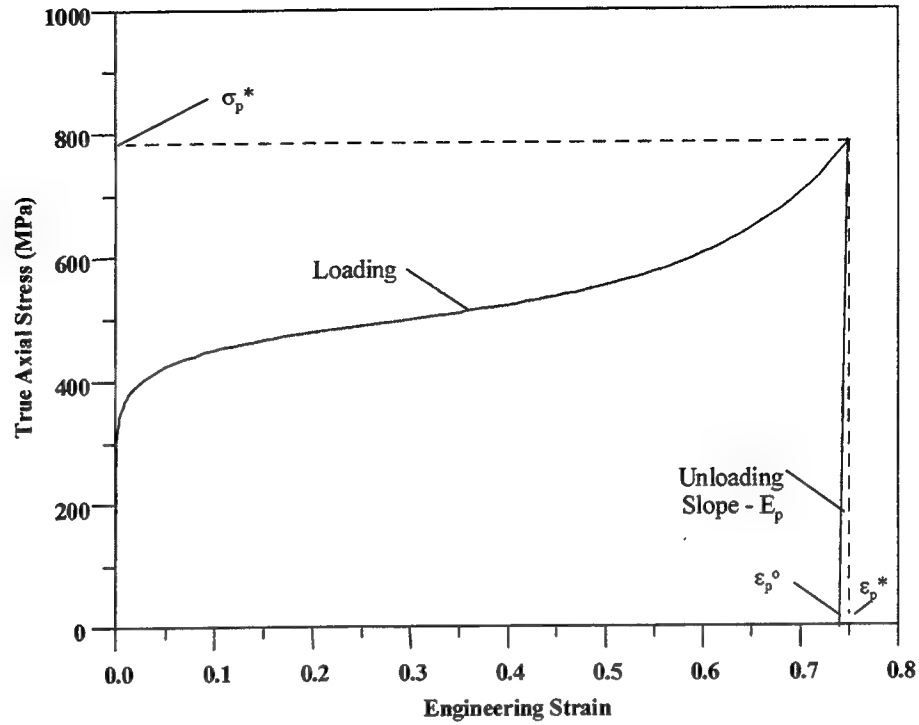
Figure 5.3 Pulse shaper response function in loading and unloading

For the situation where the pulse shaper is not fully unloaded at $t = 3\tau$, we again repeated the previous analysis and obtained equations for the pulse shaper response for unloading between $\tau \leq t < 2\tau$ and responses during $3\tau \leq t < 4\tau$. Thus,

$$\frac{h_o}{V_o}\dot{\varepsilon}_p(t) = 1 - K\left[\frac{1}{\rho c} + \frac{1}{\rho_{st}c_{st}}\right]\frac{\sigma_p^* - E_p(\varepsilon_p^* - \varepsilon_p)}{\sigma_o(1-\varepsilon_p)} -$$

$$\frac{2K}{\rho_{st}c_{st}}\left[\frac{\sigma_p^* - E_p(\varepsilon_p^* - \varepsilon_p(t-\tau))}{\sigma_o(1-\varepsilon_p(t-\tau))} + \frac{g(\varepsilon_p(t-2\tau))}{1-\varepsilon_p(t-2\tau)} + \frac{g(\varepsilon_p(t-3\tau))}{1-\varepsilon_p(t-3\tau)}\right],$$

$$\text{for } 3\tau \leq t < 2\tau + t^* \quad (5.28a)$$

$$\frac{h_o}{V_o}\dot{\varepsilon}_p(t) = 1 - K\left[\frac{1}{\rho c} + \frac{1}{\rho_{st}c_{st}}\right]\frac{\sigma_p^* - E_p(\varepsilon_p^* - \varepsilon_p)}{\sigma_o(1 - \varepsilon_p)} -$$

$$\frac{2K}{\rho_{st}c_{st}}\left[\frac{\sigma_p^* - E_p(\varepsilon_p^* - \varepsilon_p(t - \tau))}{\sigma_o(1 - \varepsilon_p(t - \tau))} + \frac{\sigma_p^* - E_p(\varepsilon_p^* - \varepsilon_p(t - 2\tau))}{\sigma_o(1 - \varepsilon_p(t - 2\tau))} + \frac{g(\varepsilon_p(t - 3\tau))}{1 - \varepsilon_p(t - 3\tau)}\right],$$

$$\text{for } 2\tau + t*\tau \leq t < 4\tau. \quad (5.28b)$$

Numerical evaluations helped us understand the elastic unloading process that starts when $v_3 = v_4$ and continues for $v_4 > v_3$ (see Fig. 5.2). We found that the terms corresponding to the striker impact dominated values of v_3 and v_4. For example, the dominant term in eq (5.14a) for $v_3(t)$ is $v_{st}(t) = \sigma_{st}(t)/\rho_{st}c_{st}$ and the dominant term in eq (5.14b) for $v_4(t)$ is $v_i(t) = \sigma_i(t)/\rho c$. As the pulse shaper stress decreases during unloading, $\sigma_{st}(t)$ and $\sigma_i(t)$ decreases rapidly which also causes v_3 and v_4 to decrease rapidly. As $\sigma_{st}(t)$ and $\sigma_i(t)$ decrease, $v_3(t)$ decreases much more slowly than $v_4(t)$. For some cases, the unloading condition $v_3(t) \leq v_4(t)$ may be violated and the pulse shaper will begin elastic loading. Due to the heavy dependence of $\sigma_i(t)$ on $v_4(t)$, this reloading is short lived, occurs frequently, and is a main reason why it is not uncommon for the unloading of the pulse shaper to be long ($\sim$100 μs). The unload/ reload cycles in the pulse shaper eventually reduce the pulse shaper stress to zero and the striker and incident bars separate from each another.

In summary, we have presented a pulse shaping model for loading and unloading of the pulse shaper material. The pulse shaper material is taken as incompressible and assumed to undergo homogeneous deformation. Loading is governed by a general, one-dimensional stress-strain relationship (eq (5.6)) and unloading is taken as linear (eq

(5.23)). A general loading equation for multiple reverberations in the striker bar is developed and given by eq (5.22). The unloading procedure is more complicated and only the case for unloading at t* between $\tau \leq t < 2\tau$ is presented. For other cases where unloading starts at times greater than 2τ, we developed a Fortran computer code (see Appendix A) to calculate the pulse shaper response.

5.3 PULSE SHAPER MATERIAL RESPONSE

We conducted experiments with both OFHC and C11000 (Lewis, 1979) copper pulse shapers and showed that the C11000 pulse shapers could be driven to larger strains without breakup and remained more circular after deformation. In addition, we present results for both hard and annealed C11000 copper. The hard copper was received from the supplier and measured 45 on the Rockwell B scale (HRB 45). We heated the as-received copper for 2 hours at 800° F to obtain the annealed copper.

The original pulse shaper geometries had thicknesses ranging from 0.8 mm to 1.6 mm and thickness-to-diameter ratios ranging from 0.16 to 0.50. As discussed by Kolsky (1949), Davies and Hunter (1963), and Baron (1956), these geometries can create a complicated two-dimensional stress-state in the pulse shapers due to inertial and frictional effects. However, we are only attempting to produce a desired strain-time pulse in the incident bar and are not attempting to obtain stress-strain data for the pulse shapers. Thus $\sigma_p = \sigma_o \, g(\varepsilon_p)$ given by eq (5.6) should not be construed as a constitutive material description of the pulse shaper, but as a one-dimensional resistance function.

For the hard and annealed, C11000 copper pulse shapers, we determined that a resistance function of the form

$$\sigma_p = \frac{\sigma_o \varepsilon_p^n}{1 - \varepsilon_p^m} \tag{5.29}$$

could accurately curve fit our data with σ_o, n, and m as adjustable parameters. Figure 5.4 shows the hard copper (HRB 45) resistance function with $\sigma_o = 550$ MPa, n = 0.0875, and m = 4.0. The dashed lines are split Hopkinson pressure bar data from samples with an original diameter of 9.52 mm and an original thickness of 6.4 mm. These data reached engineering strain magnitudes of 0.44 and 0.47 with strain rates of 3,200 and 3,500 s^{-1}, respectively. The data points in Fig. 5.4 are from pulse shaping experiments where we used an end-point method. For each data point in Fig. 5.4 the engineering strain is the final strain calculated from eq (5.2). From eqs (5.3) and (5.4), the true axial stress in the pulse shaper can be expressed in terms of strain in the incident bar as

$$\sigma_p = \frac{EA}{a_o}(1 - \varepsilon_p) \cdot \varepsilon_i \tag{5.30}$$

The corresponding true axial stress for each data point in Fig. 5.4 is that value corresponding to the maximum strain measured with the incident bar. Thus, maximum strain is obtained from a post-test thickness measurement, and maximum stress is calculated from eq (5.30) with the maximum measured strain in the incident bar. Figure

5.4 shows that the end-point data and Hopkinson bar data are in good agreement to strains of about 0.45. The end-point method was required to obtain strain data to about 0.85.

Figure 5.5 shows resistance functions for 0.79 and 1.29-mm-thick annealed copper pulse shapers. The resistance function for the 0.79-mm-thick pulse shapers lies above that for the 1.29-mm-thick pulse shapers and that suggests a slight rate effect for the material response. The parameters in eq (5.29) for the annealed pulse shapers with original thickness $h_o = 0.79$ mm are $\sigma_o = 750$ MPa, $n = 0.37$, and $m = 4.25$; for $h_o = 1.29$ mm, the parameters are $\sigma_o = 625$ MPa, $n = 0.32$, and $m = 4.25$. In addition, we present results from five Hopkinson bar experiments. The data with permanent strains of 0.13, and 0.18 had an original diameter of 9.53 mm, an original thickness of 12.70 mm, and strain rates of 2,100, and 3,000 s^{-1}, respectively. The Hopkinson bar data with a permanent strain of 0.25 had an original diameter of 9.53 mm, an original thickness of 6.35 mm, and strain rate of 4,370 s^{-1}; whereas, the Hopkinson bar data with permanent strains of 0.36, and 0.54, had an original diameter and thickness of 6.35 mm, and strain rates of 5,800 s^{-1} each. The end-point method data points for the 1.29-mm-thick pulse shapers are in close agreement with the Hopkinson bar data for strains to 0.55. Again, the end-point method was required to obtain strain data to about 0.85.
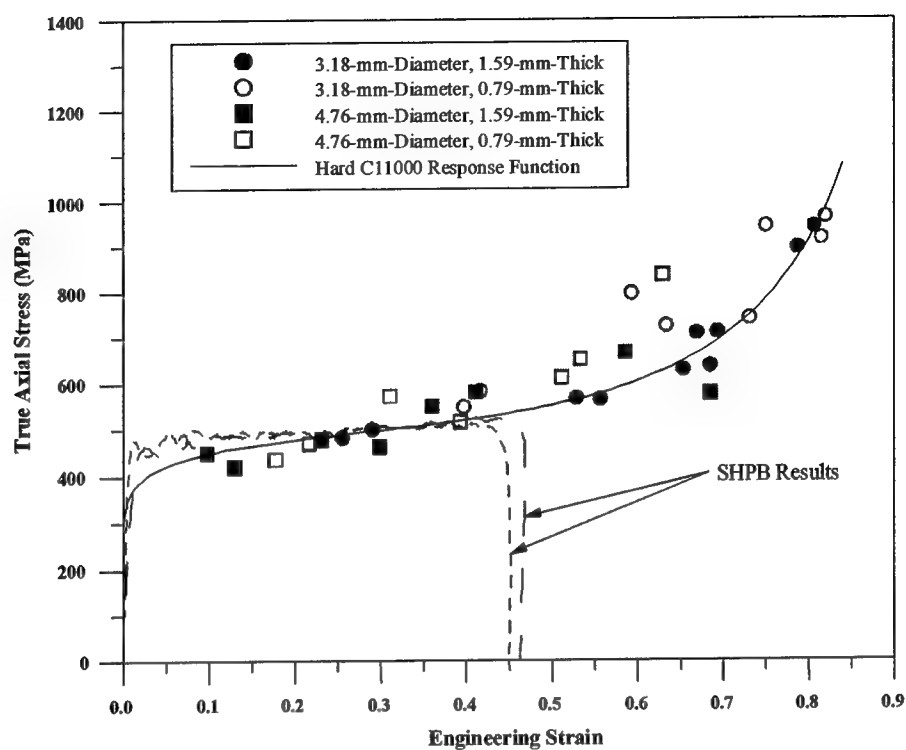
Figure 5.4 Data and response function for hard (HRB 45) C11000 copper
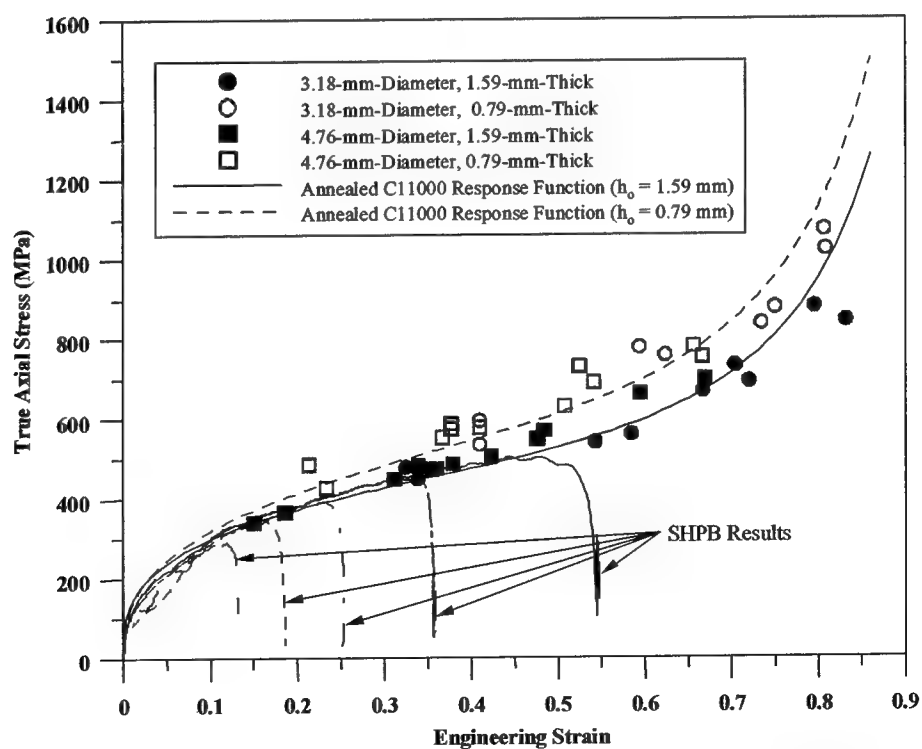
Figure 5.5 Data and response functions for annealed C11000 copper

5.4   INCIDENT STRAIN FROM PULSE SHAPED EXPERIMENTS

We modified the split Hopkinson pressure bar apparatus by shaping the incident pulses such that test samples are in dynamic stress equilibrium and have a nearly constant strain rate over most of the test duration. To obtain reliable dynamic, stress-strain data for brittle materials such as rocks or ceramics that have failure strains less than a few percent, the incident strain pulse should have a linear or quasi-linear rise. We will use the pulse shaping techniques described in this chapter to conduct experiments with limestone and glass ceramic samples. Results will be presented in Chapters 6 and 7.

Figures 5.6 and 5.7 show data and model predictions for incident stresses from pulse shaped experiments with hard (HRB 45) and annealed C11000 pulse shapers, respectively. The pulse shapers had original thicknesses and diameters of 1.6 mm and 4.8 mm, respectively. The 12.7-mm-diameter striker and incident bars shown in Fig. 5.1 had lengths of 152 and 2130 mm, respectively. As discussed in Chapter 3, the bars were made from high-strength maraging VascoMax C350 steel (Vasco-Pacific, 1998) and have density $\rho = 8100$ kg/m^3, Young's modulus $E = 200$ GPa, and bar wave velocity $c = 4970$ m/s. The strain gages shown in Fig. 5.2 are located at 1060 mm from the impact surface on the incident bar.

The striker bar is launched by a gas gun that has a bore diameter larger than the striker bar diameter, so the striker bar is fitted with two nylon bore-riders (sabots). The bore-riders are nylon cylinders that make a snug fit for the striker bar in the gun bore and provide a good alignment for projectile launch. We learned early in this study that the added mass of the bore-riders needed to be included in the striker bar wave analysis for

predicting incident strain pulses. This added mass is included in the derivation of the elementary theory for the striker bar by using an effective density ρ_{st}, where ρ_{st} is the total mass of the striker bar and bore-riders divided by the volume of the striker bar. The wave velocity for the striker bar is taken as $c_{st}^2 = E/\rho_{st}$, where E is Young's Modulus for the striker bar. Model predictions and measured strain pulses are in good agreement with this approximation.

We previously defined τ with eq (5.11b) as the time for two wave transit times in a striker bar of length L. For the data and model predictions shown in Figs. 5.6 and 5.7, the experiments were conducted with $\rho_{st} = 8{,}750$ kg/m^3, $c_{st} = 4{,}780$ m/s, L = 152 mm, $\tau = 63.6$ μs, and a striking velocity $V_o = 17.5$ m/s. Both Figs. 5.6 and 5.7 show that the onset of unloading is at about $t^* = 110$ μs. So $\tau \le t^* < 2\tau$, and the loading strain in the pulse shaper is calculated from eq (5.11a) for $0 \le t < \tau$ and from eq (5.20) for $\tau \le t < t^*$. However as with all Hopkinson experimental techniques, we do not measure stresses or strains in the pulse shaper but infer these quantities through a wave analysis and downstream strain measurements on the incident bar. Thus, the model that predicts incident bar stresses shown in Figs. 5.6 and 5.7 are calculated from eqs (5.6), (5.7a), and (5.29).

For $t \ge t^*$ or t greater than about 110 μs, the pulse shaper is unloading. We take the unloading Young's modulus as $E_p = 117$ GPa in eq (5.23) and calculate the unloading pulse shaper strain responses for $t^* \le t < 2\tau$ ($2\tau = 127$ μs) from eq (5.26) and for $2\tau \le t < 3\tau$ ($3\tau = 191$ μs) from eqs (5.27a) and (5.27b). The incident bar stresses predicted for

unloading in Figs. 5.6 and 5.7 can be expressed in terms of the strain in the pulse shaper. We combine eqs (5.3), (5.4), and (5.23) and obtain

$$\sigma_i = \frac{a_o}{A(1-\varepsilon_p)}\sigma_p^* - E_p(\varepsilon_p^* - \varepsilon_p) \qquad (5.31)$$

where σ_p^* and ε_p^* are the peak pulse shaper stress and strain at the onset of unloading.

A common feature for the hard copper data is a well defined kink found early in the incident stress-time data. The kink shown in Fig. 5.6 has an incident stress level of about 70 MPa and is caused by the transition from elastic to plastic deformation in the pulse shaper. The incident stress level of this kink can be adjusted by changing the initial pulse shaper diameter. In addition, the data in Fig. 5.7 shows the kink is removed for an annealed copper pulse shaper that has a very small yield strength.

In Appendix B, we present results from a total of 32, SHPB experiments with hard (HRB = 45) and annealed C11000 copper pulse shapers to study the accuracy of the pulse shaping model and resistance functions developed in this chapter. We varied striker bar lengths (50.8 and 152.4 mm), nominal striking velocities (8.5 and 17.5 m/s), pulse shaper diameters (3.2 and 4.8 mm), and pulse shaper thicknesses (1.6 and 0.8 mm) in order to exercise our model over a variety of different strain environments. Data and model predictions are shown to be in good agreement.
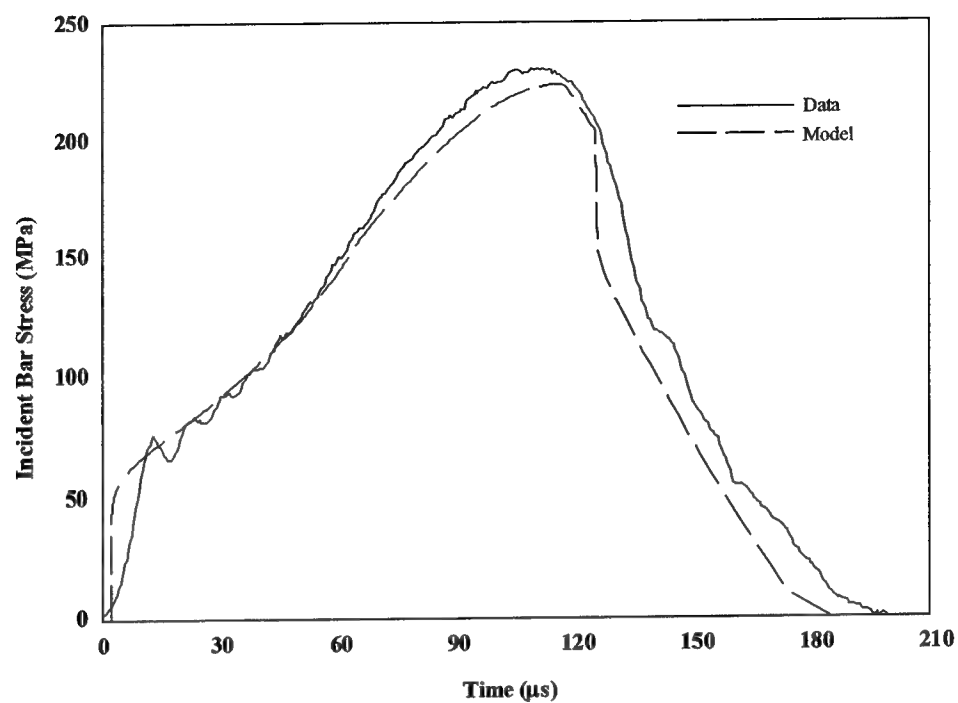
Figure 5.6 Incident bar stress data and model prediction for a hard C11000 copper pulse shaper
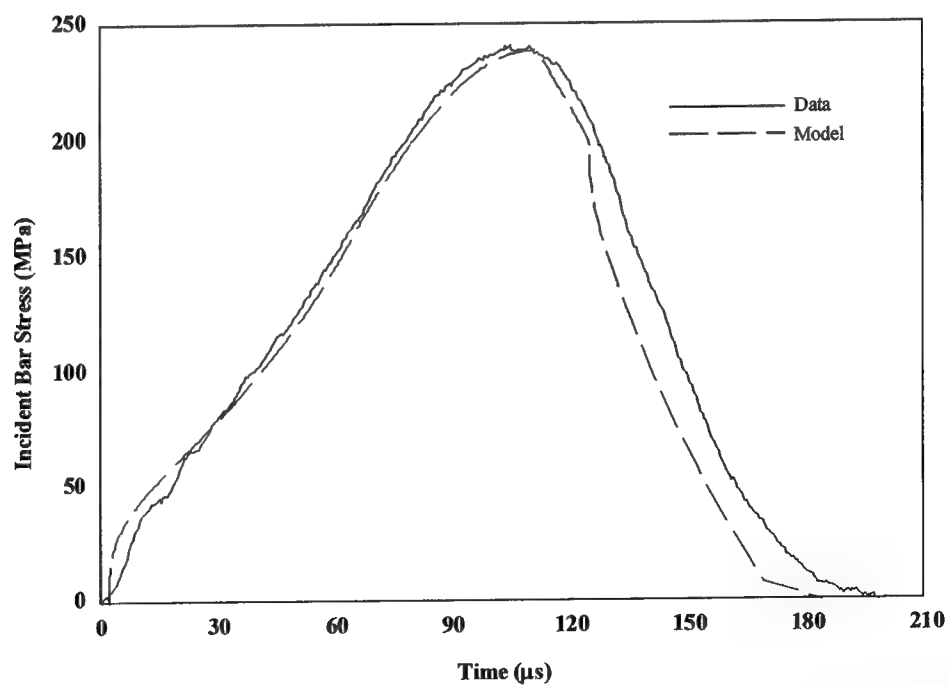
Figure 5.7 Incident bar stress data and model prediction for an annealed C11000 copper pulse shaper

CHAPTER 6

COMPRESSIVE BEHAVIOR OF AN INDIANA LIMESTONE

6.1   BACKGROUND

In Chapter 2, we presented results from three sets of depth-of-penetration experiments with limestone targets and steel rod projectiles with diameters of 7.1, 12.7, and 25.4 mm. Results from these experiments show that the target resistance increased with decreasing projectile diameter. Based on previous analyses by Warren and Forrestal (1998) for aluminum targets, we suspected that the target strength dependence on projectile diameter could be attributed to strain-rate effects in the target material. As a first step to developing a mechanics based understanding for the dynamic material response of these limestone targets, it was necessary to develop the experimental and analytical tools to properly test brittle materials dynamically. We developed an experimental split Hopkinson pressure bar (SHPB) facility specifically for brittle materials testing, and in Chapters 4 and 5 presented analytic models to help us conduct valid SHPB experiments. In this chapter, we present unconfined compressive strength data on Indiana limestone specimens at strain rates between 10^{-5} to 3×10^2 s^{-1}. We show that the dynamic unconfined compressive strength for this limestone material is about double that obtained from the quasi-static experiments. Possible mechanisms for this large strength enhancement will be discussed.

6.2   INDIANA LIMESTONE

As mentioned previously, the Indiana limestone used in this work was obtained from the Elliot Stone Company, Bedford Indiana. This material can be classified as a carbonate rock containing over 90% calcite and less than 10% quartz, and made up of an intermediate mixture of oolites and microfossil debris cemented with calcite (Podnieks, Chamberlain, and Thill, 1972, and Pettijohn, 1975). The limestone had an average bulk density ρ_s = 2320 kg/m^3 and a measured grain density ρ_g = 2700 kg/m^3, which gives an average porosity of 14.5%. The Young's modulus, E_s = 24 GPa, for the limestone was measured directly from the linearized slope of quasi-static compression tests presented in this chapter and the bar wave velocity c_s = 3,200 m/s was calculated from $c_s = (E_s/\rho_s)^{1/2}$.

Limestone cores, 13-mm in diameter, were drilled from a block perpendicular to the bedding plane with a thin walled diamond core barrel. The core was cut to a rough length and the ends ground flat and parallel to within ±0.025 mm. The outside diameter of the sample was then machined to a final diameter of 12.7 mm with the sides perpendicular to the ends of the sample to within 0.1°.

6.3   EXPERIMENTS

6.3.1   Servo-Hydraulic Loading

A total of 23 compression tests were performed using a hydraulically driven Materials Test System (MTS 810), which is shown schematically in Fig. 6.1. A load cell

(MTS model 1210 AP-5K-B) was used to measure the axial load history and two different size MTS extensometers (model 632.31E-24 for 12.7- and 19.1-mm long specimens and 632.25B-20 for 25.4-mm-long specimens) were used to measure the axial deformation of the test specimens. The MTS actuator was moved at a constant velocity in displacement control mode in order to attain a constant strain rate in the limestone samples that behave nearly linear-elastic until just prior to failure. Varying strain rates were achieved by altering the actuator velocity. A personal computer (ALR 386) was used through a software program "Testlink" to control the MTS system and a Tektronix TDS 420A digital oscilloscope recorded the axial load and deformation data from each test.

Figure 6.1 Schematic of MTS loading system

General practices for preparing and testing rock materials in compression are described in the American Society for Testing and Materials (ASTM) standards D 4543 (1991) and D 2664 (1991), respectively. From such standards, general testing procedures can be developed that help eliminate testing variables (such as grain size and edge effects) that could easily change the strength values obtained for many rock materials. The standards are meant to be a guide for testing all rock materials, and as such could be too conservative when applied to some types of rock (see Hawkes and Mellor, 1970, and Farmer, 1983).

ASTM recommends that the diameter of a rock specimen be at least ten times the largest mineral grain size, and since the grain size of Indiana limestone is between 0.15 and 1.0 mm (Podnieks, Chamberlain, and Thill, 1972), specimen diameters of at least 12.7 mm were used for this work. It is also recommended that a rock specimen have a length-to-diameter (l_o/D) ratio of 2.0 to 2.5, which for a 12.7-mm-diameter specimen would result in a length of at least 25.4 mm. This proposed length is relatively long by SHPB standards. Since we would like to test the same length specimens in both the servo-hydraulic and SHPB test devices to eliminate test variability, it was necessary to investigate the effect different l_o/D ratios on the compressive strength of Indiana limestone.

Compressive strengths from 23 servo-hydraulic experiments conducted with 12.7-mm-diameter by 12.7-, 19.1-, and 25.4-mm-long specimens at strain rates between 10^{-5} and 3×10^{-2} s^{-1} are presented in Fig. 6.2. Within the data scatter, the compressive strengths of the limestone are about the same for all three l_o/D ratios tested. Stress-strain data

presented in Figs. 6.3-6.5 show a general trend of increased compressive strength with increased strain rates. Figures 6.3-6.5 also show that the limestone behaves nearly linear-elastic, with a Young's modulus of approximately 24 GPa, until just before failure. We will use this modulus in the next section for the SHPB models developed in Chapter 4 that predict equilibrium and constant strain rate in a sample for a given ramp incident pulse.
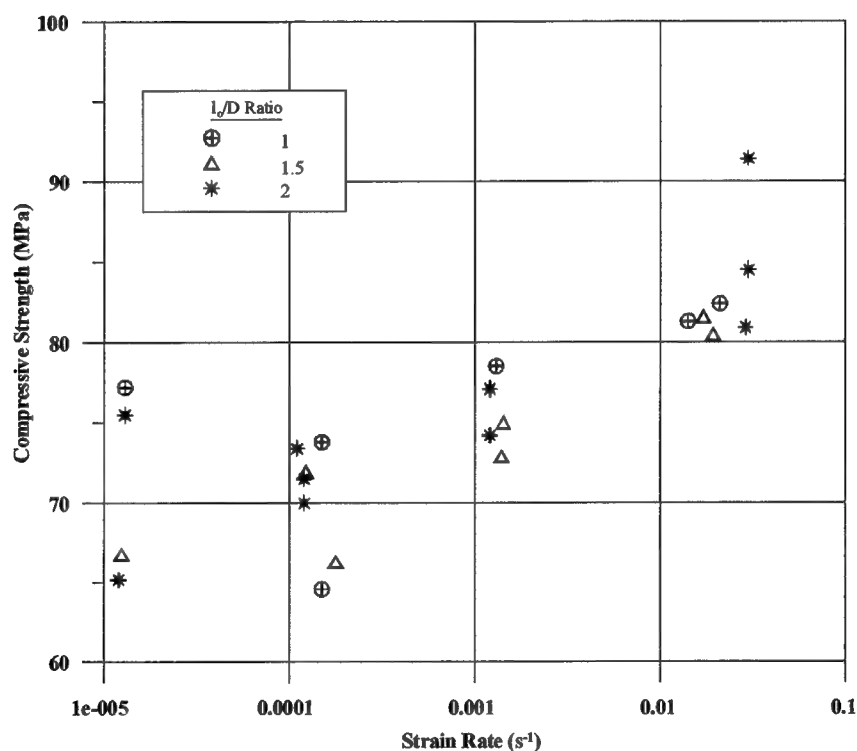
Figure 6.2 Compressive strengths of Indiana limestone samples with various aspect ratios and rates of strain
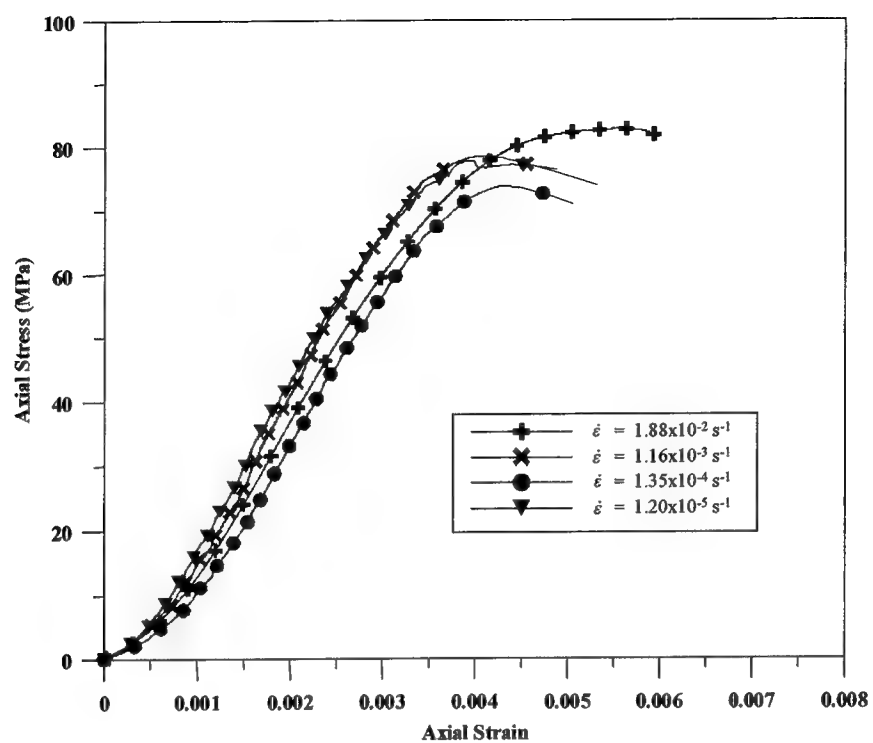
Figure 6.3 Stress-strain data for 12.7-mm-diameter by 12.7-mm-long limestone specimens
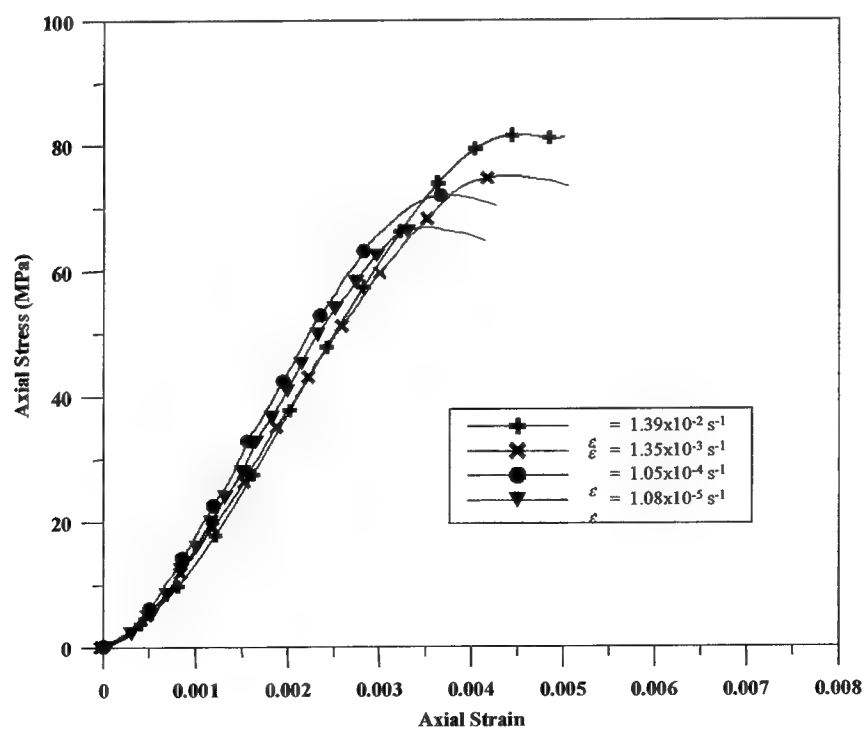
Figure 6.4 Stress-strain data for 12.7-mm-diameter by 19.1-mm-long limestone specimens
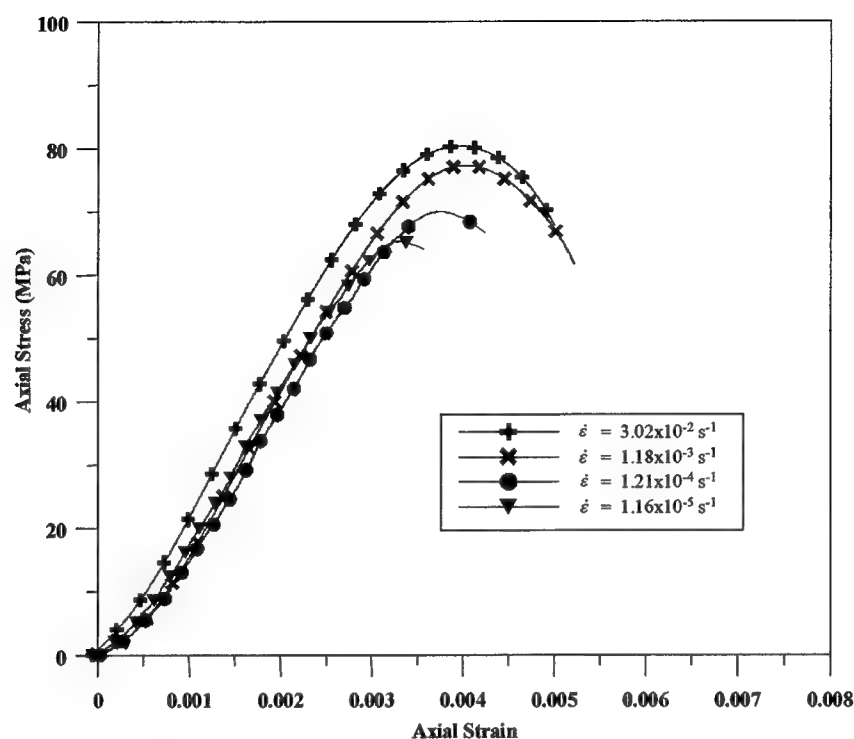
Figure 6.5 Stress-strain data for 12.7-mm-diameter by 25.4-mm-long limestone specimens

6.3.2   Modified Split Hopkinson Pressure Bar

Models developed in Chapter 4 predict that a nondispersive ramp pulse in the incident bar is required for testing brittle materials that have a linear stress-strain response to failure. In Chapter 5, we developed the pulse shaping models and techniques needed to produce such a pulse. In this section, we present results from two experiments on Indiana limestone that demonstrate our modified SHPB technique. Data from experiments show that the samples are in dynamic stress equilibrium and have nearly constant strain rates over most of the duration of the tests. We also carefully bracket sample failure with one test where the sample fails with catastrophic damage and a

second test where the sample is recovered intact. The sample had a length and diameter of 12.7 mm, and the sample and bar diameters were equal. The high strength steel incident and transmission bars had lengths of 2130 and 915 mm, respectively. Strain gages shown in Fig. 3.4 are located at 1065 mm from the impact surface of the incident bar and 229 mm from the sample/ bar interface on the transmission bar. To obtain a nearly linear ramp pulse in the incident bar, a 3.97-mm-diameter, 0.79-mm-thick, annealed C11000 copper pulse shaper was used. All the above mentioned parameters remained fixed for the two experiments presented in this section. However, the first experiment used a 154-mm-long, steel striker bar, and the second experiment used a 51-mm-long, steel striker bar. Both striker bars were launched to a striking velocity of 13.9 m/s.

Figure 6.6 shows the measured incident stress pulse and a prediction from our pulse shaping model for a 154-mm-long, steel striker bar with a striking velocity of 13.9 m/s. Note that the incident stress pulse is nearly a linear ramp for about 75 μs and has a stress loading rate of about M = 3.3 MPa/μs. Incident, reflected, and transmitted strain pulses presented in Fig. 6.7 show that the high frequency oscillations that appear in Fig. 3.10 are eliminated with pulse shaping. Thus, data analyses that use the elementary bar theory should be more accurate for pulse shaped experiments. Figure 6.8 presents stresses in the sample at the incident bar/ sample interface σ_1 and the sample/ transmission bar interface σ_2 calculated from eqs (3.26a) and (3.26b) that use the measured strain signals. We also show that the model prediction from eqs (4.2) and (4.7b) are in good agreement with the measured stresses and that σ_1 and σ_2 are in close

agreement. Thus, the sample is in nearly a state of dynamic stress equilibrium. Figure 6.8 also shows the predicted and measured strain rates versus time. Strain rate is nearly constant for 15 μs < t < 50 μs. At about 50 μs, the limestone sample begins to fail. When failure starts, the sample is no longer in a state of homogeneous deformation and the valid range for the experiment is over. Post-test observations showed that the sample eventually experienced catastrophic damage.
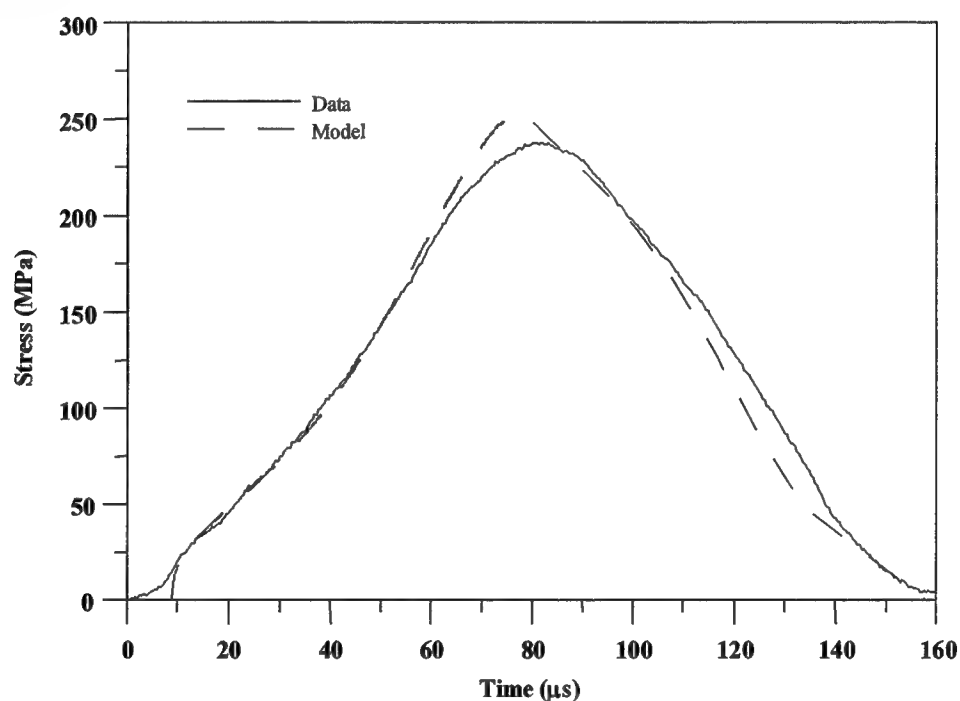
Figure 6.6 Data and model prediction for an incident pulse with an annealed copper pulse shaper
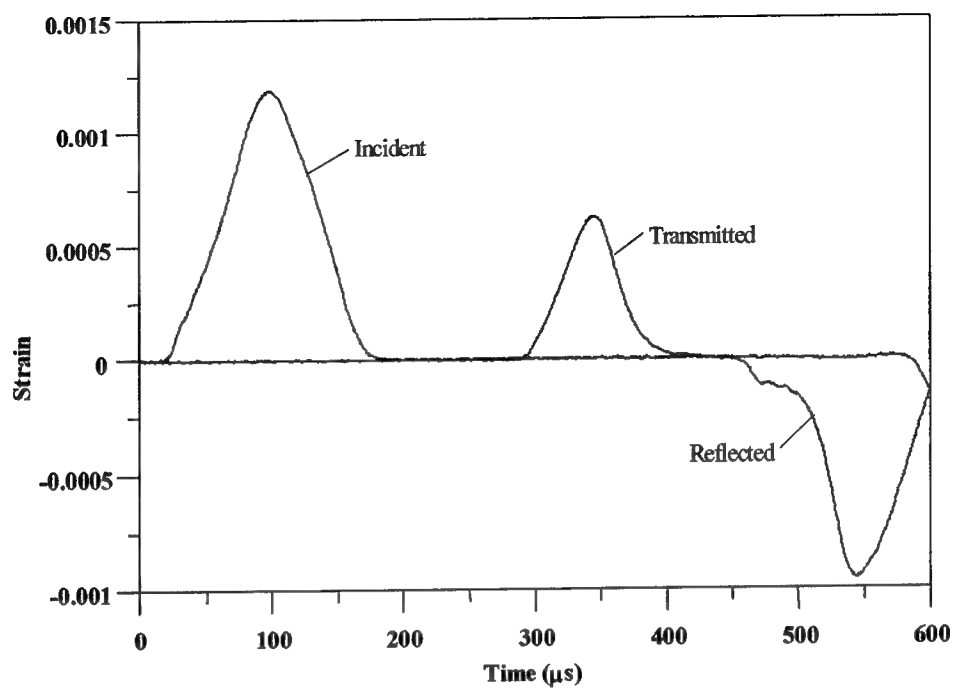
Figure 6.7 Strain-time signals for a pulse shaped SHPB experiment with a limestone sample
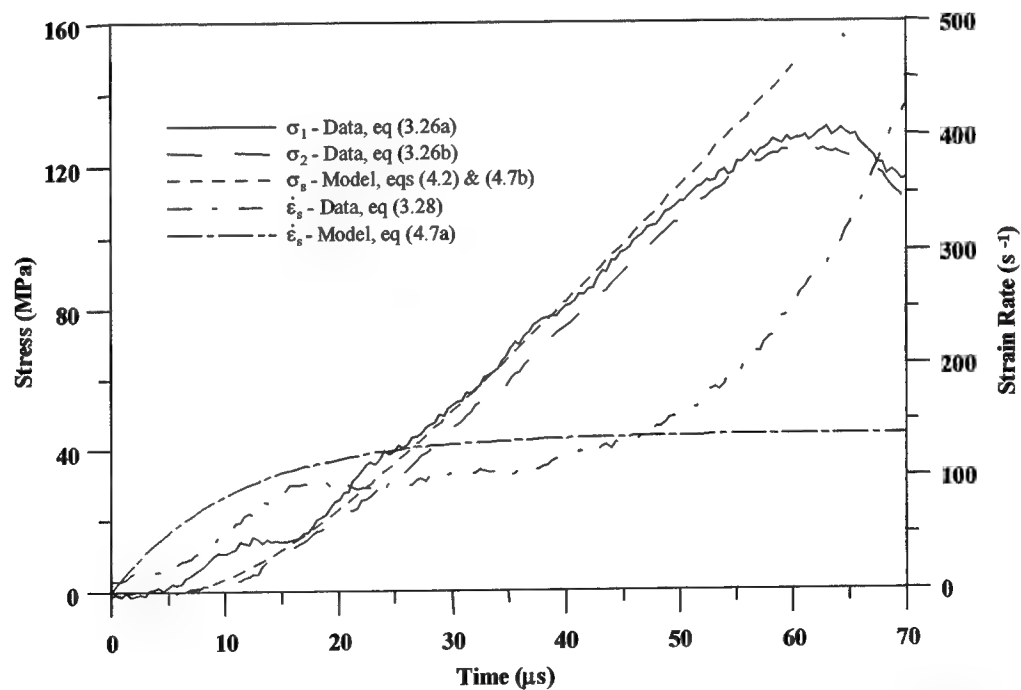
Figure 6.8 Interface stresses and strain rate from a pulse shaped SHPB experiment with a limestone sample

Figures 6.6 and 6.8 show that the limestone sample started to fail at about 50 µs and the incident ramp pulse was loading for about 75 µs. Therefore, the sample continued to be loaded after the start of failure and the sample eventually experienced catastrophic damage. To recover an intact limestone sample after a test, we conducted another experiment with a ramp pulse in the incident bar with a shorter duration than the pulse shown in Fig. 6.6. Figure 6.9 shows the measured incident stress pulse and a prediction from our pulse shaping model for a 51-mm-long, steel striker bar with a striking velocity of 13.9 m/s. Note that the incident stress pulse is nearly a linear ramp for about 50 µs and has a stress loading rate of about $M = 3.1$ MPa/µs. Thus the incident pulses shown in Figs. 6.6 and 6.9 are almost identical except for the loading durations of 75 µs and 50 µs, respectively. Results for the 50 µs ramp incident pulse are shown in Fig. 6.10 and are very similar to those presented in Fig. 6.8. However, the strain rate in Fig. 6.7 shows an exponential growth after about 50 µs, and the strain rate in Fig. 6.10 remains nearly constant. Thus the sample is loaded after failure began in the first experiment, and the loading ended at about the time the sample started to fail in the second experiment. In the first experiment the limestone sample eventually failed with catastrophic damage; whereas, in the second experiment the sample was recovered intact. From Figs. 6.8 and 6.10 we conclude that the limestone sample has a failure stress of about 120 MPa for a strain rate between 100 s^{-1} and 120 s^{-1}.
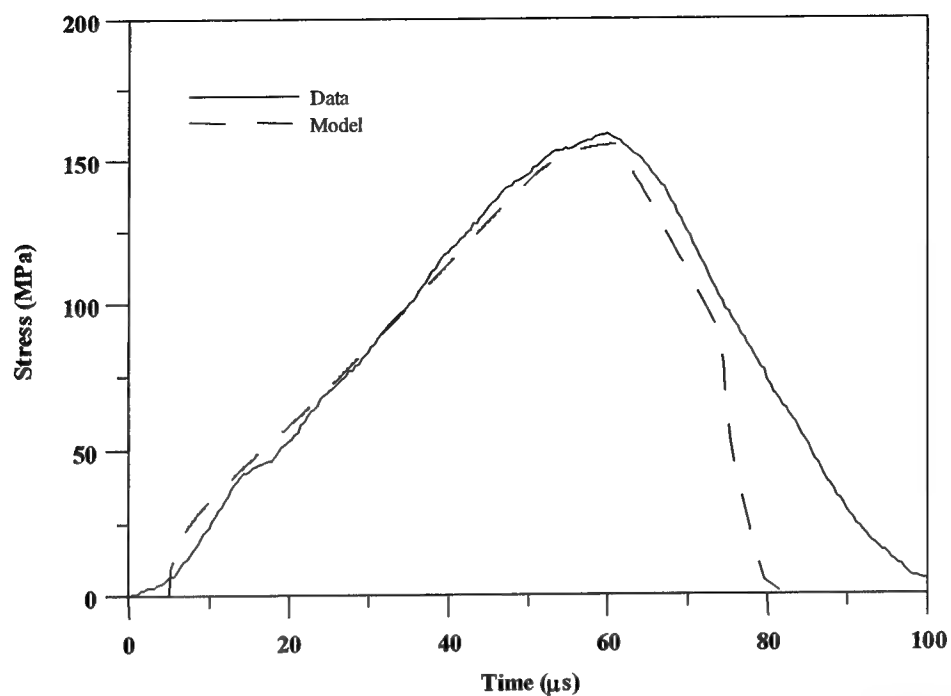
Figure 6.9 Data and model prediction for an incident pulse with an annealed copper pulse shaper
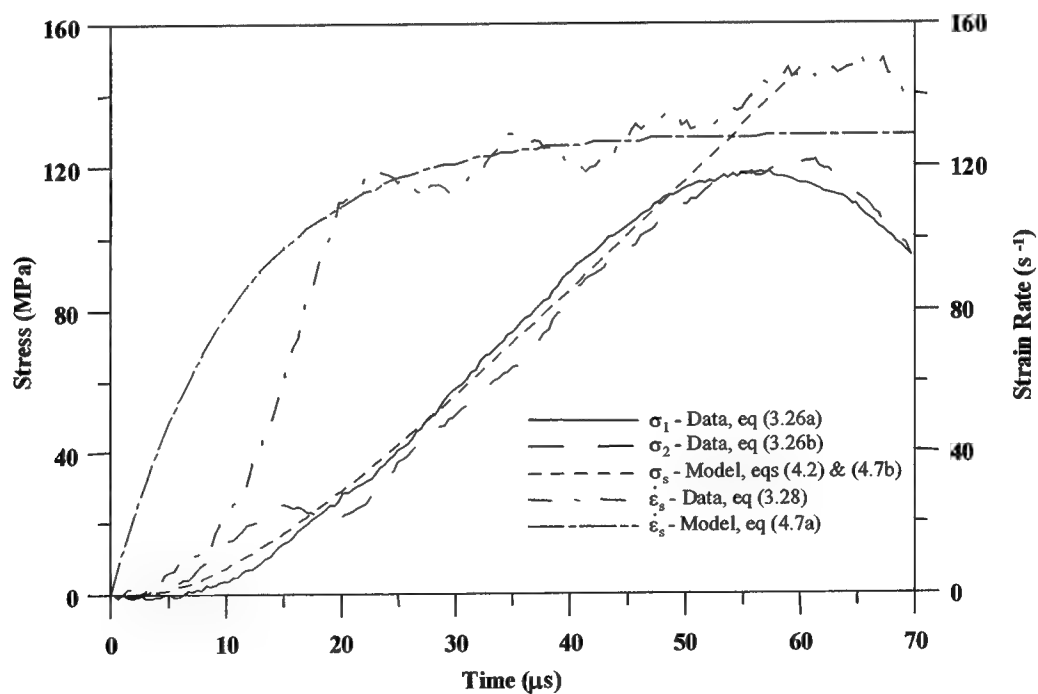
Figure 6.10 Interface stresses and strain rate from a pulse shaped SHPB experiment with a limestone sample

6.4   RESULTS

In Fig. 6.11, we show stress-strain curves from the dynamic SHPB experiments discussed in this section and a quasi-static stress-strain curve. We note that the failure stress at a strain rate between 100 and 120 s^{-1} is about double that obtained from a quasi-static experiment. Compressive strength versus strain rate data are presented in Fig. 6.12. In addition to the servo-hydraulic and SHPB data discussed in section 6.3, several additional compressive strength data points are included in Fig. 6.12. The open square symbols in Fig 6.12 represent data produced by Olsson and Mosher (1996) on 25.4-mm-diameter, $l_o/D =2$ limestone specimens. Also, two additional SHPB experiments with $l_o/D = 1.5$ specimens were conducted and show no noticeable strength effect from the different aspect ratios (open triangle and crossed circle). These additional data compare well with the previously discussed servo-hydraulic and SHPB data and create an almost linear compressive strength- log strain rate relationship over the range we tested.
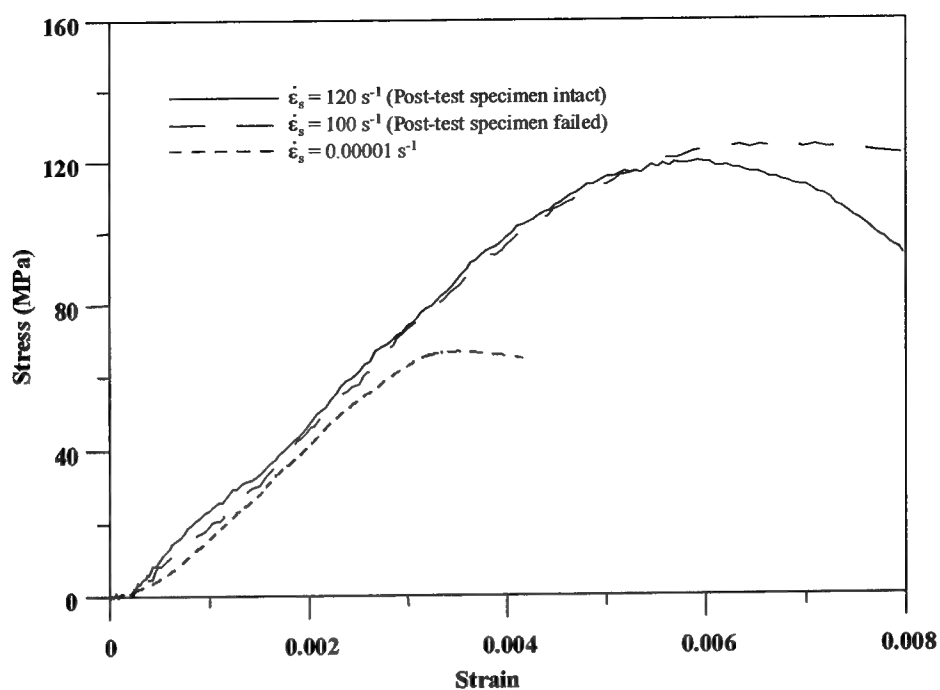
Figure 6.11 Quasi-static and dynamic stress-strain limestone data
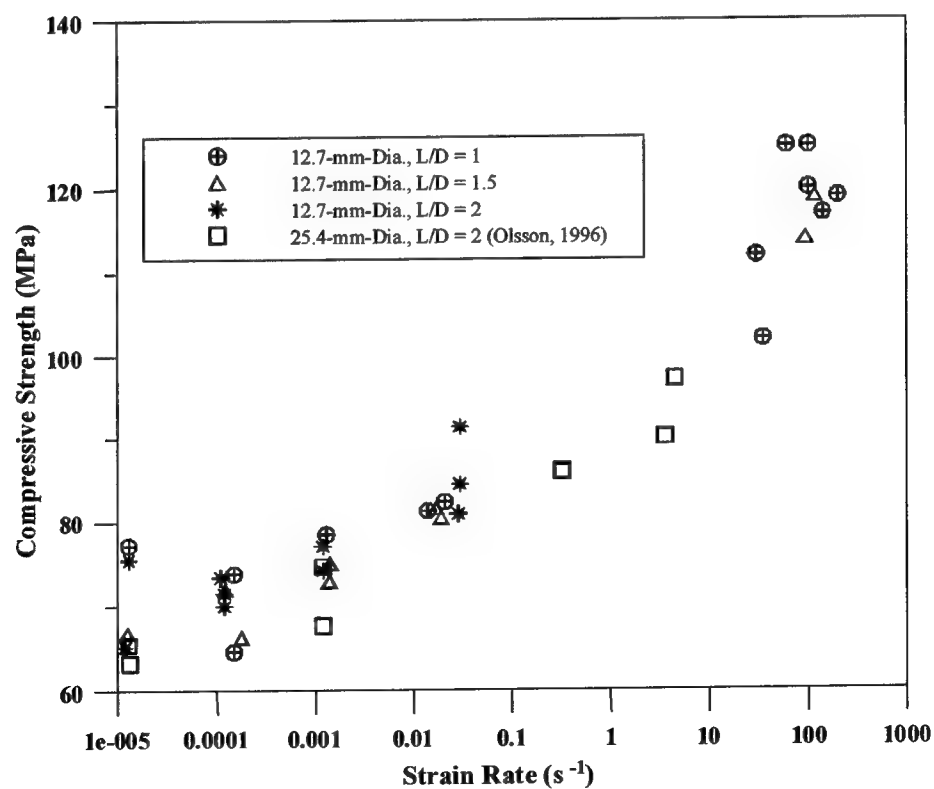
Figure 6.12 Unconfined compressive strength of an Indiana limestone versus strain rate

6.5   DISCUSSION OF STRAIN RATE EFFECTS IN INDIANA LIMESTONE

The results presented in Fig. 6.12 on Indiana limestone demonstrates that compressive strength increases with increasing strain rate. Previous research (Cheatham, 1968; Kumar, 1968; Sangha and Dhir, 1972; Green and Perkins ,1972; and Costin and Mecholsky, 1983) has also shown that the compressive strengths of many types of rocks are sensitive to strain rate.   Causes for this strain-rate effect have focused on environmental variables such as temperature (Rutter, 1972; and Podnieks, Chamberlain, and Thill, 1972) and liquid saturation (Colback, and Wiid, 1965; and Podnieks, Chamberlain, and Thill, 1972). In general, it has been shown that the strength of rocks and many other brittle solids (Lawn, 1993) will increase with increasing strain rate and decreasing temperature and saturation. In an attempt to gain an insight into the effect of strain rate on the strengths of rocks, the basic rock fracturing process is briefly reviewed, previous work is discussed, and possible explanations for the rate enhancement of Indiana limestone are presented.

Griffith (1920) assumed that defects, in the form of narrow cracks, created stress concentrations that weakened brittle materials. He proposed that fracture occurs when the stress at or near the crack tip exceeds the strength of the atomic bonds in this region. Using expressions for the stress field around an isolated crack in an elastic homogeneous body, Griffith developed a fracture initiation criterion for crack tip propagation. According to Griffith's model, a crack initiated in a tensile field will propagate unstably causing the specimen to fracture. However, the problem becomes more complicated in a

compressive field. Various investigators (Brace and Bombilakis, 1963; and Hoek and Bieniawski, 1965) have studied crack growth photoelastically in glass plates stressed in compression. They found that the initiation of crack growth under such conditions did not lead to failure. Instead, the cracks became stable after propagating some fraction of their initial length and in the direction of the maximum compressive principle stress.

If a uniform stress field is applied to an inhomogeneous material such as a rock, local stresses can be very different than those specified at the boundaries. The stress concentrations along grain boundaries, pores, and cracks further complicate this problem. As an inhomogeneous rock specimen is subjected to an increasing applied stress, there will be a certain region in the rock where the stress intensity will exceed the local strength. A crack, which may pre-exist in the material or at a grain boundary, will then propagate. When the crack propagates into a region where the local stress is lower, it will stop propagating and become arrested. As the applied stress is increased still higher, the region with the next highest stress concentration will fail, and so on, until combinations of these events produces a final fracture of the entire body.

The idealized picture of crack propagation in rocks is complicated by environmental effects. Rice (1978) modified the classical Griffith (1920) theory to account for stress corrosion in a solid due to an absorbate able to infiltrate the solid matrix and reduce the thermodynamic threshold by which crack growth can occur. Data by Boozer, Hiller, and Serdengecti (1962) on Indiana limestone (similar to the material of study in this research) and Navaho sandstone samples saturated with different liquids showed that triaxial compressive strengths of both rocks decreased as a function of increasing surface tension of the immersing liquids. Later, Colback and Wiid (1965)

presented similar results on unconfined compression experiments from another quartzitic sandstone. Conclusions from these experiments suggest that the absorbates decreased the energy needed to form the two new surfaces of a crack and thus decreased their strength, by a factor of two in some cases.

Other data from Krokosky and Husak (1968) showed unconfined strength increases of up to 50% from samples of basalt tested at room ($1x10^5$ Pa) pressure and when ultra-high vacuum pressures ($1.3x10^{-7}$ Pa) were applied. Results from these experiments indicate that the lack of a stress corrosion mechanism, namely water vapor, in the ultra-high vacuum tests was responsible for the increased strength of the rock.

In addition to environmental effects, the rate of loading is also an important parameter because it can limit the effective time environmental conditions have to decrease the surface free energy at crack tips in rocks. Costin and Mecholsky (1983) applied Rice's (1978) failure criterion to a wet Tennessee marble to study the effects stress corrosion has on strength with varying strain rate. Data and model predictions, presented in Fig. 6.13, show three distinct stages to the shape of the data and model prediction. At strain rates below about 10^{-6} s^{-1}, the model predicts that the rock strength will be independent of rate. In this strain-rate range, the stress around the advancing crack tips will have sufficient time to relax and the crack tips will have sufficient time to absorb moisture before the next increment of load is applied. At intermediate strain rates (10^{-6} to 1 s^{-1}), stress corrosion plays a less dominant role in the strength of the marble with increasing strain rate. As strain rates are increased, the medium around the advancing crack tips will not have sufficient time to absorb completely the water vapor that could weaken the atomic bonds at the crack tip. At strain rates above 1 s^{-1}, the

predicted failure stress of the marble is independent of stress corrosion because the water vapor will not have time to weaken the bonds of the advancing crack tip.   Model predictions and experimental data are shown to be in good agreement in Fig. 6.13.
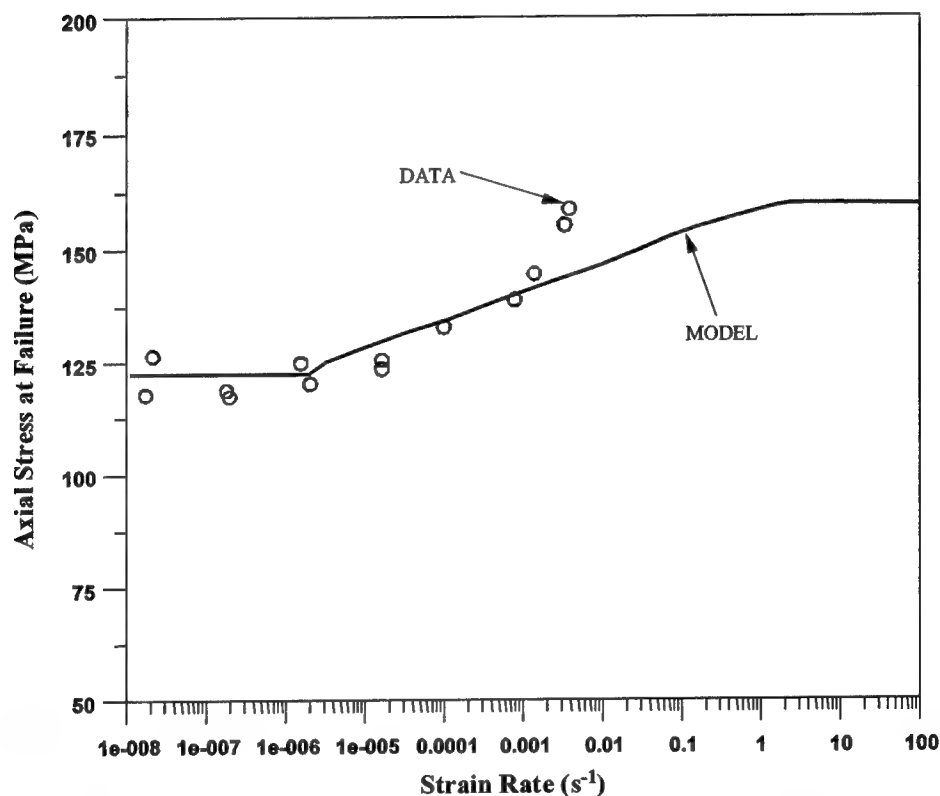
Figure 6.13 Ultimate failure stress versus strain rate from compression tests on wet Tennessee marble. [Costin and Mecholsky (1983)]

Griffith's (1920) and Rice's (1978) models assumes quasi-static loading of an ideal brittle material.   Under such idealized conditions, all of the mechanical energy absorbed by a material having linearly elastic behavior until failure is used to rupture the atomic bonds at the crack tip to form new surfaces. The rate of loading of this solid is slow enough so that stress fields within the medium can equilibrate, and no mechanical energy is used to generate heat, create plastic flow, or develop acoustic emissions around

an advancing crack tip. Although restrictive in nature, Rice's model shows that environmental effects in rocks can account for some of the strength enhancements shown in Fig. 6.12 for Indiana limestone, especially in the low to medium strain rate region.

At strain rates about 10^{-3} s^{-1}, other mechanisms such as non-equilibrated stress fields and mode of failure changes can also cause strength enhancements in rocks. Observations by Swanson (1984), and Atkinson (1984) have shown that the mode of crack propagation within rocks changes with strain rate. At moderate rates of strain (10^{-1} s^{-1}), the crack path tends to travel a more transgranular path compared to the predominant intergranular path seen at quasi-static strain rates (10^{-5} s^{-1}). As a rock specimen is subjected to a stress field in a quasi-static environment, crack advancement occurs at a slow enough rate to relax the stress concentrations adjacent to the crack surface before the next stress increment is applied. However, at faster strain rates, the stress concentrations do not have sufficient time to fully equilibrate through the medium and cause the stress distribution around a crack tip to be a function of strain rate. In this case, the magnitude of the stress concentrations around a crack tip is higher. Depending upon the mineralogy and pore and flaw distributions of the rock being tested, the crack path could follow a much more transgranular path at the higher strain rates (Swanson, 1984). It is likely that the observed strength enhancements we have seen for Indiana limestone as a function of strain rate are due to one or more of the mechanisms we have discussed above.

To begin to unravel the dependence saturation level, equilibrium, and mode of failure changes have on the unconfined compressive strength of Indiana limestone would require an extensive experimental effort. Although standard American Society for

Testing & Materials (ASTM) practices (D4543, 1991, and D2664, 1991) exist for preparing and testing rock materials in a quasi-static environment, no standards are currently available for the dynamic testing of rocks. Further, Podnieks, Chamberlain, and Thill, (1972) have shown that slight variations of sample preparation and preconditioning can dramatically effect strength characteristics of rocks. Repetitive experiments would need to be conducted at several strain-rate ranges to obtain statistically meaningful results.

We have shown that recovery of damaged specimens loaded with a single, well-defined loading pulse from a SHPB experiment is possible. Several different post-mordem analyses of the recovered samples could be performed in future work to help quantify the damage created in the limestone tested at various rates of strain. Some examples are: 1) Pre- and post-test sonic velocities can be measured, 2) reloading of recovered intact samples from SHPB experiments could be performed quasi-statically to measure the relative change in unconfined strengths of pristine and dynamically tested limestone samples, and 3) optical or scanning electron microscope images of sections of samples could be used to study fracture patterns and trends.

CHAPTER 7

COMPRESSIVE BEHAVIOR OF MACOR

The analytical models presented in Chapter 4 examine the sample response produced by an incident stress pulse. The incident stress pulse given by eq (4.1) is taken as a quadratic function, but these models assume the sample has a linear stress-strain response. While most brittle materials, such as rocks or ceramics, have quasi-linear, dynamic stress-strain responses, slight deviations from linear can change the strain-rate histories over the test duration. Because we do not know the sample, stress-strain response before a test, some experimental trials are required before we achieve dynamic stress equilibrium and nearly constant strain rate. The analytical models show trends that help guide and minimize our experimental trials.

We begin this process by first conducting a few quasi-static, stress-strain experiments with a new sample material. Then, we linearize this quasi-static data and obtain a value for E_s for eq (4.2). Our early SHPB experiments are conducted with nearly linear incident stress pulses such as those for limestone (Fig. 6.6) or the incident pulse shown in Fig. 5.7. We check for sample equilibrium and nearly constant strain rate with strain measurements and eqs (3.26a), (3.26b), and (3.28). In this study, we learned that it was relatively easy to obtain sample equilibrium and more difficult to obtain a nearly constant strain rate over most of the test duration. For the Macor results presented in this section, analytical and experimental trials suggest the concave downward incident stress pulse shown in Fig. 7.1 produced a nearly constant strain rate.

To demonstrate our modified SHPB technique, we present results from two pulse shaped experiments with the machineable glass ceramic, Macor (Corning, 1992). Macor is a white, ceramic composite comprised of a fluorophlogopite mica phase (55%) interspersed in a borosilicate glass matrix (45%) having a density ρ_s = 2520 kg/m^3, Young's modulus E_s = 64.1 GPa, bar wave velocity c_s = 5040 m/s, and porosity η = 0%. Data from experiments with Macor show that the samples are in dynamic stress equilibrium and have nearly constant strain rates over most of the duration of the tests. In addition, we carefully bracket sample failure with one test where the sample fails with catastrophic damage and a second test where the sample is recovered intact. Thus, intact samples that experience strains beyond the elastic region and post-peak stresses can be retrieved for microstructural evaluations.

The striker, incident, and transmission bars shown in Fig. 3.4 were made from high strength, maraging VM 350 steel (Vasco Pacific, Montebello, CA) and have density ρ = 8100 kg/m^3, Young's modulus E = 200 GPa, and bar wave velocity c = 4970 m/s. The incident and transmission bars had diameters of 19.05 mm and lengths of 2130 and 915 mm, respectively. Strain gages shown in Fig. 3.4 were located at 1065 mm from the impact surface of the incident bar and at 458 mm from the sample/ bar interface on the transmission bar. The Macor samples had a length and diameter of 9.53 mm. To obtain incident stress pulses that would strain the Macor samples at a nearly constant strain rate over most of the test durations, 10.21-mm-diameter, 0.79-mm-thick, annealed C11000 copper pulse shapers were used. All of the above mentioned parameters remained fixed for the two experiments presented in this section. However, the first experiment used a 19.05-mm-diameter, 127-mm-long, striker bar, and the second experiment used a

19.05-mm-diameter, 101.6-mm-long, striker bar. The effective densities and wave velocities that correct for the added mass of the sabots were $\rho_{st} = 8790$ kg/m^3, $c_{st} = 4770$ m/s and $\rho_{st} = 8760$ kg/m^3, $c_{st} = 4780$ m/s for the 125-mm-long and 101.6-mm-long striker bars, respectively. Both striker bars were launched to a striking velocity of 12.2 m/s.
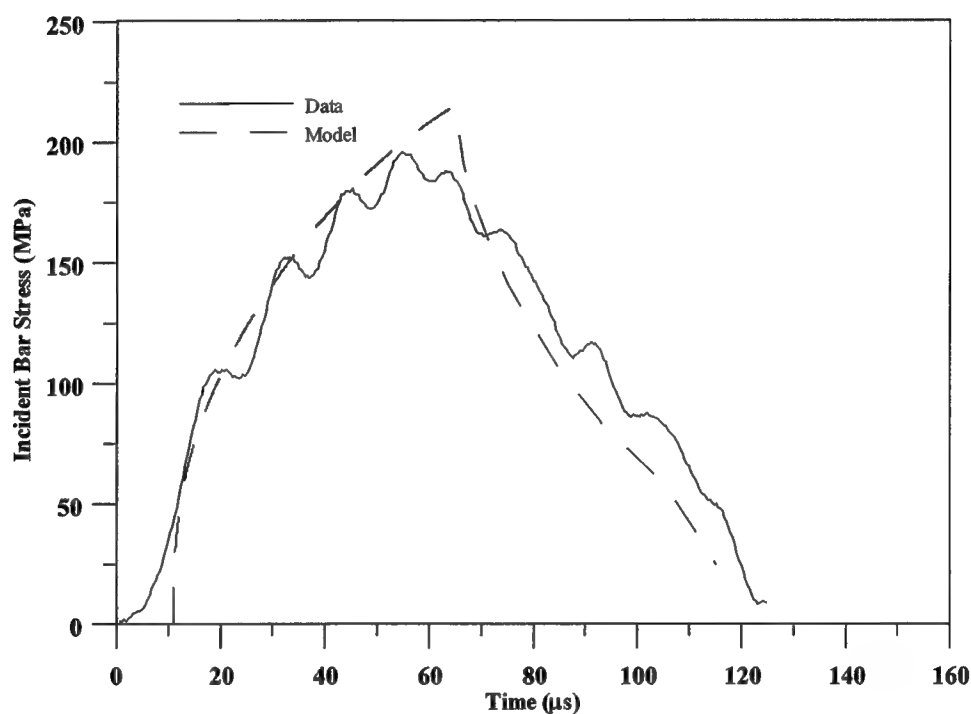
Figure 7.1 Incident bar stress data and model prediction for an annealed C11000 copper pulse shaper

Figures 7.1, 7.2, and 7.3 show data for the experiment conducted with the 127-mm-long striker bar. In Fig. 7.1, we show the measured incident stress pulse and a prediction from our pulse shaping model. Figure 7.2 shows stresses at stations 1 and 2 shown in Fig. 3.4. The stress at the incident bar/ sample interface σ_1 is calculated from eq (3.29a) and strains measured on the incident bar, and stress at the transmission

bar/sample interface σ_2 is calculated from eq (3.29b) and the measured transmitted strain. These interface stresses are in reasonably good agreement, which implies that the sample is nearly in dynamic stress equilibrium. Strain rate in the sample, shown in Fig. 7.3, is calculated from eq (3.31) and the measured reflected strain in the incident bar. The average strain rate is about 300 s^{-1} over 20 μs to 60 μs. At about 60 μs the sample begins to fail and eventually fails with catastrophic damage.
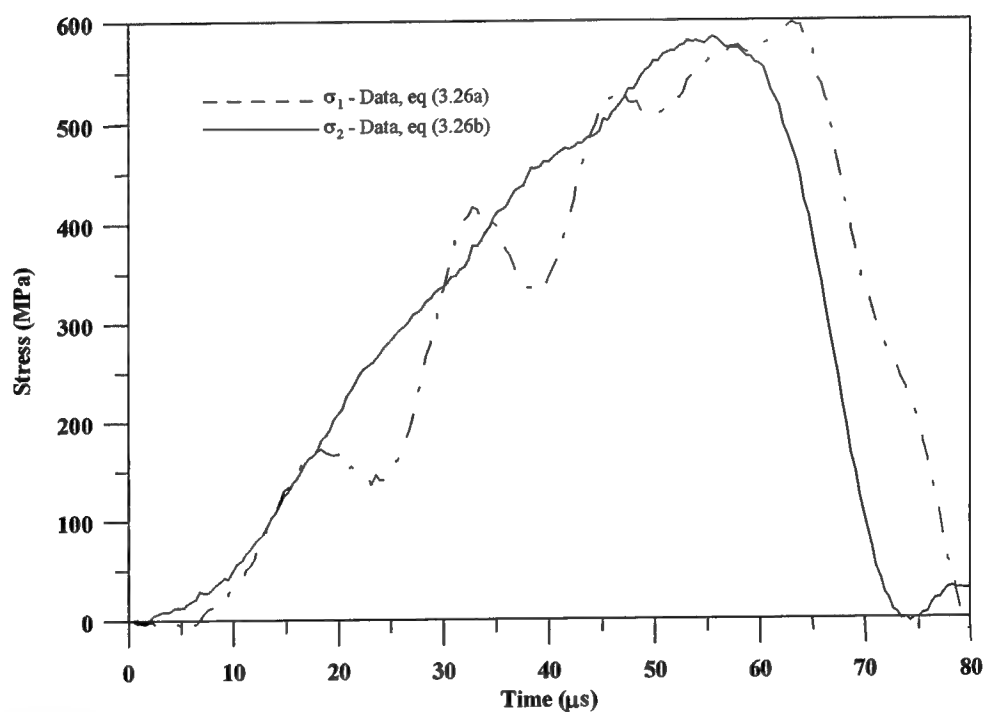
Figure 7.2 Interface stresses from a pulse shaped SHPB experiment with a Macor sample
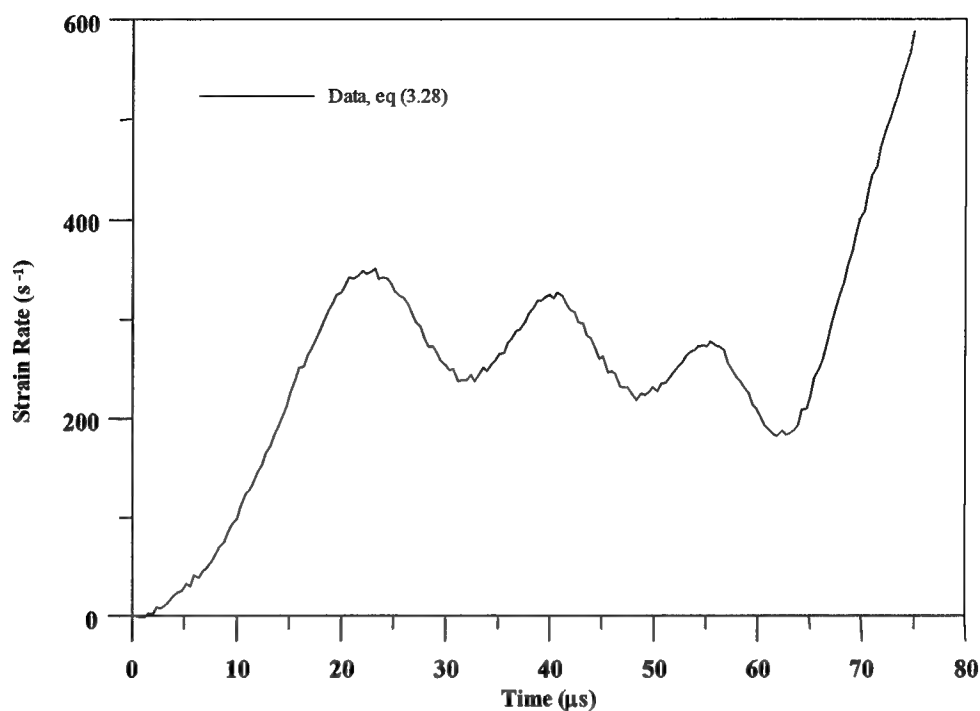
Figure 7.3 Strain rate from a pulse shaped SHPB experiment with a Macor sample

Figures 7.4, 7.5, and 7.6 show data for the experiment conducted with the 101.6-mm-long striker bar. Figure 7.6 shows an average strain rate of 280 s^{-1} over 20 μs to 50 μs. At 50 μs, the sample unloads and was recovered intact.

Figure 7.7 shows dynamic and quasi-static stress-strain data for the Macor samples. The sample with an average strain rate of $\dot{\varepsilon}_s$ = 280 s^{-1} experienced strain beyond the elastic region and post-peak stress. Samples such as these can be retrieved for post-test, microstructural evaluations.
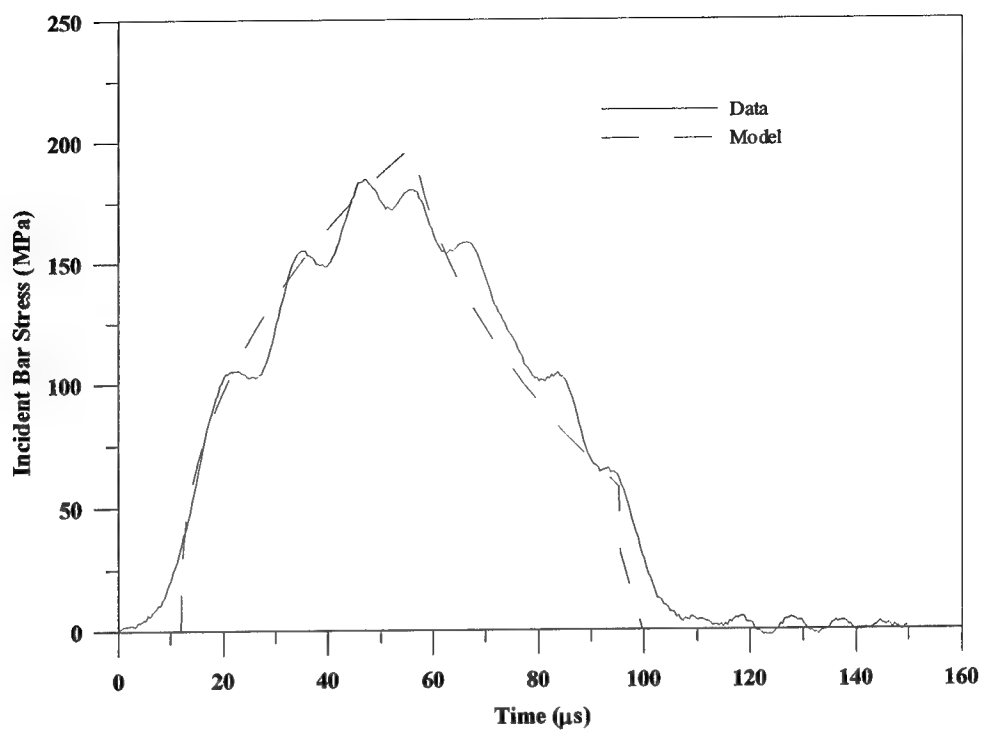
Figure 7.4 Incident bar stress data and model prediction for an annealed C11000 copper pulse shaper
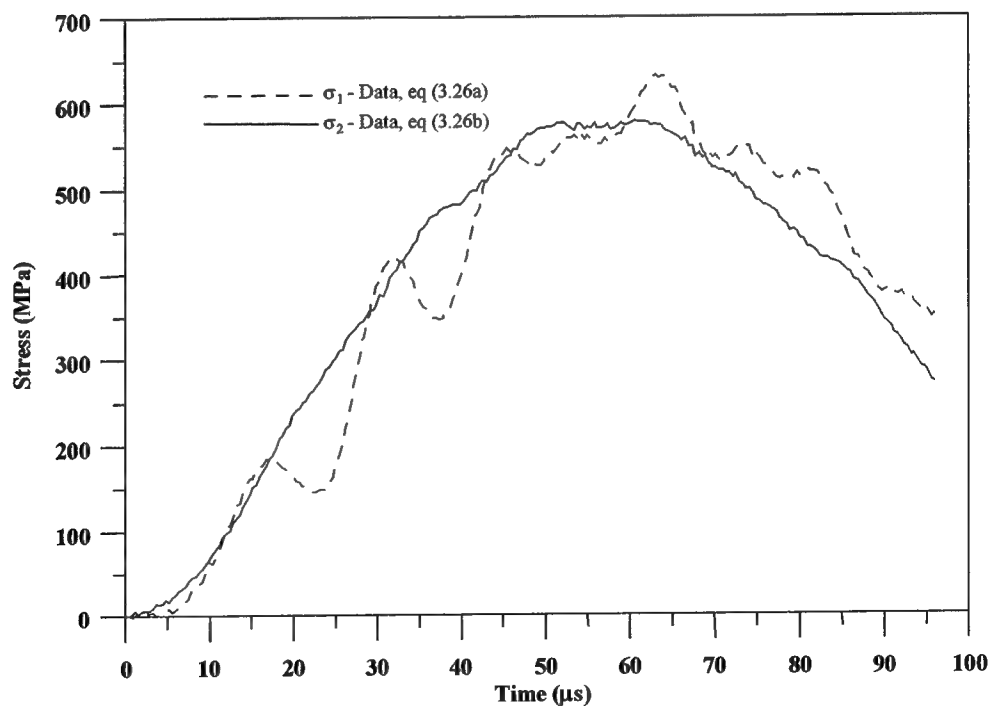
Figure 7.5 Interface stresses from a pulse shaped SHPB experiment with a Macor sample
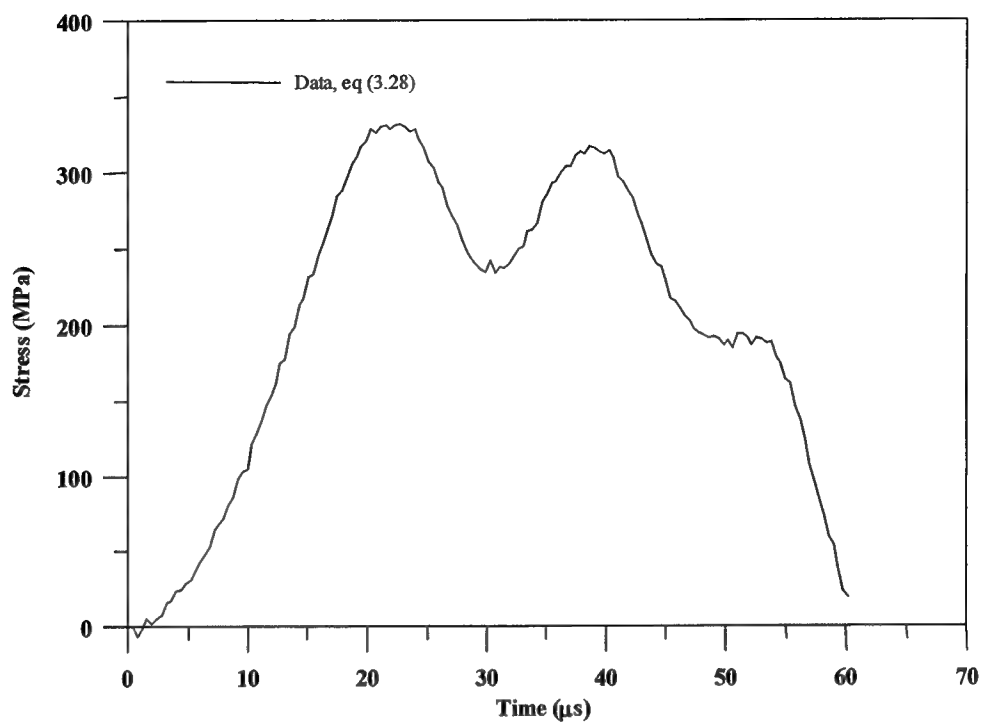
Figure 7.6 Strain rate from a pulse shaped SHPB experiment with a Macor sample
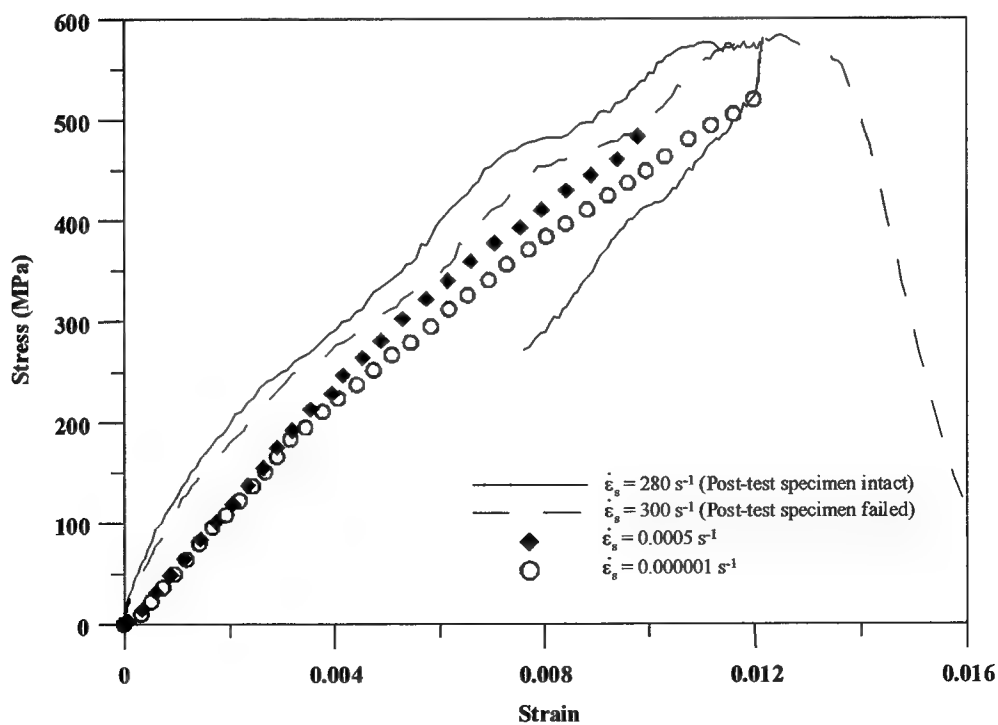
Figure 7.7 Quasi-static and dynamic stress-strain data for Macor

CHAPTER 8

CONCLUSIONS

A series of penetration experiments were conducted into Indiana limestone targets with three scales of geometrically similar projectiles. The ogive-nose rod projectiles with a length-to-diameter ratio of ten had diameters and masses of 7.1 mm, 0.020kg; 12.7 mm, 0.117 kg; and 25.4 mm, 0.931 kg. Based on data sets with these three projectile scales, a previously developed analytic penetration model was used to describe the target resistance by its density and a target strength parameter that is determined from penetration depth versus striking velocity data. Results from these experiments and the penetration model suggested a strain-rate dependence of the limestone target material.

In order to begin to investigate the strain-rate effects of Indiana limestone, a split Hopkinson pressure bar (SHPB) facility was designed and built for dynamic testing of brittle materials in uniaxial compression. Preliminary results from conventional SHPB experiments on limestone samples indicated that critical experimental modifications had to be made to the traditional SHPB apparatus for valid testing of brittle materials. Specifically, the incident pulse was shaped such that the samples reached dynamic stress equilibrium and had a nearly constant strain rate throughout most of the test duration. Also, the responses of the SHPB apparatus and the sample under test were modeled in order to guide the experimental designs and minimize the experimental trials.

The shaping of the incident pulse was accomplished by placing a thin disk of annealed or hard C11000 copper on the impact surface of the incident bar. After impact

by the striker bar, the copper disk deforms plastically and spreads the pulse in the incident bar. An analytical model and data were presented that show a wide variety of incident strain pulses can be produced by varying the geometry of the copper disks and the length and striking velocity of the striker bar. Model predictions were shown to be in good agreement with measurements.

Analytic models predicted that a ramp stress pulse in the incident bar is required for limestone samples. Data from experiments with limestone samples showed that the samples were in dynamic stress equilibrium and had constant strain rates over most of the test durations. Compressive strength stress data for strain rates between 10^{-5} and 300 s^{-1} on Indiana limestone samples showed an increase in compressive strength as strain rate increased. In addition, the ramp pulse durations were controlled such that samples were unloaded just prior to failure. Thus, intact samples that experienced strains beyond the elastic region and post-peak stresses could be retrieved for microstructural evaluations. To show the versatility of this work, experiments and model results were also presented for a machineable glass ceramic.

Thus, this thesis presents analytic models and experimental techniques that provide procedures to obtain dynamic, unconfined compressive, stress-strain data for brittle materials. Data for limestone and a glass ceramic materials were presented to demonstrate these procedures.

REFERENCES

Ahrens, T. J. and Rubin, A. M. (1993). Impact-induced tensional failure in rock, *J. Geophys. Res.* **98**, 1185–1203.

Aidun, J. B. and Gupta, Y. M. (1995). Shear and compression waves in shocked calcium carbonate, *J. Geophys. Res.* **100**, 1955–1980.

Anderson, C. E. and Bodner, S. R. (1988). Ballistic impact: the status of analytical and numerical modeling, *Int. J. Impact Engng.* **7**, 9–35.

Atkinson, B. K. (1984). Subcritical crack growth in geologic materials, *J. Geophys. Res.* **89**, 4077-4114.

Backman, M. E. and Goldsmith, W. (1978). The mechanics of penetration of projectiles into targets, *Int. J. Eng. Sci.* **16**, 1–99.

Baron, H. G. (1956). Stress/strain curves for some metals and alloys at low temperatures and high rates of strain. *J. Iron St. Inst.* **182**, 354-365.

Boozer, G. D., Hiller, K. H., and Serdengetti, S. (1962). Effects of pore fluids on the deformation behavior of rocks subjected to triaxial compression. *Proc. 5th U. S. Symposium on Rock Mechanics*, University of Minnesota, May.

Brace, W. F. and Bombolakis, E. G. (1963). A note on brittle crack growth in compression. *J. Geophys. Res.* **68**, 3709-3713.

Brown, W. F., Mindlin, H., and Ho, C. Y. (1996). *Aerospace Structural Metals Handbook*, Vol. 1, Code 1206, CINDAS/USAF CRDA Handbooks Operation, Purdue University, West Lafayette, IN 47907-1293.

Camacho, G. T. and Ortiz, M. (1997), Adaptive lagrangian modelling of ballistic penetration of metallic targets, *Comput. Methods Appl. Engng.* **142**, 269–301.

Cheatham, J. B. (1968). The effect of pressure, temperature, and loading rate on the mechanical properties of rocks. In *Mechanical Behavior of Materials Under Dynamic Loads*, 388-401.

Chen, W. and Ravichandran, G. (1997). Dynamic compressive failure of a glass ceramic under lateral confinement. *J. Mech. Phys. Solids* **45**, 1303-1328.

Chen, W., Zhang, B., and Forrestal, M. J. (1999). A split Hopkinson bar technique for low-impedance materials. *Exper. Mech.* **39**, 81-85.

Christensen, R. J., Swanson, S. R., and Brown, W. S. (1972). Split-Hopkinson-bar tests on rock under confining pressure. *Exper. Mech.* **29**, 508-513.

Colback, P. S. B. and Wiid, B. L. (1965). The influence of moisture content on the compressive strength of rocks. *Proc. 3rd Canadian Symposium on Rock Mechanics*, University of Toronto, Canada, January, 65-83.

Corbett, G. G., Reid, S. R., and Johnson, W. (1996). Impact loading of plates and shells by free-flying projectiles: a review, *Int. J. Impact Engng.* **18**, 141–230.

Corning Incorporated, (1992). Macor machineable glass ceramic: safety and health issues. Technical Bulletin, Macor-03, Corning, New York.

Costin, L. S. and Mecholsky, J. J. (1983*). Proc. 24th U.S. Symposium on Rock Mechanics*, Texas A&M University, College Station, Texas, 385-394.

Dahl, J. (1991). Aer Met 100 – an advanced steel for the aerospace industry. *Advanced Materials Technology International*, pp. 40–45.

Davies, E. D. H. and Hunter S. C. (1963). The dynamic compression testing of solids by the method of the split hopkinson pressure bar. *J. Mech. Phys. Solids* **11**, 155-179.

Duffy, J., Campbell, J. D., and Hawley, R. H. (1971). On the use of a torsional split Hopkinson bar to study rate effects in 1100-0 aluminum. *J. Appl. Mech.* **37**, 83-91.

Farmer, I. (1983). *Engineering Behavior of Rocks*, 2nd edition. Chapman and Hall, New York.

Follansbee, P. S. (1985). The Hopkinson bar. In *Mechanical Testing, Metals Handbook*, Vol. 8, 9th edition, American Society for Metals, Metals Park, Ohio, 198-217.

Forrestal, M. J., Altman, B. S., Cargile, J. D., and Hanchak, S. J. (1994). An empirical equation for penetration depth of ogive-nose projectiles into concrete targets, *Int. J. Impact Engng.* **15**, 395–405.

Forrestal, M. J., Frew, D. J., Hanchak, S. J., and Brar, N. S. (1996). Penetration of grout and concrete targets with ogive-nose steel projectiles, *Int. J. Impact Engng.* **18**, 465–476.

Fossum, A. F., Senseny, P. E., Pfeifle, T. W., and Mellegard, K. D. (1995). Experimental determination of probability distributions for parameters of a Salem limestone cap plasticity model. *Mech. Mater.* **21**, 119-137.

Frew, D. J., Forrestal, M.J., and Chen, W. (2001). A split Hopkinson bar technique to determine compressive stress-strain data for rock materials. *Exper. Mech.*, **41**, 40-46.

Frew, D. J., Hanchak, S. J., Green, M. L., and Forrestal, M. J. (1998). Penetration of concrete targets with ogive-nose steel rods, *Int. J. Impact Engng.* **21**, 489–497.

Grady, D. E. and Hollenbach, R. E. (1979). Dynamic fracture strength of rock, *Geophysical Research Letters*, **6**, No. 2, pp. 73–76.

Graff, K. F. (1975). *Wave Motions in Elastic Solids*. Dover Publications, New York.

Gray, G. T. (1999). Classic split-Hopkinson pressure bar technique, LA-UR-99-2347, Los Alamos National Laboratory, Los Alamos, NM 87545, To be published in ASM Volume 8, Chapter 6A- Mechanical Testing, ASM International, Materials Park, OH, 44073.

Gray, G. T. and Blumenthal, W. R. (1999). Split-Hopkinson pressure bar testing of soft materials, LA-UR-99-4878, Los Alamos National Laboratory, Los Alamos, NM 87545, To be published in ASM Volume 8, Chapter 6E- Mechanical Testing, ASM International, Materials Park, OH, 44073.

Green, S. J. and Perkins, R. D. (1972). Uniaxial compression tests at varying strain rates on three geologic materials. In *Basic and Applied Mechanics – Proc. 10th U. S. Symposium on Rock Mechanics*. Edited Gray, K. E., 35-54.

Griffith, A. A. (1920). The phenomena of rupture and flow in solids. *Phil. Trans. Roy. Soc. Lond.* **A221**, 163-198.

Hawkes, I. and Mellor, M. (1970). Uniaxial testing in rock mechanics laboratories. *Eng. Geol.*, **4**, 177-285.

Hoek, E. and Bieniawski, Z. T. (1965). Brittle fracture propagation in compression. *Int. J. Fracture* **1**, 137-155.

Hohler, V. and Stilp, A. J. (1990). Long-rod penetration mechanics, *High Velocity Impact Dynamics*, Chapter 5, J. A. Zukas (Ed.), John Wiley and Sons, Inc., New York, N.Y.

Jaeger, J.C. and Cook, N. G. W. (1979). *Fundamental of Rock Mechanics*, 3rd edition, Chapman and Hall, New York.

Kolsky, H. (1949). An investigation of the mechanical properties of materials at very high rates of loading. *Proc. Royal Soc. B* **62**, 676-700.

Kolsky, H. (1963). *Stress Waves in Solids*. Dover Publications, New York.

Krokosky, E. M. and Husak, A. (1968). Strength characteristics of basalt rock in ultra-high vacuum. *J. Geophys. Res.* **73**, 2237-2247.

Kumar, A. (1968). The effect of stress rate and temperature on the strength of basalt and granite. *Geophysics* **33**, 501-510.

Larson, D. B. and Anderson, G. D. (1979). Plane shock wave study of porous geologic media. *J. Geophys. Res.* **84**, 4592-4600.

Lawn, B. (1993). *Fracture of Brittle Solids*, 2nd edition, Cambridge University Press, Cambridge.

Lewis, C. F. (1979). Properties and selection: nonferrrous alloys and pure metals, *Metals Handbook*, 9th Edition, *2*, American Society for Metals, Metals Park, OH.

Lindholm, U. S. (1964). Some experiments with the Split Hopkinson Pressure Bar. *J. Mech. Phys. Solids* **12**, 317-335.

Lindholm, U.S., Yeakley, L.M., and Nagy, A. (1974). The dynamic strength and fracture properties of Dresser basalt. *Int. J. Rock Mech. Min. Sci. & Geomech. Abstr.* **11**, 181-191.

Lipkin, J., Grady, D. E., and Campbell, J. D. (1977). Dynamic flow and fracture of rock in pure shear. *Proc. 18th U.S. Symposium on Rock Mechanics*. Colorado School of Mines press. Edited Wang, F. and Clark, G. B., 3B21-3B27.

Mastilovic, S. and Krajcinovic, D. (1999). Penetration of rigid projectiles through quasi-brittle materials. *J. Appl. Mech.* **66**, 585-592.

Nemat-Nasser, S., Isaacs, J. B., and Starrett, J. E. (1991). Hopkinson techniques for dynamic recovery experiments. *Proc. R. Soc. Lond.* **A435**, 371-391.

Nicholas, T. (1982). "Material behavior at high strain rates", *Impact Dynamics*, Chapter 8, J. A. Zukas et. al. (Ed.), John Wiley and Sons, New York.

Olsson, B. and Mosher, D., (1996). Unpublished notes sent to M. J. Forrestal, Sandia National Laboraories, Albuquerque, NM., November.

Ortiz, M. (1996). Computational micromechanics, *Comp. Mech.* **18**, pp. 321–338.

Pettijohn, E. R. (1975). *Sedimentary Rocks*, 3rd edition. Harper and Row, New York.

Piekutowski, A. J., Forrestal, M. J., Poormon, K. L., and Warren, T. L. (1999). Penetration of 6061-T6511 aluminum targets by ogive-nose steel projectiles with striking velocities between 0.5 and 3.0 km/s, *Int. J. Impact Engng.* **23**, 723-734.

Podnieks, E. R., Chamberlain, P. G., and Thill, R.E. (1972). Enviornmental effects on rock properties. In *Proc. 10th U. S. Symposium on Rock Mechanics.* American Institute of Mechanical Engineers, New York, 215-241.

Preparing rock core specimens and determining dimensional and shape tolerances (1991). *D 4543 Annual Book of ASTM Standards*, ASTM, Philadelphia, 687-690.

Ramesh, K. T. and Narasimhan, S. (1996). Finite deformations and the dynamic measurement of radial strains in compression Kolsky bar experiments. *Int. J. Solids Structures* **33**, 3723-3738.

Ravichandran, G. and Subhash, G. (1994). Critical appraisal of limiting strain rates for compression testing of ceramics in a split Hopkinson pressure bar. *J. Am. Ceram. Soc.* **77**, 263-267.

Recht, R. (1990). High velocity impact dynamics: analytical modeling of plate penetration dynamics, *High Velocity Impact Dynamics*, Chapter 7, J. A. Zukas (Ed.), John Wiley and Sons, Inc., New York, N.Y.

Rice, J. R. (1978). Thermodynamics of the quasi-static growth of Griffith cracks. *J. Mech. Phys. Solids* **26**, 61-78.

Rogers, W. P. and Nemat-Nasser, S. (1990). Transformation plasticity at high strain rate in magnesia-partially-stabilized zirconia. *J. Am. Ceram. Soc.* **73**, 136-139.

Rutter, E. H. (1972). The effects of strain-rate changes on the strength and ductility of Solenhofen limestone at low temperatures and confining pressures. *Int. J. Rock Mech. Min. Sci.* **9**, 183-189.

Sangha, C. M. and Dhir, R. K. (1972). *Int. J. Rock Min. Sci. Geomech. Abstr.* **9**, 343-354.

Swanson, P. L. (1984). Subcritical crack growth and other time- and environment-dependent behavior in crustal rocks. *J. Geophys. Res.* **89**, 4137-4152.

Togami, T. C., Baker, W. E., and Forrestal, M. J. (1996). A split Hopkinson bar technique to evaluate the performance of accelerometers. *J. Appl. Mech.* **63**, 353-356.

Triaxial compressive strength of undrained rock core specimens without pore pressure measurements (1991). *D 2664 Annual Book of ASTM Standards*, ASTM, Philadelphia, 231-233.

Vasco-Pacific (1998). Mechanical specification sheet for Vasco-Max C-350 maraging steel, Montebello, CA, 16-19.

Warren, T. L. and Forrestal, M. J. (1998). Effects of strain hardening and strain-rate

    sensitivity on the penetration of aluminum targets with spherical-nosed rods. *Int. J.*

    Solids Struct. **35**, 3737-3753.

Wu, X. J. and Gorham, D. A. (1997). Stress equilibrium in the split Hopkinson pressure

    bar test. *J. PHYS. IV FRANCE* **7**, C3, 91-96.

Yadav, S., Chichili, D. R., and Ramesh, K. T. (1995). The mechanical response of a

    6061-T6 Al/Al2O3 metal matrix composite at high rates of deformation. *Acta metall.*

    Mater. **43**, 4453-4464.

APPENDIX A

PULSE SHAPING FORTRAN CODE

```
$DEBUG

C
C                 HOPKINSON BAR PULSE SHAPING PROGRAM HOP9-1 (9/20/99)
C
C          THIS PROGRAM CALCULATES THE INCIDENT STRESS IN THE SPLIT
C          HOPKINSON BAR FOR A PULSE SHAPING MATERIAL WITH KNOWN MATERIAL
C          PROPERTIES.
C
           PARAMETER        (NPS=15000)
           DOUBLE PRECISION HM(NPS),HI(NPS),EC(NPS),T(NPS),DELT(NPS)
           DOUBLE PRECISION STRAINI(NPS),STRESSI(NPS),TMS(NPS)
           DOUBLE PRECISION STRNRT(NPS),V1(NPS),V2(NPS),AM
           DOUBLE PRECISION DHM,DDELT,DT,DEC,SIGCSTR,ECSTR,VALUE1,VALUE4
C
C          CA110 COPPER MODEL
C
C          SIGO=550000000.
C          AN=0.0875
C          AM=4.
C
C          CA110 'ANNEALED' COPPER MODEL REGULAR
C
C          SIGO=625000000.
C          AN=0.32
C          AM=4.25
C
C          CA110 'ANNEALED' COPPER MODEL THIN
C
           SIGO=750000000.
           AN=0.37
           AM=4.25
C
C          NEMAT-NASSER'S CONSTANTS (CA 101)
C
C          SIGO=570000000.
C          AN=0.2
C          AM=9.9e25
C
C          COPPER PARAMETERS
C
           YOUNGC=117.21E03
           HOIN=0.0317
           HOM=HOIN*0.0254
           DIAO=0.402
           AO=DIAO**2*0.7854
           HSTEPI=0.00005*0.0254
           STEP=50
C
C          BAR PROPERTIES  (C-350)
C
           E=200E9
           RHO=8100
           C=4969
           A=0.7465**2*0.7854
C
C          BAR PROPERTIES (ALUMINUM)
C
C          E=72.0e9
C          RHO=2780
C          C=5089
C          A=0.750**2*0.7854
C
C          STRIKER PARAMETERS
C
           RHOST=RHO*1.0885
           CST=SQRT(E/RHOST)
           VO=12.28
           ALEN=6.
```

```
         ST=2*ALEN*0.0254/CST
C
C        INCREMENTS
C
         STAR1=HSTEPI/200
         STAR2=HSTEPI/10000
         STAR3=HSTEPI/52500
         STAR4=HSTEPI/25000
         AK1=(2*SIGO*AO)/(RHOST*CST*VO*A)
         AK=(SIGO*AO)/(VO*A)*(1/(C*RHO)+1/(CST*RHOST))
C
C        INITIAL VALUES
C
         HM(1)=HOM
         HI(1)=HOM/0.0254
         EC(1)=0
         T(1)=0
         DELT(1)=0
         STRAINI(1)=0
         STRESSI(1)=0
         V1(1)=VO
         V2(1)=0.0
         TMS(1)=0
         STRNRT(1)=(VO)/HOM
         SIGMAX=0.99*0.5*RHO*C*VO/1E6
         COUNT=1
C
C        OPEN OUTPUT FILES
C
         OPEN(UNIT=7,FILE='OUTPUT1.TXT',STATUS='UNKNOWN')
         WRITE(7,5) HM(1),HI(1),EC(1),T(1),DELT(1),STRAINI(1)
       +     ,STRESSI(1),TMS(1),STRNRT(1),V1(1), V2(1)
     5   FORMAT(11(F15.8,1X))
C
C        OPEN DEBUG FILE
C
         OPEN(UNIT=8,FILE='OUTPUT2.TXT',STATUS='UNKNOWN')
         OPEN(UNIT=9,FILE='OUTPUT3.TXT',STATUS='UNKNOWN')
         OPEN(UNIT=10,FILE='OUTPUT4.TXT',STATUS='UNKNOWN')
C
C        DO LOOP FOR FIRST TRAVEL OF WAVE (ST) IN STRIKER
C
         DO 1000 I=2,NPS
   100               DHM=HM(I-1)-HSTEPI
   200               DHI=DHM/0.0254
                     DEC=(HOM-DHM)/HOM
      DT=(HOM/VO)*(1.0/(1.0-AK*((DEC**AN)/((1.0-(DEC**AM))*(1.0-DEC)))))
       +             *(DEC-EC(I-1))+T(I-1)
                      DDELT=DT-T(I-1)
                      IF(I.EQ.2)THEN
                             DELTP=DDELT+1.5E-9
                             DELTM=DDELT-1.5E-9
                             GO TO 300
                      ENDIF
                      IF(DDELT.LE.DELTP.AND.DDELT.GE.DELTM)THEN
                             HSTEPI=HM(I-1)-DHM
                             GO TO 300
                      ENDIF
                      IF(DDELT.GT.DELT(2))THEN
                             DHM=DHM+STAR2
                      GO TO 200
                      ENDIF
                      IF(DDELT.LT.DELT(2))THEN
                             DHM=DHM-STAR2
                      GO TO 200
                      ENDIF
   300               HM(I)=DHM
                     HI(I)=DHI
                     EC(I)=DEC
```

```fortran
                        T(I)=DT
                        DELT(I)=DDELT
                STRAINI(I)=(SIGO*AO)/(E*A)*(EC(I)**AN)/((1.0-EC(I)**AM)
     +                  *(1.0-EC(I)))
                        STRESSI(I)=STRAINI(I)*(E/1E6)
                        IF(STRESSI(I).GE.SIGMAX)THEN
                                STRESSI(I)=SIGMAX
                                STRAINI(I)=STRESSI(I)/(E/1E6)
                                HM(I)=HM(I-1)
                                HI(I)=HI(I-1)
                                EC(I)=EC(I-1)
                                SIGCSTR=(STRESSI(I)*(1-EC(I))*A)/AO
                                ECSTR=EC(I)
                        ENDIF
                        V1(I)=VO-(STRESSI(I)*1E6)/(RHOST*CST)
                        V2(I)=(STRESSI(I)*1E6)/(RHO*C)
                        TMS(I)=T(I)*1E6
                        STRNRT(I)=(V1(I)-V2(I))/HOM
        WRITE(7,400)HM(I),HI(I),EC(I),T(I),DELT(I),STRAINI(I),
     +          STRESSI(I),TMS(I),STRNRT(I),V1(I),V2(I)
  400   FORMAT(11(F15.8,1X))
                        IF(STRNRT(I).LE.0.0)THEN
                                STRNRT(I)=0.0
                                NUN=I
                                N=I
                                GO TO 10001
                        ENDIF
                        IF(T(I).GE.ST)THEN
                                N=I
                                COUNT=2
                                GO TO 1001
                        ENDIF
 1000   CONTINUE
C
C       DO LOOP FOR SECOND TRAVEL OF WAVE (2*ST) IN STRIKER
C
 1001   PRINT*, 'GOING TO SECOND'
        DO 2000 II=N+1,NPS
                        DHM=HM(II-1)-STAR1
 2100                   DHI=DHM/0.0254
                        DEC=(HOM-DHM)/HOM
        DT=(HOM/VO)*(1.0/(1.0-AK*(DEC**AN)/((1.0-DEC**AM)*(1.0-DEC))-
     +          AK1*(EC(II-N)**AN)/((1.0-EC(II-N)**AM)*(1-EC(II-N)))))
     +          *(DEC-EC(II-1))+T(II-1)
                        DDELT=DT-T(II-1)
                        IF(DDELT.LE.0.0)THEN
                                NN=II-1
                                NUN=NN
                                SIGCSTR=(STRESSI(II-1)*(1-EC(II-1))*A)/AO
                                ECSTR=EC(II-1)
                                GO TO 10001
                        ENDIF
                        IF(DDELT.LE.DELTP.AND.DDELT.GE.DELTM)THEN
                                HSTEPI=HM(II-1)-DHM
                                GO TO 2200
                        ENDIF
                        IF(DDELT.GT.DELT(2))THEN
                                DHM=DHM+STAR3
                        GO TO 2100

                        ENDIF
                        IF(DDELT.LT.DELT(2))THEN
                                DHM=DHM-STAR3
                        GO TO 2100
                        ENDIF
 2200                   HM(II)=DHM
                        HI(II)=DHI
                        EC(II)=DEC
                        T(II)=DT
```

```fortran
                        DELT(II)=DDELT
                        STRAINI(II)=(SIGO*AO)/(E*A)*(EC(II)**AN)/((1.0-
     +                  EC(II)**AM)*(1.0-EC(II)))
                        STRESSI(II)=STRAINI(II)*(E/1E6)
                        IF(STRESSI(II).GT.((RHO*C*VO)/(2E6)))THEN
                                STRESSI(II)=(RHO*C*VO)/(2E6)
                                STRAINI(II)=STRESSI(II)/(E/1E6)
                        ENDIF
                V1(II)=(VO-(2*STRESSI(II-N)*1E6)/(RHOST*CST))-(STRESSI(II)*
     +                  1E6)/(RHOST*CST)
                        V2(II)=(STRESSI(II)*1E6)/(RHO*C)
                        TMS(II)=T(II)*1E6
                        STRNRT(II)=(V1(II)-V2(II))/HOM
        WRITE(7,2700)HM(II),HI(II),EC(II),T(II),DELT(II),STRAINI(II),
     +          STRESSI(II),TMS(II),STRNRT(II),V1(II),V2(II)
 2700   FORMAT(11(F15.8,1X))
                        IF(STRNRT(II).LE.0.0)THEN
                                STRNRT(II)=0.0
                                NN=II
                                NUN=II
                                PRINT *,ST
                                GO TO 10001
                        ENDIF
                        IF(II.EQ.(2*N))THEN
                                NN=II
                                COUNT=3
C                               WRITE(8,*)NN,T(II)
                                PRINT *,'GOING TO 3'
                                GO TO 2001
                        ENDIF
 2000   CONTINUE
C
C       DO LOOP FOR THIRD TRAVEL OF WAVE (3*ST) IN STRIKER
C
 2001   DO 3000 III=NN+1,NPS
                DHM=HM(III-1)-STAR1
 3100           DHI=DHM/0.0254
                DEC=(HOM-DHM)/HOM
                DT1=AK*(DEC**AN)/((1.0-DEC**AM)*(1.0-DEC))
                DT2=AK1*(EC(III-N)**AN)/((1.0-EC(III-N)**AM)*(1-EC(III-N)))
                DT3=AK1*(EC(III-NN)**AN)/((1.0-EC(III-NN)**AM)*(1-EC(III-NN)))
        DT=(HOM/VO)*(1.0/(1.0-DT1-DT2-DT3))*(DEC-EC(III-1))+T(III-1)
                DDELT=DT-T(III-1)
                IF(DDELT.LE.0.0)THEN
                        NNN=III-1
                        NUN=NNN
                        SIGCSTR=(STRESSI(III-1)*(1-EC(III-1))*A)/AO
                        ECSTR=EC(III-1)
                        GO TO 10001
                ENDIF
                        IF(DDELT.LE.DELTP.AND.DDELT.GE.DELTM)THEN
                        HSTEPI=HM(III-1)-DHM
                        GO TO 3200
                ENDIF
                IF(DDELT.GT.DELT(2))THEN
                        DHM=DHM+STAR3
                        GO TO 3100
                ENDIF
                IF(DDELT.LT.DELT(2))THEN
                        DHM=DHM-STAR3
                        GO TO 3100
                ENDIF
 3200           HM(III)=DHM
                HI(III)=DHI
                EC(III)=DEC
                T(III)=DT
                DELT(III)=DDELT
                STRAINI(III)=(SIGO*AO)/(E*A)*(EC(III)**AN)/
     +          ((1.0-EC(III)**AM)*(1.0-EC(III)))
```

```fortran
                 STRESSI(III)=STRAINI(III)*(E/1E6)
                 IF(STRESSI(III).GT.((RHO*C*VO)/(2E6)))THEN
                        STRESSI(III)=(RHO*C*VO)/(2E6)
                        STRAINI(III)=STRESSI(III)/(E/1E6)
                 ENDIF
                 V1(III)=VO-(STRESSI(III)*1E6)/(RHOST*CST)-(2*STRESSI(III-N)
      +          *1000000)/(RHOST*CST)-(2*STRESSI(III-NN)*1E6)/(RHOST*C)
                 V2(III)=(STRESSI(III)*1E6)/(RHO*C)
                 TMS(III)=T(III)*1E6
                 STRNRT(III)=(V1(III)-V2(III))/HOM
       WRITE(7,3700,ERR=999)HM(III),HI(III),EC(III),T(III),DELT(III),
      +          STRAINI(III),STRESSI(III),TMS(III),STRNRT(III),V1(III),V2(III)
 3700            FORMAT(11(F15.8,1X))
                 IF(STRNRT(III).LE.0.0)THEN
                        STRNRT(III)=0.0
                        NNN=III
                        NUN=III
                        GO TO 10001
                 ENDIF
                 IF(III.EQ.(3*N))THEN
                        NNN=III
                        COUNT=4
                        PRINT*,'GOING TO 4'
                        GO TO 4001
                 ENDIF
 3000 CONTINUE
C
C        DO LOOP FOR FORTH TRAVEL OF WAVE (4*ST) IN STRIKER
C
 4001    DO 4000 IIII=NNN+1,NPS
                 DHM=HM(IIII-1)-STAR1
 4100            DHI=DHM/0.0254
                 DEC=(HOM-DHM)/HOM
                 DT1=(DEC**AN)/((1.0-DEC**AM)*(1.0-DEC))
                 DT2=(EC(IIII-N)**AN)/((1.0-EC(IIII-N)**AM)*(1-EC(IIII-N)))
                 DT3=(EC(IIII-NN)**AN)/((1.0-EC(IIII-NN)**AM)*(1-EC(IIII-NN)))
        DT4=(EC(IIII-NNN)**AN)/((1.0-EC(IIII-NNN)**AM)*(1-EC(IIII-NNN)))
        DT=(HOM/VO)*(1.0/(1.0-AK*DT1-AK1*(DT2+DT3+DT4)))*
      +          (DEC-EC(IIII-1))+T(IIII-1)
                 DDELT=DT-T(IIII-1)
                 IF(DDELT.LE.0.0)THEN
                        NNNN=IIII-1
                        NUN=NNNN
                        SIGCSTR=(STRESSI(IIII-1)*(1-EC(IIII-1))*A)/AO
                        ECSTR=EC(IIII-1)
                        GO TO 10001
                 ENDIF
                 IF(DDELT.LE.DELTP.AND.DDELT.GE.DELTM)THEN
                        HSTEPI=HM(IIII-1)-DHM
                        GO TO 4200
                 ENDIF
                 IF(DDELT.GT.DELT(2))THEN
                        DHM=DHM+STAR3
                        GO TO 4100
                 ENDIF
                 IF(DDELT.LT.DELT(2))THEN
                        DHM=DHM-STAR3
                        GO TO 4100
                 ENDIF
 4200            HM(IIII)=DHM
                 HI(IIII)=DHI
                 EC(IIII)=DEC
                 T(IIII)=DT
                 DELT(IIII)=DDELT
        STRAINI(IIII)=(SIGO*AO)/(E*A)*(EC(IIII)**AN)/((1.0-
      +          EC(IIII)**AM)*(1.0-EC(IIII)))
                 STRESSI(IIII)=STRAINI(IIII)*(E/1E6)
                 IF(STRESSI(IIII).GT.((RHO*C*VO)/(2E6)))THEN
                        STRESSI(IIII)=(RHO*C*VO)/(2E6)
```

```
                              STRAINI(IIII)=STRESSI(IIII)/(E/1E6)
                  ENDIF
                  V1(IIII)=VO-(STRESSI(IIII)*1E6)/(RHOST*CST)-(2*STRESSI(IIII-N)
         +        *1E6)/(RHOST*CST)-(2*STRESSI(IIII-NN)*1E6)/
         +        (RHOST*CST)-(2*STRESSI(IIII-NNN)*1E6)/(RHOST*CST)
                  V2(IIII)=(STRESSI(IIII)*1E6)/(RHO*C)
                  TMS(IIII)=T(IIII)*1E6
                  STRNRT(IIII)=(V1(IIII)-V2(IIII))/HOM
                  PRINT *, IIII, EC(IIII), TMS(IIII)
         WRITE(7,4700,ERR=999)HM(IIII),HI(IIII),EC(IIII),T(IIII),
        + DELT(IIII),STRAINI(IIII),STRESSI(IIII),TMS(IIII),STRNRT(IIII),
        + V1(IIII),V2(IIII)
 4700    FORMAT(11(F15.8,1X))
                  STRNRT(IIII)=(V1(IIII)-V2(IIII))/HOM
                  IF(STRNRT(IIII).LE.0.0)THEN
                              STRNRT(IIII)=0.0
                              NNNN=IIII
                              NUN=IIII
                              GO TO 10001
                  ENDIF
                  IF(IIII.EQ.(4*N))THEN
                          NNNN=IIII
                          NIV=IIII
                          COUNT=5
                          PRINT*,'GOING TO 5'
                          GO TO 5001
                  ENDIF
          NNNN=IIII
 4000    CONTINUE
C
C        DO LOOP FOR FIFTH TRAVEL OF WAVE (5*ST) IN STRIKER
C
 5001    DO 5000 IIIII=NNNN+1,NPS
                  DHM=HM(IIIII-1)-STAR3
 5100             DHI=DHM/0.0254
                  DEC=(HOM-DHM)/HOM
                  DT1=(DEC**AN)/((1.0-DEC**AM)*(1.0-DEC))
                  DT2=(EC(IIIII-N)**AN)/((1.0-EC(IIIII-N)**AM)*(1-EC(IIIII-N)))
          DT3=(EC(IIIII-NN)**AN)/((1.0-EC(IIIII-NN)**AM)*(1-EC(IIIII-NN)))
                  DT4=(EC(IIIII-NNN)**AN)/((1.0-EC(IIIII-NNN)**AM)*
         +        (1-EC(IIIII-NNN)))
                  DT5=(EC(IIIII-NNNN)**AN)/((1.0-EC(IIIII-NNNN)**AM)*
         +        (1-EC(IIIII-NNNN)))
          DT=(HOM/VO)*(1.0/(1.0-AK*DT1-AK1*(DT2+DT3+DT4+DT5)))*
         +        (DEC-EC(IIIII-1))+T(IIIII-1)
                  DDELT=DT-T(IIIII-1)
                  IF(DDELT.LE.0.0)THEN
                          NNNN=IIIII-1
                          NUN=NNNN
                          SIGCSTR=(STRESSI(IIIII-1)*(1-EC(IIIII-1))*A)/AO
                          ECSTR=EC(IIIII-1)
                          GO TO 10001
                  ENDIF
                  IF(DDELT.LE.DELTP.AND.DDELT.GE.DELTM)THEN
                          HSTEPI=HM(IIIII-1)-DHM
                          GO TO 5200
                  ENDIF
                  IF(DDELT.GT.DELT(2))THEN
                          DHM=DHM+STAR4
                          GO TO 5100
                  ENDIF
                  IF(DDELT.LT.DELT(2))THEN
                          DHM=DHM-STAR4
                          GO TO 5100
                  ENDIF
 5200             HM(IIIII)=DHM
                  HI(IIIII)=DHI
                  EC(IIIII)=DEC
                  T(IIIII)=DT
```

```
              DELT(IIIII)=DDELT
        STRAINI(IIIII)=(SIGO*AO)/(E*A)*(EC(IIIII)**AN)/
     +          ((1-EC(IIIII)**AM)*(1.0-EC(IIIII)))
              STRESSI(IIIII)=STRAINI(IIIII)*(E/1E6)
              IF(STRESSI(IIIII).GT.((RHO*C*VO)/(2E6)))THEN
                      STRESSI(IIIII)=(RHO*C*VO)/(2E6)
                      STRAINI(IIIII)=STRESSI(IIIII)/(E/1E6)
              ENDIF
        V1(IIIII)=VO-(STRESSI(IIIII)*1E6)/(RHOST*CST)-(2*STRESSI(IIIII-N)
     +       *1000000)/(RHOST*CST)-(2*STRESSI(IIIII-NN)*1000000)/(RHOST*CST)
     +       -(2*STRESSI(IIIII-NNN)*1E6)/(RHOST*CST)-(2*STRESSI(IIIII-NNNN)
     +       *1E6)/(RHOST*CST)
        V2(IIIII)=(STRESSI(IIIII)*1E6)/(RHO*C)
              TMS(IIIII)=T(IIIII)*1E6
              STRNRT(IIIII)=(V1(IIIII)-V2(IIIII))/HOM
                      PRINT *, IIIII, EC(IIIII), TMS(IIIII)
        WRITE(7,5700,ERR=999)HM(IIIII),HI(IIIII),EC(IIIII),T(IIIII),
     +       DELT(IIIII),STRAINI(IIIII),STRESSI(IIIII),TMS(IIIII),
     +       STRNRT(IIIII),V1(IIIII),V2(IIIII)
 5700   FORMAT(11(F15.8,1X))
              IF(STRNRT(IIIII).LE.0.0)THEN
                            STRNRT(IIIII)=0.0
                            NNNNN=IIIII
                            NUN=IIIII
                            PRINT *, 'STRNRT ZERO'
                            GO TO 10001
              ENDIF
              IF(IIIII.EQ.(5*N))THEN
                      NV=IIIII
                      NNNNN=IIIII
                      COUNT=6
                      PRINT*, 'GOING TO 6'
                      GO TO 6001
              ENDIF
        NNNNN=IIIII
 5000   CONTINUE
C
C       DO LOOP FOR SIXTH TRAVEL OF WAVE (6*ST) IN STRIKER
C
 6001   DO 6000 IV=NNNNN+1,NPS
              DHM=HM(IV-1)-STAR3
 6100         DHI=DHM/0.0254
              DEC=(HOM-DHM)/HOM
              DT1=(DEC**AN)/((1.0-DEC**AM)*(1.0-DEC))
              DT2=(EC(IV-N)**AN)/((1.0-EC(IV-N)**AM)*(1-EC(IV-N)))
              DT3=(EC(IV-NN)**AN)/((1.0-EC(IV-NN)**AM)*(1-EC(IV-NN)))
              DT4=(EC(IV-NNN)**AN)/((1.0-EC(IV-NNN)**AM)*(1-EC(IV-NNN)))
              DT5=(EC(IV-NNNN)**AN)/((1.0-EC(IV-NNNN)**AM)*(1-EC(IV-NNNN)))
        DT6=(EC(IV-NNNNN)**AN)/((1.0-EC(IV-NNNNN)**AM)*(1-EC(IV-NNNNN)))
        DT=(HOM/VO)*(1.0/(1.0-AK*DT1-AK1*(DT2+DT3+DT4+DT5+DT6)))*
     +       (DEC-EC(IV-1))+T(IV-1)
              DDELT=DT-T(IV-1)
              IF(DDELT.LE.0.0)THEN
                      NNNN=IV-1
                      NUN=NNNN
                      SIGCSTR=(STRESSI(IV-1)*(1-EC(IV-1))*A)/AO
                      ECSTR=EC(IV-1)
                      PRINT*, 'DDELT.LE.0.0'
                      GO TO 10001
              ENDIF
              IF(DDELT.LE.DELTP.AND.DDELT.GE.DELTM)THEN
                      HSTEPI=HM(IV-1)-DHM
                      GO TO 6200
              ENDIF
              IF(DDELT.GT.DELT(2))THEN
                      DHM=DHM+STAR4
                      GO TO 6100
              ENDIF
              IF(DDELT.LT.DELT(2))THEN
```

```fortran
                          DHM=DHM-STAR4
                          GO TO 6100
                ENDIF
 6200           HM(IV)=DHM
                HI(IV)=DHI
                EC(IV)=DEC
                T(IV)=DT
                DELT(IV)=DDELT
        STRAINI(IV)=(SIGO*AO)/(E*A)*(EC(IV)**AN)/((1-EC(IV)**AM)*
     +          (1.0-EC(IV)))
                STRESSI(IV)=STRAINI(IV)*(E/1E6)
                IF(STRESSI(IV).GT.((RHO*C*VO)/(2E6)))THEN
                          STRESSI(IV)=(RHO*C*VO)/(2E6)
                          STRAINI(IV)=STRESSI(IV)/(E/1E6)
                ENDIF
        V1(IV)=VO-(STRESSI(IV)*1E6)/(RHOST*CST)-(2*STRESSI(IV-N)
     +          *1000000)/(RHOST*CST)-(2*STRESSI(IV-NN)*1000000)/(RHOST*CST)
     +          -(2*STRESSI(IV-NNN)*1E6)/(RHOST*CST)-(2*STRESSI(IV-NNNN)
     +          *1E6)/(RHOST*CST)-(2*STRESSI(IV-NNNNN)*1E6)/(RHOST*CST)
                          V2(IV)=(STRESSI(IV)*1E6)/(RHO*C)
                TMS(IV)=T(IV)*1E6
                STRNRT(IV)=(V1(IV)-V2(IV))/HOM
                PRINT *, IV, EC(IV), TMS(IV)
        WRITE(7,6700,ERR=999)HM(IV),HI(IV),EC(IV),T(IV),
     +          DELT(IV),STRAINI(IV),STRESSI(IV),TMS(IV),STRNRT(IV),
     +          V1(IV),V2(IV)
 6700   FORMAT(11(F15.8,1X))
                STRNRT(IV)=(V1(IV)-V2(IV))/HOM
                IF(STRNRT(IV).LE.0.0)THEN
                          STRNRT(IV)=0.0
                          NSIX=IV
                          NUN=IV
                          PRINT *, 'STRNRT ZERO'
                          GO TO 10001
                ENDIF
                IF(IV.EQ.(6*N))THEN
                          NVI=IV
                          NSIX=IV
                          COUNT=7
                          PRINT *,'GOING TO 7'
                          GO TO 7001
                ENDIF
        NSIX=IV
 6000   CONTINUE
C
C       DO LOOP FOR SEVENTH TRAVEL OF WAVE (7*ST) IN STRIKER
C
 7001   DO 7000 IVI=NSIX+1,NPS
                DHM=HM(IVI-1)-STAR1
 7100           DHI=DHM/0.0254
                DEC=(HOM-DHM)/HOM
                DT1=(DEC**AN)/((1.0-DEC**AM)*(1.0-DEC))
                DT2=(EC(IVI-N)**AN)/((1.0-EC(IVI-N)**AM)*(1-EC(IVI-N)))
                DT3=(EC(IVI-NN)**AN)/((1.0-EC(IVI-NN)**AM)*(1-EC(IVI-NN)))
                DT4=(EC(IVI-NNN)**AN)/((1.0-EC(IVI-NNN)**AM)*(1-EC(IVI-NNN)))
        DT5=(EC(IVI-NNNN)**AN)/((1.0-EC(IVI-NNNN)**AM)*(1-EC(IVI-NNNN)))
        DT6=(EC(IVI-NNNNN)**AN)/((1.0-EC(IVI-NNNNN)**AM)*
     +          (1-EC(IVI-NNNNN)))
        DT7=(EC(IVI-NSIX)**AN)/((1.0-EC(IVI-NSIX)**AM)*
     +          (1-EC(IVI-NSIX)))
        DT=(HOM/VO)*(1.0/(1.0-AK*DT1-AK1*(DT2+DT3+DT4+DT5+DT6+DT7)))*
     +          (DEC-EC(IVI-1))+T(IVI-1)
                DDELT=DT-T(IVI-1)
                IF(DDELT.LE.0.0)THEN
                          NUN=IVI-1
                          SIGCSTR=(STRESSI(IVI-1)*(1-EC(IVI-1))*A)/AO
                          ECSTR=EC(IVI-1)
                          PRINT*, 'DDELT.LE.0.0'
                          GO TO 10001
```

```fortran
                ENDIF
                IF(DDELT.LE.DELTP.AND.DDELT.GE.DELTM)THEN
                        HSTEPI=HM(IVI-1)-DHM
                        GO TO 7200
                ENDIF
                IF(DDELT.GT.DELT(2))THEN
                        DHM=DHM+STAR3
                        GO TO 7100
                ENDIF
                IF(DDELT.LT.DELT(2))THEN
                        DHM=DHM-STAR3
                        GO TO 7100
                ENDIF
7200            HM(IVI)=DHM
                HI(IVI)=DHI
                EC(IVI)=DEC
                T(IVI)=DT
                DELT(IVI)=DDELT
        STRAINI(IVI)=(SIGO*AO)/(E*A)*(EC(IVI)**AN)/((1-EC(IVI)**AM)*
     +          (1.0-EC(IVI)))
                STRESSI(IVI)=STRAINI(IVI)*(E/1E6)
                IF(STRESSI(IVI).GT.((RHO*C*VO)/(2E6)))THEN
                        STRESSI(IVI)=(RHO*C*VO)/(2E6)
                        STRAINI(IVI)=STRESSI(IVI)/(E/1E6)
                ENDIF
        V1(IVI)=VO-(STRESSI(IVI)*1E6)/(RHOST*CST)-(2*STRESSI(IVI-N)
     +          *1000000)/(RHOST*CST)-(2*STRESSI(IVI-NN)*1000000)/(RHOST*CST)
     +          -(2*STRESSI(IVI-NNN)*1E6)/(RHOST*CST)-(2*STRESSI(IVI-NNNN)
     +          *1E6)/(RHOST*CST)-(2*STRESSI(IVI-NNNNN)*1E6)/(RHOST*CST)
     +          -(2*STRESSI(IVI-NSIX)*1E6)/(RHOST*CST)
         V2(IVI)=(STRESSI(IVI)*1E6)/(RHO*C)
                TMS(IVI)=T(IVI)*1E6
                STRNRT(IVI)=(V1(IVI)-V2(IVI))/HOM
                PRINT *, IVI, EC(IVI), TMS(IVI)
        WRITE(7,7700,ERR=999)HM(IVI),HI(IVI),EC(IVI),T(IVI),
     +          DELT(IVI),STRAINI(IVI),STRESSI(IVI),TMS(IVI),STRNRT(IVI),
     +          V1(IVI),V2(IVI)
7700    FORMAT(11(F15.8,1X))
                IF(STRNRT(IVI).LE.0.0)THEN
                                STRNRT(IVI)=0.0
                                NSEV=IVI
                                PRINT *, 'STRNRT ZERO'
                                GO TO 10001
                ENDIF
                IF(IVI.EQ.(7*N))THEN
                        NVII=IVI
                        NSEV=IVI
                        COUNT=8
                        PRINT*,'GOING TO 8'
                        GO TO 8001
                ENDIF
        NSEV=IVI
7000    CONTINUE
C
C       DO LOOP FOR EIGHTH TRAVEL OF WAVE (8*ST) IN STRIKER
C
8001    DO 8000 IVII=NSEV+1,NPS
                DHM=HM(IVII-1)-STAR1
8100            DHI=DHM/0.0254
                DEC=(HOM-DHM)/HOM
        DT1=(DEC**AN)/((1.0-DEC**AM)*(1.0-DEC))
        DT2=(EC(IVII-N)**AN)/((1.0-EC(IVII-N)**AM)*(1-EC(IVII-N)))
        DT3=(EC(IVII-NN)**AN)/((1.0-EC(IVII-NN)**AM)*(1-EC(IVII-NN)))
        DT4=(EC(IVII-NNN)**AN)/((1.0-EC(IVII-NNN)**AM)*(1-EC(IVII-NNN)))
        DT5=(EC(IVII-NNNN)**AN)/((1.0-EC(IVII-NNNN)**AM)*
     +          (1-EC(IVII-NNNN)))
        DT6=(EC(IVII-NNNNN)**AN)/((1.0-EC(IVII-NNNNN)**AM)*
     +          (1-EC(IVII-NNNNN)))
        DT7=(EC(IVII-NSIX)**AN)/((1.0-EC(IVII-NSIX)**AM)*
```

```fortran
     +            (1-EC(IVII-NSIX)))
      DT8=(EC(IVII-NSEV)**AN)/((1.0-EC(IVII-NSEV)**AM)*
     +            (1-EC(IVII-NSEV)))
      DT=(HOM/VO)*(1.0/(1.0-AK*DT1*AK1*(DT2+DT3+DT4+DT5+DT6+DT7+DT8)))*
     +            (DEC-EC(IVII-1))+T(IVII-1)
              DDELT=DT-T(IVII-1)
              IF(DDELT.LE.0.0)THEN
                      PRINT*,'*'
                      NUN=IVII-1
                      SIGCSTR=(STRESSI(IVII-1)*(1-EC(IVII-1))*A)/AO
                      ECSTR=EC(IVII-1)
                      PRINT*, 'DDELT.LE.0.0'
                      GO TO 10001
              ENDIF
              IF(DDELT.LE.DELTP.AND.DDELT.GE.DELTM)THEN
                      HSTEPI=HM(IVII-1)-DHM
                      GO TO 8200
              ENDIF
              IF(DDELT.GT.DELT(2))THEN
                      DHM=DHM+STAR3
                      GO TO 8100
              ENDIF
              IF(DDELT.LT.DELT(2))THEN
                      DHM=DHM-STAR3
                      GO TO 8100
              ENDIF
 8200         HM(IVII)=DHM
              HI(IVII)=DHI
              EC(IVII)=DEC
              T(IVII)=DT
              DELT(IVII)=DDELT
      STRAINI(IVII)=(SIGO*AO)/(E*A)*(EC(IVII)**AN)/(1.0-EC(IVII))
              STRESSI(IVII)=STRAINI(IVII)*(E/1E6)
              IF(STRESSI(IVII).GT.((RHO*C*VO)/(2E6)))THEN
                      STRESSI(IVII)=(RHO*C*VO)/(2E6)
                      STRAINI(IVII)=STRESSI(IVII)/(E/1E6)
              ENDIF
      V1(IVII)=VO-(STRESSI(IVII)*1E6)/(RHOST*CST)-(2*STRESSI(IVII-N)
     +       *1000000)/(RHOST*CST)-(2*STRESSI(IVII-NN)*1000000)/(RHOST*CST)
     +       -(2*STRESSI(IVII-NNN)*1E6)/(RHOST*CST)-(2*STRESSI(IVII-NNNN)
     +       *1E6)/(RHOST*CST)-(2*STRESSI(IVII-NNNNN)*1E6)/(RHOST*CST)
     +       -(2*STRESSI(IVII-NSIX)*1E6)/(RHOST*CST)-(2*STRESSI(IVII-NSEV)
     +       *1E6)/(RHOST*CST)
      V2(IVII)=(STRESSI(IVII)*1E6)/(RHO*C)
              TMS(IVII)=T(IVII)*1E6
              STRNRT(IVII)=(V1(IVII)-V2(IVII))/HOM
              PRINT *, IVII, EC(IVII), TMS(IVII)
      WRITE(7,8700,ERR=999)HM(IVII),HI(IVII),EC(IVII),T(IVII),
     +       DELT(IVII),STRAINI(IVII),STRESSI(IVII),TMS(IVII),STRNRT(IVII),
     +       V1(IVII),V2(IVII)
 8700 FORMAT(11(F15.8,1X))
              IF(STRNRT(IVII).LE.0.0)THEN
                              STRNRT(IVII)=0.0
                              NUN=IVII
                              PRINT *, 'STRNRT ZERO'
                              GO TO 10001
              ENDIF
              IF(IVII.EQ.(8*N))THEN
                      NVIII=IVII
                      NUN=IVII
                      COUNT=9
                      GO TO 10001
              ENDIF
      NEIG=IVII
 8000 CONTINUE
  999 PRINT *,'BAD'
C
C     UNLOADING
C
```

```fortran
10001    PRINT *,'UNLOADING'
         PRINT *, N,NN,NNN,NIV,NV,NVI,NVII
         VALUE=DELT(2)
         DO 10000 J=NUN+1,NPS
                 DHM=HM(J-1)+STAR4
10100                    DHI=DHM/0.0254
                         DEC=(HOM-DHM)/HOM
                         IF(COUNT.EQ.11)THEN
                                 STRESSJJN=STRESSI(J-N)
                                 STRESSJJNN=STRESSI(J-NN)
                                 STRESSJJNNN=STRESSI(J-NNN)
                                 STRESSJJNIV=STRESSI(J-NIV)
                                 STRESSJJNV=STRESSI(J-NV)
                                 STRESSJJNVI=STRESSI(J-NVI)
                                 STRESSJJNVII=STRESSI(J-NVII)
                                 STRESSJJNVIII=STRESSI(J-NVIII)
                                 STRESSJJNIX=STRESSI(J-NIX)
                                 STRESSJJNX=STRESSI(J-NX)
                                 VALUE1=1-(2*STRESSJJN*1E6)/(VO*RHOST*CST)
                                 VALUE2=(2*STRESSJJNN*1E6)/(VO*RHOST*CST)
                                 VALUE3=(2*STRESSJJNNN*1E6)/(VO*RHOST*CST)
                                 VALUE4=(2*STRESSJJNIV*1E6)/(VO*RHOST*CST)
                                 VALUE5=(2*STRESSJJNV*1E6)/(VO*RHOST*CST)
                                 VALUE6=(2*STRESSJJNVI*1E6)/(VO*RHOST*CST)
                                 VALUE7=(2*STRESSJJNVII*1E6)/(VO*RHOST*CST)
                                 VALUE8=(2*STRESSJJNVIII*1E6)/(VO*RHOST*CST)
                                 VALUE9=(2*STRESSJJNIX*1E6)/(VO*RHOST*CST)
                                 VALUE10=(2*STRESSJJNX*1E6)/(VO*RHOST*CST)
                                 VALUE11=(AO)/(VO*A*(1-DEC))*(1/(RHO*C)+1/(RHOST*CST))
       +                                 *((SIGCSTR*1E6)-YOUNGC*(ECSTR-DEC))
                 DT=(HOM/VO)*(1.0/(VALUE1-VALUE2-VALUE3-VALUE4
       +                 -VALUE5-VALUE6-VALUE7-VALUE8-VALUE9-VALUE10-VALUE11))*
       +                 (DEC-EC(J-1))+T(J-1)
                         ENDIF
                         IF(COUNT.EQ.10)THEN
                                 STRESSJJN=STRESSI(J-N)
                                 STRESSJJNN=STRESSI(J-NN)
                                 STRESSJJNNN=STRESSI(J-NNN)
                                 STRESSJJNIV=STRESSI(J-NIV)
                                 STRESSJJNV=STRESSI(J-NV)
                                 STRESSJJNVI=STRESSI(J-NVI)
                                 STRESSJJNVII=STRESSI(J-NVII)
                                 STRESSJJNVIII=STRESSI(J-NVIII)
                                 STRESSJJNIX=STRESSI(J-NIX)
                                 VALUE1=1-(2*STRESSJJN*1E6)/(VO*RHOST*CST)
                                 VALUE2=(2*STRESSJJNN*1E6)/(VO*RHOST*CST)
                                 VALUE3=(2*STRESSJJNNN*1E6)/(VO*RHOST*CST)
                                 VALUE4=(2*STRESSJJNIV*1E6)/(VO*RHOST*CST)
                                 VALUE5=(2*STRESSJJNV*1E6)/(VO*RHOST*CST)
                                 VALUE6=(2*STRESSJJNVI*1E6)/(VO*RHOST*CST)
                                 VALUE7=(2*STRESSJJNVII*1E6)/(VO*RHOST*CST)
                                 VALUE8=(2*STRESSJJNVIII*1E6)/(VO*RHOST*CST)
                                 VALUE9=(2*STRESSJJNIX*1E6)/(VO*RHOST*CST)
                                 VALUE10=(AO)/(VO*A*(1-DEC))*(1/(RHO*C)+1/(RHOST*CST))
       +                                 *((SIGCSTR*1E6)-YOUNGC*(ECSTR-DEC))
                 DT=(HOM/VO)*(1.0/(VALUE1-VALUE2-VALUE3-VALUE4
       +                 -VALUE5-VALUE6-VALUE7-VALUE8-VALUE9-VALUE10))*
       +                 (DEC-EC(J-1))+T(J-1)
                         ENDIF
                         IF(COUNT.EQ.9)THEN
                                 STRESSJJN=STRESSI(J-N)
                                 STRESSJJNN=STRESSI(J-NN)
                                 STRESSJJNNN=STRESSI(J-NNN)
                                 STRESSJJNIV=STRESSI(J-NIV)
                                 STRESSJJNV=STRESSI(J-NV)
                                 STRESSJJNVI=STRESSI(J-NVI)
                                 STRESSJJNVII=STRESSI(J-NVII)
                                 STRESSJJNVIII=STRESSI(J-NVIII)
                                 VALUE1=1-(2*STRESSJJN*1E6)/(VO*RHOST*CST)
```

```
                                    VALUE2=(2*STRESSJJNN*1E6)/(VO*RHOST*CST)
                                    VALUE3=(2*STRESSJJNNN*1E6)/(VO*RHOST*CST)
                                    VALUE4=(2*STRESSJJNIV*1E6)/(VO*RHOST*CST)
                                    VALUE5=(2*STRESSJJNV*1E6)/(VO*RHOST*CST)
                                    VALUE6=(2*STRESSJJNVI*1E6)/(VO*RHOST*CST)
                                    VALUE7=(2*STRESSJJNVII*1E6)/(VO*RHOST*CST)
                                    VALUE8=(2*STRESSJJNVIII*1E6)/(VO*RHOST*CST)
                                    VALUE9=(AO)/(VO*A*(1-DEC))*(1/(RHO*C)+1/(RHOST*CST))
         +                              *((SIGCSTR*1E6)-YOUNGC*(ECSTR-DEC))
                            DT=(HOM/VO)*(1.0/(VALUE1-VALUE2-VALUE3-VALUE4
         +              -VALUE5-VALUE6-VALUE7-VALUE8-VALUE9))*(DEC-EC(J-1))+T(J-1)
                            ENDIF
                            IF(COUNT.EQ.8)THEN
                                    STRESSJJN=STRESSI(J-N)
                                    STRESSJJNN=STRESSI(J-NN)
                                    STRESSJJNNN=STRESSI(J-NNN)
                                    STRESSJJNIV=STRESSI(J-NIV)
                                    STRESSJJNV=STRESSI(J-NV)
                                    STRESSJJNVI=STRESSI(J-NVI)
                                    STRESSJJNVII=STRESSI(J-NVII)
                                    VALUE1=1-(2*STRESSJJN*1E6)/(VO*RHOST*CST)
                                    VALUE2=(2*STRESSJJNN*1E6)/(VO*RHOST*CST)
                                    VALUE3=(2*STRESSJJNNN*1E6)/(VO*RHOST*CST)
                                    VALUE4=(2*STRESSJJNIV*1E6)/(VO*RHOST*CST)
                                    VALUE5=(2*STRESSJJNV*1E6)/(VO*RHOST*CST)
                                    VALUE6=(2*STRESSJJNVI*1E6)/(VO*RHOST*CST)
                                    VALUE7=(2*STRESSJJNVII*1E6)/(VO*RHOST*CST)
                            VALUE8=(AO)/(VO*A*(1-DEC))*(1/(RHO*C)+1/(RHOST*CST))
         +                              *((SIGCSTR*1E6)-YOUNGC*(ECSTR-DEC))
                    DT=(HOM/VO)*(1.0/(VALUE1-VALUE2-VALUE3-VALUE4
         +                  -VALUE5-VALUE6-VALUE7-VALUE8))*(DEC-EC(J-1))+T(J-1)
                            ENDIF
                            IF(COUNT.EQ.7)THEN
                                    STRESSJJN=STRESSI(J-N)
                                    STRESSJJNN=STRESSI(J-NN)
                                    STRESSJJNNN=STRESSI(J-NNN)
                                    STRESSJJNIV=STRESSI(J-NIV)
                                    STRESSJJNV=STRESSI(J-NV)
                                    STRESSJJNVI=STRESSI(J-NVI)
                                    VALUE1=1-(2*STRESSJJN*1E6)/(VO*RHOST*CST)
                                    VALUE2=(2*STRESSJJNN*1E6)/(VO*RHOST*CST)
                                    VALUE3=(2*STRESSJJNNN*1E6)/(VO*RHOST*CST)
                                    VALUE4=(2*STRESSJJNIV*1E6)/(VO*RHOST*CST)
                                    VALUE5=(2*STRESSJJNV*1E6)/(VO*RHOST*CST)
                                    VALUE6=(2*STRESSJJNVI*1E6)/(VO*RHOST*CST)
                                    VALUE7=(AO)/(VO*A*(1-DEC))*(1/(RHO*C)+1/(RHOST*CST))
         +                              *((SIGCSTR*1E6)-YOUNGC*(ECSTR-DEC))
                                    DT=(HOM/VO)*(1.0/(VALUE1-VALUE2-VALUE3-VALUE4
         +                              -VALUE5-VALUE6-VALUE7))*(DEC-EC(J-1))+T(J-1)
                            ENDIF
                            IF(COUNT.EQ.6)THEN
                                    STRESSJJN=STRESSI(J-N)
                                    STRESSJJNN=STRESSI(J-NN)
                                    STRESSJJNNN=STRESSI(J-NNN)
                                    STRESSJJNIV=STRESSI(J-NIV)
                                    STRESSJJNV=STRESSI(J-NV)
                                    VALUE1=1-(2*STRESSJJN*1E6)/(VO*RHO*C)
                                    VALUE2=(2*STRESSJJNN*1E6)/(VO*RHO*C)
                                    VALUE3=(2*STRESSJJNNN*1E6)/(VO*RHO*C)
                                    VALUE4=(2*STRESSJJNIV*1E6)/(VO*RHO*C)
                                    VALUE5=(2*STRESSJJNV*1E6)/(VO*RHO*C)
                                    VALUE6=(AO)/(VO*A*(1-DEC))*(1/(RHO*C)+1/(RHOST*CST))
         +                              *((SIGCSTR*1E6)-YOUNGC*(ECSTR-DEC))
                                    DT=(HOM/VO)*(1.0/(VALUE1-VALUE2-VALUE3-VALUE4
         +                              -VALUE5-VALUE6))*(DEC-EC(J-1))+T(J-1)
                            ENDIF
                            IF(COUNT.EQ.5)THEN
                                    STRESSJJN=STRESSI(J-N)
                                    STRESSJJNN=STRESSI(J-NN)
```

```fortran
                    STRESSJJNNN=STRESSI(J-NNN)
                    STRESSJJNIV=STRESSI(J-NIV)
                    VALUE1=1-(2*STRESSJJN*1E6)/(VO*RHOST*C)
                    VALUE2=(2*STRESSJJNN*1E6)/(VO*RHOST*CST)
                    VALUE3=(2*STRESSJJNNN*1E6)/(VO*RHOST*CST)
                    VALUE4=(2*STRESSJJNIV*1E6)/(VO*RHOST*CST)
                    VALUE5=(AO)/(VO*A*(1-DEC))*(1/(RHO*C)+1/(RHOST*CST))
     +                  *((SIGCSTR*1E6)-YOUNGC*(ECSTR-DEC))
                        DT=(HOM/VO)*(1.0/(VALUE1-VALUE2-VALUE3-VALUE4-
     +                       VALUE5))*(DEC-EC(J-1))+T(J-1)
                ENDIF
                IF(COUNT.EQ.4)THEN
                    STRESSJJN=STRESSI(J-N)
                    STRESSJJNN=STRESSI(J-NN)
                    STRESSJJNNN=STRESSI(J-NNN)
                    VALUE1=1-(2*STRESSJJN*1E6)/(VO*RHOST*CST)
                    VALUE2=(2*STRESSJJNN*1E6)/(VO*RHOST*CST)
                    VALUE3=(2*STRESSJJNNN*1E6)/(VO*RHOST*CST)
                    VALUE4=(AO)/(VO*A*(1-DEC))*(1/(RHO*C)+1/(RHOST*CST))
     +                    *((SIGCSTR*1E6)-YOUNGC*(ECSTR-DEC))
                    DT=(HOM/VO)*(1.0/(VALUE1-VALUE2-VALUE3-VALUE4))*
     +                     (DEC-EC(J-1))+T(J-1)
                ENDIF
                IF(COUNT.EQ.3)THEN
                    STRESSJJN=STRESSI(J-N)
                    STRESSJJNN=STRESSI(J-NN)
                    VALUE1=1-(2*STRESSJJN*1E6)/(VO*RHOST*CST)
                    VALUE2=(2*STRESSJJNN*1E6)/(VO*RHOST*CST)
                    VALUE4=(AO)/(VO*A*(1-DEC))*(1/(RHO*C)+1/(RHOST*CST))
     +                     *((SIGCSTR*1E6)-YOUNGC*(ECSTR-DEC))
                    DT=(HOM/VO)*(1.0/(VALUE1-VALUE2-VALUE4))*
     +                     (DEC-EC(J-1))+T(J-1)
                ENDIF
                IF(COUNT.EQ.2)THEN
                    STRESSJJN=STRESSI(J-N)
                    VALUE1=1-(2*STRESSJJN*1E6)/(VO*RHO*C)
                    VALUE4=(AO)/(VO*A*(1-DEC))*(1/(RHO*C)+1/(RHOST*CST))
     +                     *((SIGCSTR*1E6)-YOUNGC*(ECSTR-DEC))
                    DT=(HOM/VO)*(1.0/(VALUE1-VALUE4))*
     +                     (DEC-EC(J-1))+T(J-1)
                ENDIF
                DDELT=DT-T(J-1)
C
C     FIRST DATA POINT WILL HAVE VERY LITTLE CHANGE IN STRAIN.
C     THEREFORE, IT IS NECESSARY TO LET TIME ADVANCE AND HOLD STRAINS
C     CONSTANT.
C
                IF(DDELT.LT.0.0)THEN
                        DELT(J)=DELT(J-1)
                        T(J)=T(J-1)+DELT(J)
                        TMS(J)=T(J)*1E6
                        STRESSI(J)=STRESSI(J-1)
                        STRAINI(J)=STRAINI(J-1)
                        HM(J)=HM(J-1)
                        HI(J)=HI(J-1)
                        EC(J)=EC(J-1)
     V1(J)=VO-(STRESSI(J)*1E6)/(RHOST*CST)-(2*STRESSJJN*1E6)/
     +         (RHOST*CST)-(2*STRESSJJNN*1E6)/(RHOST*CST)-(2*STRESSJJNNN*1E6)/
     +         (RHOST*CST)-(2*STRESSJJNNN*1E6)/(RHOST*CST)-(2*STRESSJJNIV*1E6)/
     +         (RHOST*CST)-(2*STRESSJJNV*1E6)/(RHOST*CST)-(2*STRESSJJNVI*1E6)/
     +         (RHOST*CST)-(2*STRESSJJNVII*1E6)/(RHOST*CST)-(2*STRESSJJNVIII*1E6)
     +         /(RHOST*CST)-(2*STRESSJJNIX*1E6)/(RHOST*CST)-(2*STRESSJJNX*1E6)/
     +         (RHOST*CST)
                        V2(J)=(STRESSI(J)*1E6)/(RHO*C)
                            STRNRT(J)=(V1(J)-V2(J))/HOM
                            GOTO 10201
                ENDIF
                IF(DDELT.LE.DELTP.AND.DDELT.GE.DELTM)THEN
                    GO TO 10200
```

```fortran
                        ENDIF
                        IF(DDELT.GT.VALUE)THEN
                                IF(BETA.EQ.0)THEN
                                        DHM=DHM-STAR4/3
                                        BETA=1
                                        GOTO 10100
                                ENDIF
                                BETA=1
                                DHM=DHM-STAR4
                                GOTO 10100
                        ENDIF
                        IF(DDELT.LT.VALUE)THEN
                                IF(BETA.EQ.1)THEN
                                        DHM=DHM+STAR4/2
                                        BETA=0
                                        GOTO 10100
                                ENDIF
                                DHM=DHM+STAR4
                                BETA=0
                                GOTO 10100
                        ENDIF
10200                   CONTINUE
                        HM(J)=DHM
                        HI(J)=DHI
                        EC(J)=DEC
                        T(J)=DT
                        DELT(J)=DDELT
        STRESSI(J)=AO/((1-EC(J))*A)*(SIGCSTR-YOUNGC*(ECSTR-EC(J)))
                        STRAINI(J)=STRESSI(J)/(E/1E6)
      V1(J)=VO-(STRESSI(J)*1E6)/(RHOST*CST)-(2*STRESSJJN*1E6)/
     +          (RHOST*CST)-(2*STRESSJJNNN*1E6)/(RHOST*CST)-(2*STRESSJJNNNN*1E6)/
     +          (RHOST*CST)-(2*STRESSJJNNNN*1E6)/(RHOST*CST)-(2*STRESSJJNIV*1E6)/
     +          (RHOST*CST)-(2*STRESSJJNV*1E6)/(RHOST*CST)-(2*STRESSJJNVI*1E6)/
     +          (RHOST*CST)-(2*STRESSJJNVII*1E6)/(RHOST*CST)-(2*STRESSJJNVIII*1E6)
     +          /(RHOST*CST)-(2*STRESSJJNIX*1E6)/(RHOST*CST)-(2*STRESSJJNX*1E6)/
     +          (RHOST*CST)
                        V2(J)=(STRESSI(J)*1E6)/(RHO*C)
                        TMS(J)=T(J)*1E6
                        STRNRT(J)=(V1(J)-V2(J))/HOM
C
C    THE CALCULATED STRNRT(J) ABOVE ASSUMES UNLOADING IS OCCURING. IF THE
C    STRAIN RATE IS POSITIVE, STRNRT(J) IS NOT VALID.  THEREFORE, THE PROGRAM
C    LETS TIME ADVANCE AND HOLDS THE STRESS AND STRAIN CONSTANT.
C
                        IF(STRNRT(J).GT.0.0)THEN
                                STRESSI(J)=STRESSI(J-1)
                                STRAINI(J)=STRAINI(J-1)
                                HM(J)=HM(J-1)
                                HI(J)=HI(J-1)
                                EC(J)=EC(J-1)
      V1(J)=VO-(STRESSI(J)*1E6)/(RHOST*CST)-(2*STRESSJJN*1E6)/
     +          (RHOST*CST)-(2*STRESSJJNNN*1E6)/(RHOST*CST)-(2*STRESSJJNNNN*1E6)/
     +          (RHOST*CST)-(2*STRESSJJNNNN*1E6)/(RHOST*CST)-(2*STRESSJJNIV*1E6)/
     +          (RHOST*CST)-(2*STRESSJJNV*1E6)/(RHOST*CST)-(2*STRESSJJNVI*1E6)/
     +          (RHOST*CST)-(2*STRESSJJNVII*1E6)/(RHOST*CST)-(2*STRESSJJNVIII*1E6)
     +          /(RHOST*CST)-(2*STRESSJJNIX*1E6)/(RHOST*CST)-(2*STRESSJJNX*1E6)/
     +          (RHOST*CST)
                                V2(J)=(STRESSI(J)*1E6)/(RHO*C)
                                STRNRT(J)=(V1(J)-V2(J))/HOM
C
C    DOES NOT WRITE THE ADVANCE, JUST KEEPS TRACK OF IT
C
                                GO TO 10800
                        ENDIF
10201                   PRINT *,  J,EC(J),TMS(J)
                        IF(STRESSI(J).LT.0.0)THEN
                                STRESSI(J)=0.0
        WRITE(7,10700,ERR=999)HM(J),HI(J),EC(J),T(J),DELT(J),
     +          STRAINI(J),STRESSI(J),TMS(J),STRNRT(J),V1(J),
```

```
      +          V2(J)
                                            GO TO 20000
                        ENDIF
        WRITE(7,10700,ERR=999)HM(J),HI(J),EC(J),T(J),DELT(J),
      +          STRAINI(J),STRESSI(J),TMS(J),STRNRT(J),V1(J),
      +          V2(J)
10700    FORMAT(11(F15.8,1X))
10800                   IF(J.EQ.(COUNT*N))THEN
                                PRINT*, J,STRNRT(J),TMS(J)
                                IF(COUNT.EQ.2)NN=J
                                IF(COUNT.EQ.3)NNN=J
                                IF(COUNT.EQ.4)NIV=J
                                IF(COUNT.EQ.5)NV=J
                                IF(COUNT.EQ.6)NVI=J
                                IF(COUNT.EQ.7)NVII=J
                                IF(COUNT.EQ.8)NVIII=J
                                IF(COUNT.EQ.9)NIX=J
                                IF(COUNT.EQ.10)NX=J
                                COUNT=COUNT+1
                        ENDIF
10050            CONTINUE
10000 CONTINUE
20000 CLOSE(UNIT=7)
      CLOSE(UNIT=8)
      CLOSE(UNIT=9)
      CLOSE(UNIT=10)
      STOP
      END
```

APPENDIX B

PULSE SHAPING MODEL EVALUATION EXPERIMENTS

A total of 32 SHPB experiments were conducted with hard (HRB = 45) and annealed C11000 copper pulse shapers to study the accuracy of the pulse shaping model and resistance functions developed in Chapter 5. These experiments were conducted using 12.7-mm-diameter VascoMax C-350 maraging steel (HRC = 58) striker and incident bars. We varied striker bar lengths (50.8 and 152.4 mm), nominal striking velocities (8.5 and 17.5 m/s), pulse shaper diameters (3.2 and 4.8 mm), and pulse shaper thicknesses (1.6 and 0.8 mm) in order to exercise our model over a variety of loading conditions.

Tabulated results from the experiments and model predictions are presented for the hardened and annealed (C11000) coppers in Tables B.1 and B.2, respectively. For each experiment, the pre- and post-test dimensions of the pulse shapers were measured and used to calculate the final engineering strain in the pulse shaper and also validate our model assumption that the pulse shaper material is nearly incompressible [see eq (5.1)]. The peak incident bar stress was from the peak axial strain measured by the incident bar strain gages. Knowing the peak stress in the incident bar and final pulse shaper diameter, eq (5.5) was then rearranged to calculate the peak true pulse shaper stress. Model predictions of the pulse shaper strain given by eqs (5.11), (5.20), (5.29), and (5.34) were applied to eq (5.3), (5.2), (5.6), and (5.5) to calculate the diameter and thickness of the pulse shaper, the true stress in the pulse shaper, and the incident bar stress, respectively. Tables B.1 and B.2 show that model predictions of the final pulse shaper dimensions and peak incident bar and pulse shaper stresses are in good agreement with the experimental measurements.

Figures B.1 – B.16 show incident bar stress data and model prediction comparisons for the tests described in Tables B.1 and B.2. Part (a) and (b) of each figure describes the respective response of a hardened and annealed (C11000) copper pulse shaper tested under nominally identical input conditions. As we discussed earlier in Chapter 5, a common feature for the hardened copper data is a well-defined knee found early into the loading of the pulse shaper. The knee is created when the hardened copper is loaded beyond its elastic limit and begins to flow plastically. Since annealed copper has a much smaller yield strength than that of the hardened copper, the annealed copper knee is sometimes more difficult to distinguish. The incident stress pulse model predictions agree well with measurements and can therefore be used as a design tool to help select the experimental parameters necessary to produce valid SHPB experiments for brittle materials.

Table B.1 Comparison of post-test pulse shaper data and model dimensions and incident and pulse shaper peak stresses for hardened (C11000) copper

Striking Velocity (m/s)	Striker Length (mm)	Initial Pulse Diameter (mm)	Initial Pulse Thickness (mm)	Final Pulse Diameter* (mm)	Final Pulse Thickness* (mm)	Incompressible Ratio (a_0h_0/ah) (%)	Final Axial Engineering Strain* (%)	Peak Incident Stress* (MPa)	Peak True Pulse Shaper Stress* (MPa)
8.58	50.8	3.20	1.57	3.71/ 3.70	1.17/1.18	99.7%	25.5/ 25.2	41.9/ 42.5	482.8/ 493.2
17.61	50.8	3.18	1.57	5.42/ 5.32	0.54/ 0.56	99.0%	65.3/ 64.3	116.1/ 116.1	629.0/ 653.6
9.04	152.4	3.18	1.55	4.68/ 4.63	0.73/ 0.73	97.5%	52.8/ 52.9	78.3/ 77.0	567.3/ 572.2
17.49	152.4	3.21	1.57	7.04/ 6.92	0.34/ 0.34	97.3%	78.6/ 78.3	279.3/ 275.2	897.2/ 915.2
8.52	50.8	3.21	0.79	4.16/ 4.12	0.48/ 0.48	98.8%	39.7/ 9.2	59.7/ 55.8	548.8/ 523.8
17.49	50.8	3.21	0.80	6.32/ 6.41	0.22/ 0.20	95.7%	73.1/ 4.7	186.5/ 208.5	742.6/ 806.9
8.79	152.4	3.16	0.78	4.98/ 5.33	0.32/ 0.28	99.0%	59.3/ 4.8	124.4/ 117.6	797.4/ 658.8
17.53	152.4	3.25	0.80	7.67/ 7.41	0.15/ 0.15	97.1%	81.4/ 80.7	339.5/ 349.3	917.6/ 1012.4
8.70	50.8	4.78	1.59	5.03/ 5.06	1.44/ 1.42	99.9%	9.7/ 10.9	71.8/ 73.6	450.3/ 456.5
17.81	50.8	4.76	1.59	6.03/ 6.08	1.02/ 0.98	97.3%	36.0/ 38.7	126.0/ 121.3	550.0/ 522.5
8.66	152.4	4.74	1.58	5.46/ 5.44	1.21/ 1.20	98.1%	23.2/ 24.1	89.6/ 91.5	478.0/ 490.9
17.50	152.4	4.74	1.59	7.41/ 7.57	0.66/ 0.63	98.8%	58.5/ 60.7	230.6/ 223.9	667.2/ 621.4
8.69	50.8	4.81	0.77	5.42/ 5.34	0.64/ 0.63	95.7%	17.8/ 18.9	80.7/ 86.0	436.2/ 479.7
17.76	50.8	4.78	0.78	6.92/ 7.08	0.38/ 0.36	97.6%	51.1/ 54.5	184.5/ 183.3	612.1/ 580.9
8.68	152.4	4.75	0.78	5.80/ 5.95	0.54/ 0.50	97.4%	31.1/ 36.3	121.1/ 115.2	572.7/ 517.1
17.52	152.4	4.78	0.81	7.87/ 8.65	0.30/ 0.25	99.2%	62.9/ 69.4	326.7/ 335.3	838.0/ 712.5

* Experimental data/ model prediction

Table **B.2** Comparison of post-test pulse shaper data and model dimensions and incident and pulse shaper peak stresses for annealed (C11000) copper

Striking Velocity (m/s)	Striker Length (mm)	Initial Pulse Diameter (mm)	Initial Pulse Thickness (mm)	Final Pulse Diameter* (mm)	Final Pulse Thickness* (mm)	Incompressible Ratio ($a_o h_o/ah$) (%)	Final Axial Engineering Strain* (%)	Peak Incident Stress* (MPa)	Peak True Pulse Shaper Stress* (MPa)
8.55	50.8	3.18	1.57	3.93/ 3.90	1.04/ 1.05	98.5%	33.9/ 33.5	43.6/ 42.9	447.9/ 449.8
17.68	50.8	3.19	1.60	5.57/ 5.49	0.53/ 0.54	98.5%	66.7/ 66.3	130.5/ 129.4	669.3/ 682.5
8.72	152.4	3.19	1.61	4.78/ 4.73	0.73/ 0.73	97.3%	54.3/ 54.4	77.9/ 79.5	541.1/ 565.0
17.49	152.4	3.20	1.59	7.11/ 6.86	0.33/ 0.35	98.9%	79.5/ 78.2	280.2/ 281.5	881.0/ 951.2
8.16	50.8	3.18	0.77	4.20/ 4.17	0.46/ 0.45	96.8%	41.0/ 41.8	59.4/ 61.6	535.3/ 564.0
17.63	50.8	3.18	0.80	.21/ 6.09	0.21/ 0.22	98.5%	73.4/ 72.7	203.4/ 219.8	838.7/ 942.4
8.67	152.4	3.19	0.80	.03/ 5.13	0.33/ 0.31	99.1%	59.4/ 61.0	124.1/ 120.7	779.2/ 729.2
17.57	152.4	3.20	0.81	7.34/ 6.92	0.16/ 0.17	98.9%	80.8/ 78.7	347.1/ 350.4	1024.5/ 1165.2
8.31	50.8	4.77	1.57	5.26/ 5.23	1.34/ 1.31	96.6%	15.0/ 16.9	59.3/ 61.8	340.0/ 358.7
17.61	50.8	4.79	1.58	6.41/ 6.38	0.91/ 0.89	96.7%	42.4/ 43.8	131.2/ 128.3	507.4/ 500.5
8.63	152.4	4.77	1.57	5.81/ 5.79	1.08/ 1.07	97.9%	31.2/ 32.0	95.3/ 93.1	448.6/ 442.11
17.52	152.4	4.81	1.62	7.60/ 7.77	0.66/ 0.62	98.8%	59.4/ 61.7	240.7/ 238.6	663.8/ 628.4
8.68	50.8	4.76	0.76	5.55/ 5.51	0.58/ 0.57	95.9%	23.3/ 25.2	82.6/ 87.4	427.3/ 458.1
17.74	50.8	4.80	0.82	6.94/ 7.00	0.40/ 0.38	97.0%	50.8/ 53.1	191.5/ 200.1	631.5/ 648.8
8.51	152.4	4.78	0.76	6.01/ 6.10	0.48/ 0.47	99.8%	36.7/ 38.7	125.3/ 127.5	552.4/ 545.6
17.48	152.4	4.78	0.78	8.15/ 8.22	0.27/ 0.26	99.8%	65.6/ 66.3	326.6/ 343.7	781.3/ 808.6

* Experimental data/ model prediction
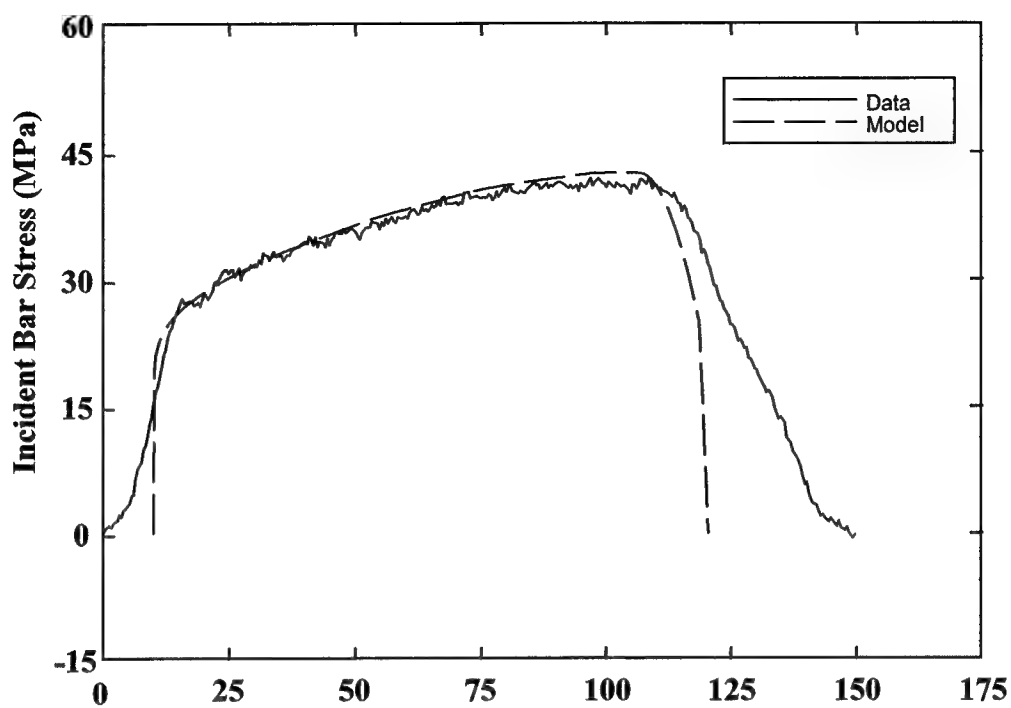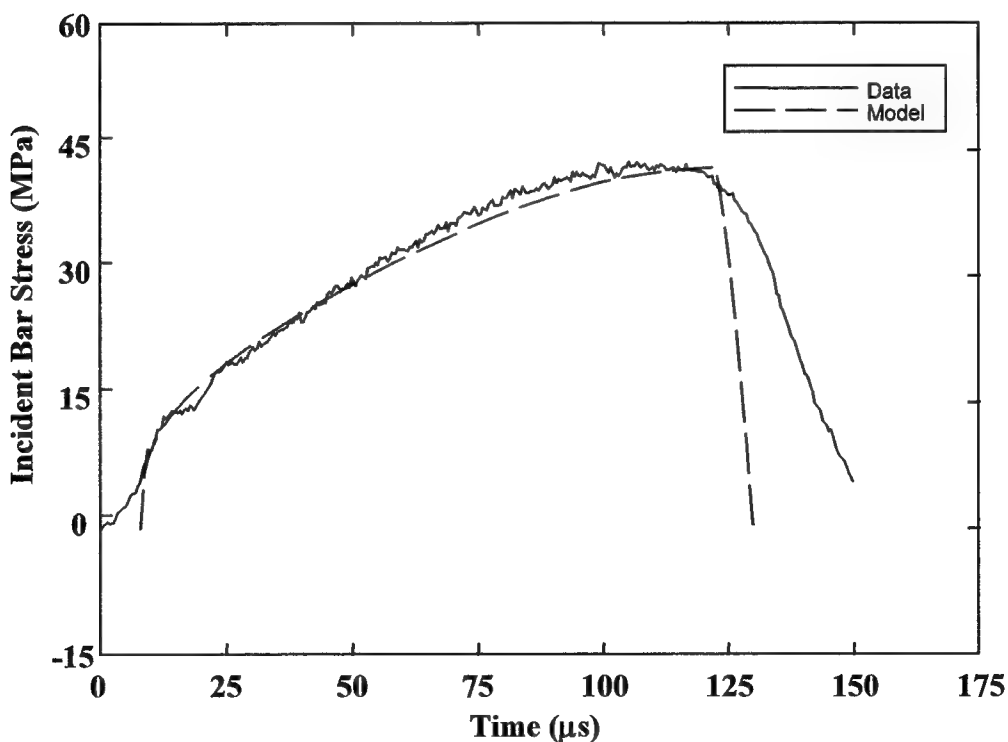
Figure B.1 Data and model predictions for nominal 3.2-mm-diameter by 1.6-mm-thick
(a) hard and (b) annealed C11000 copper pulse shaper impacted by a 50.8-mm-long
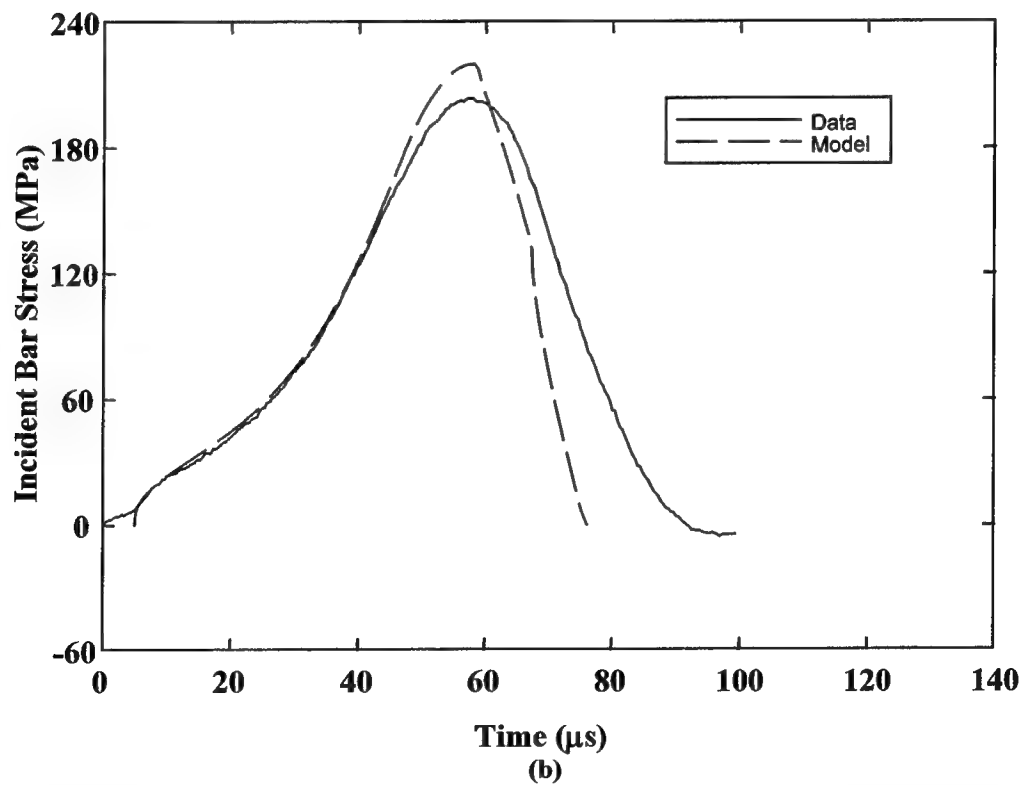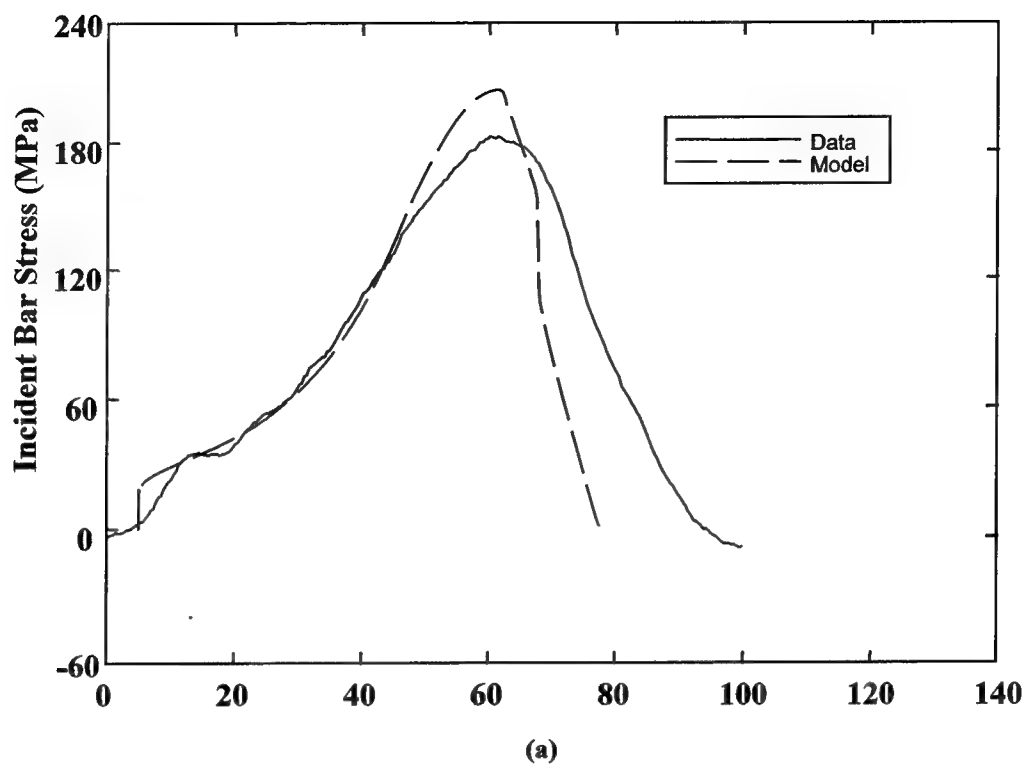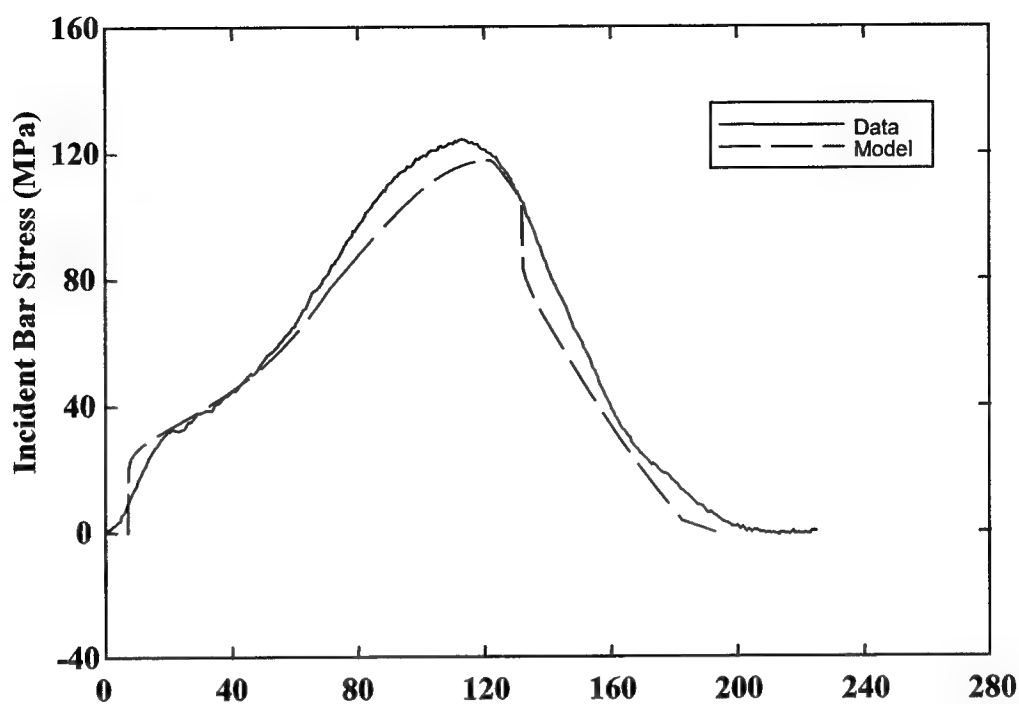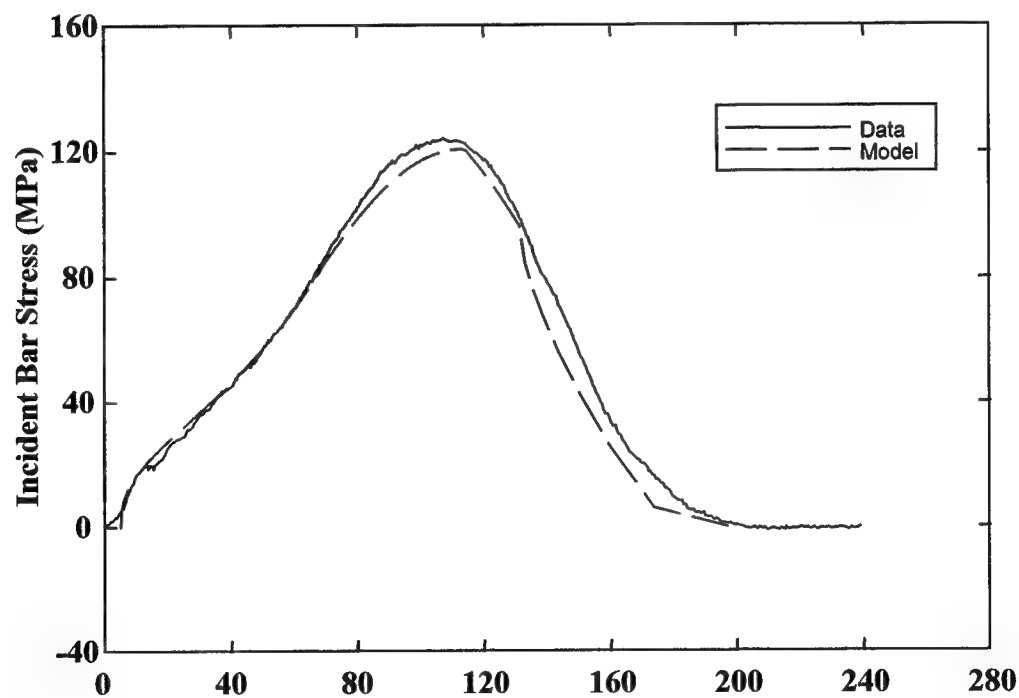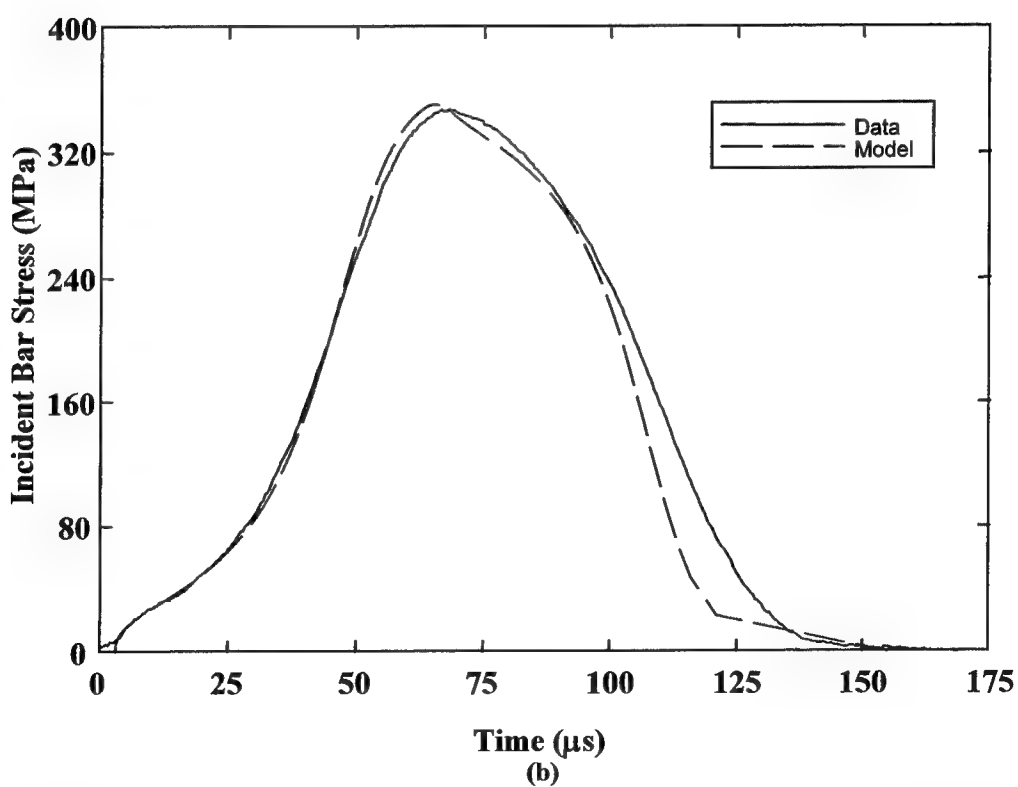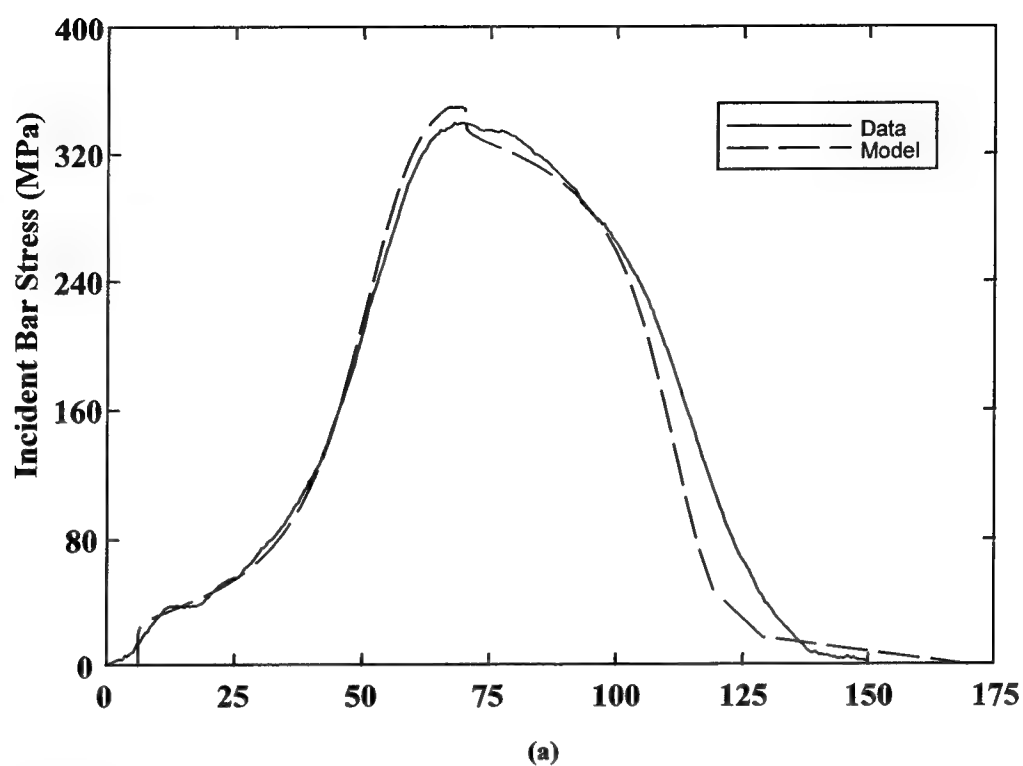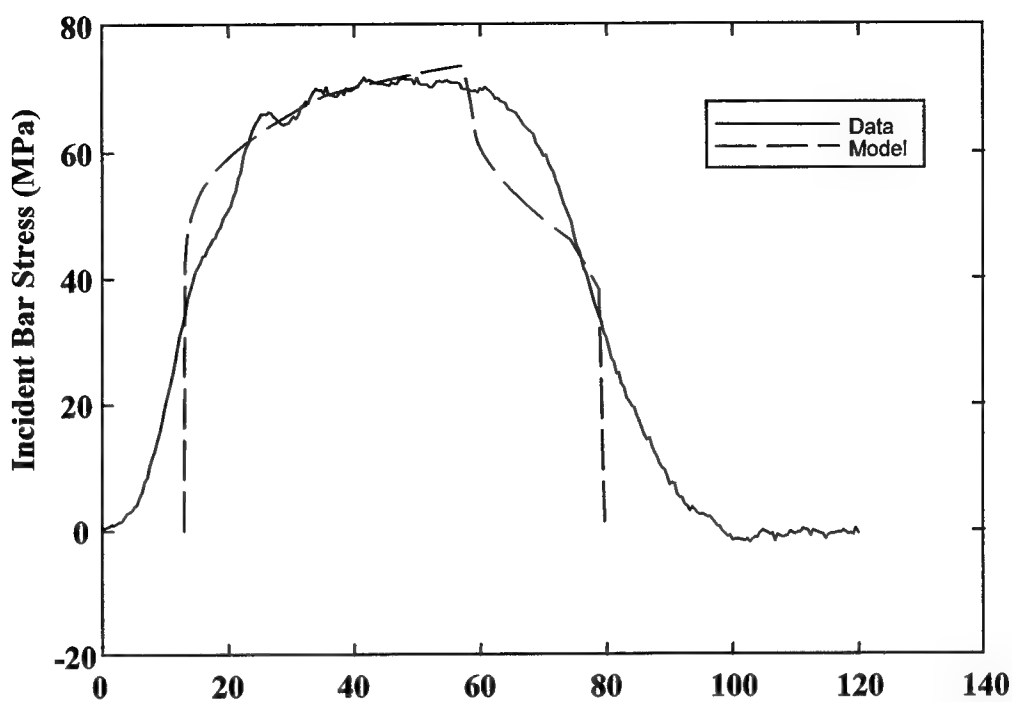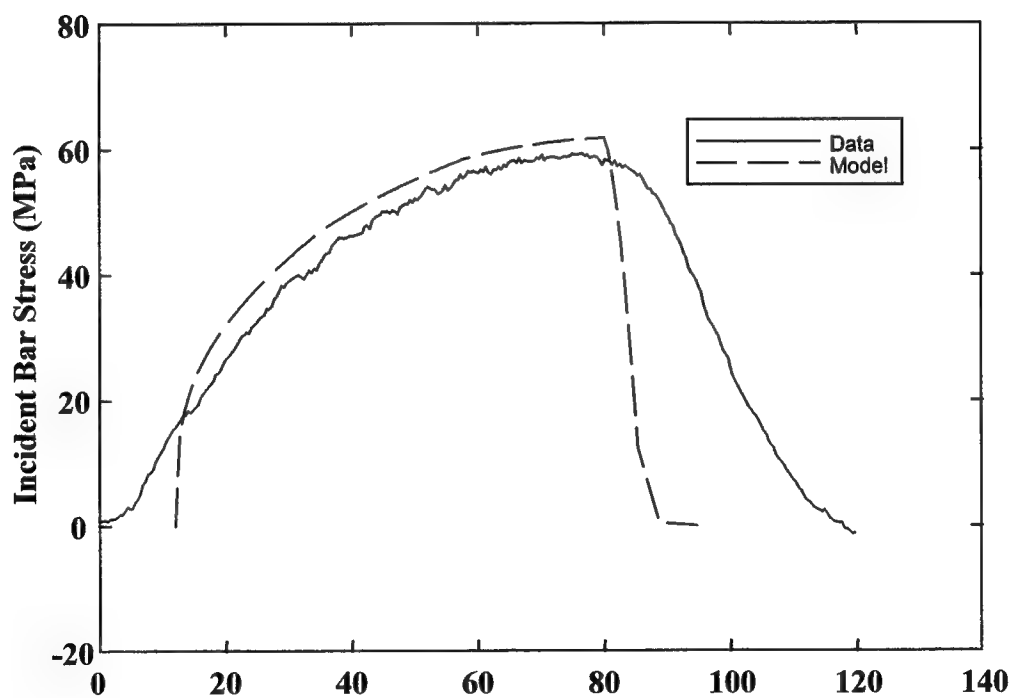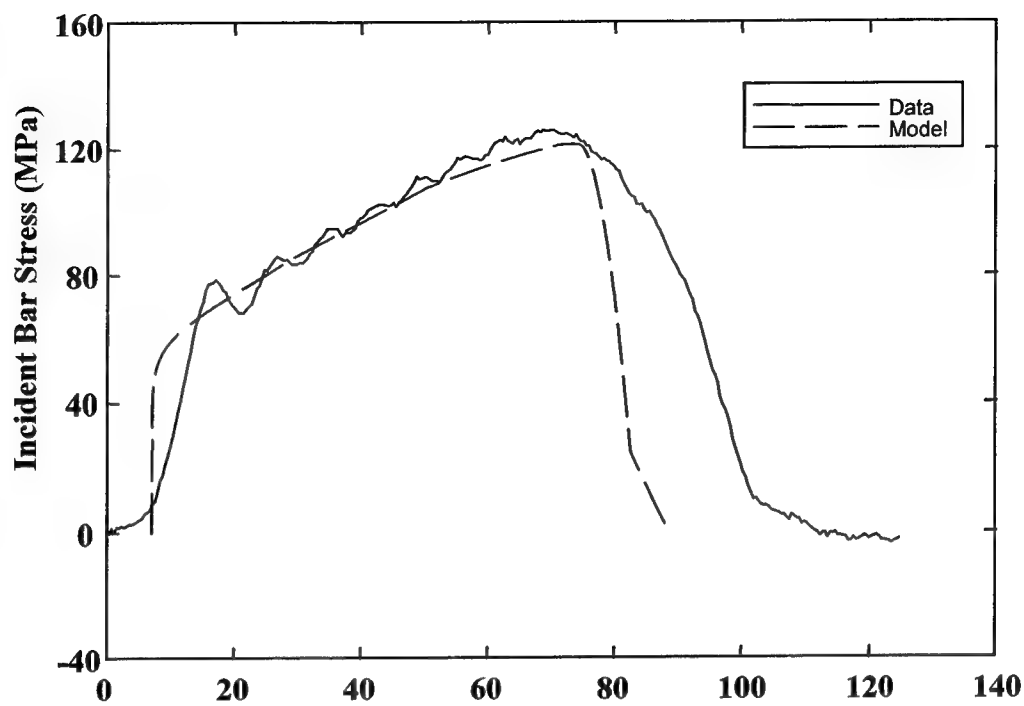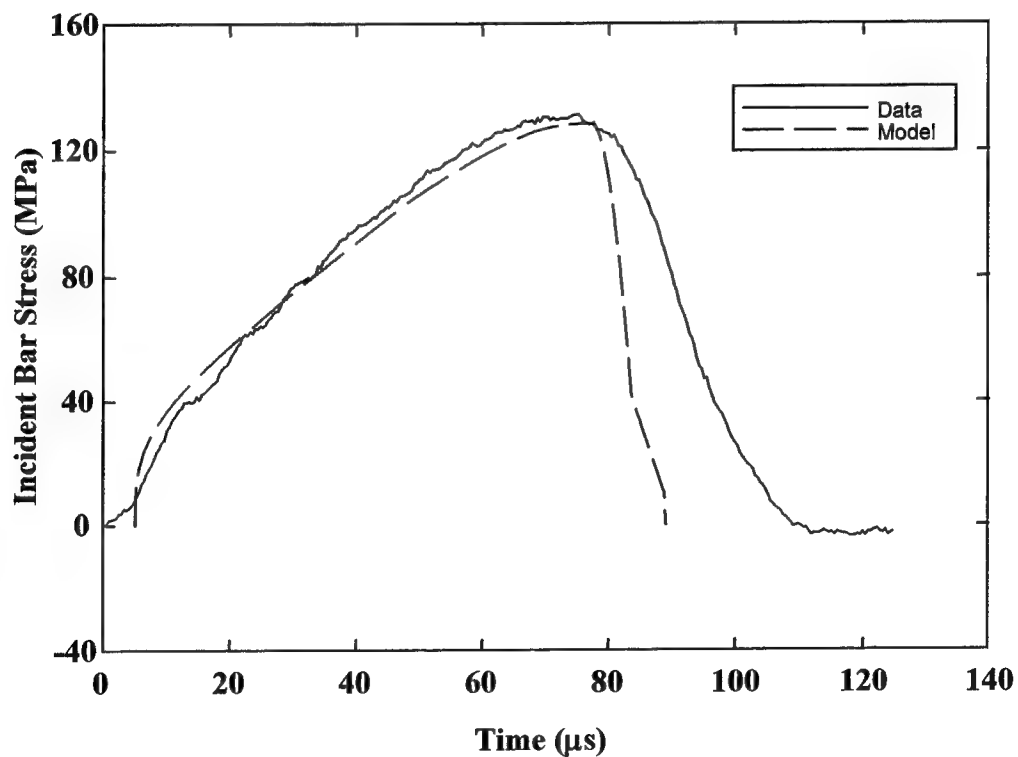striker at a nominal velocity of 8.6 m/s
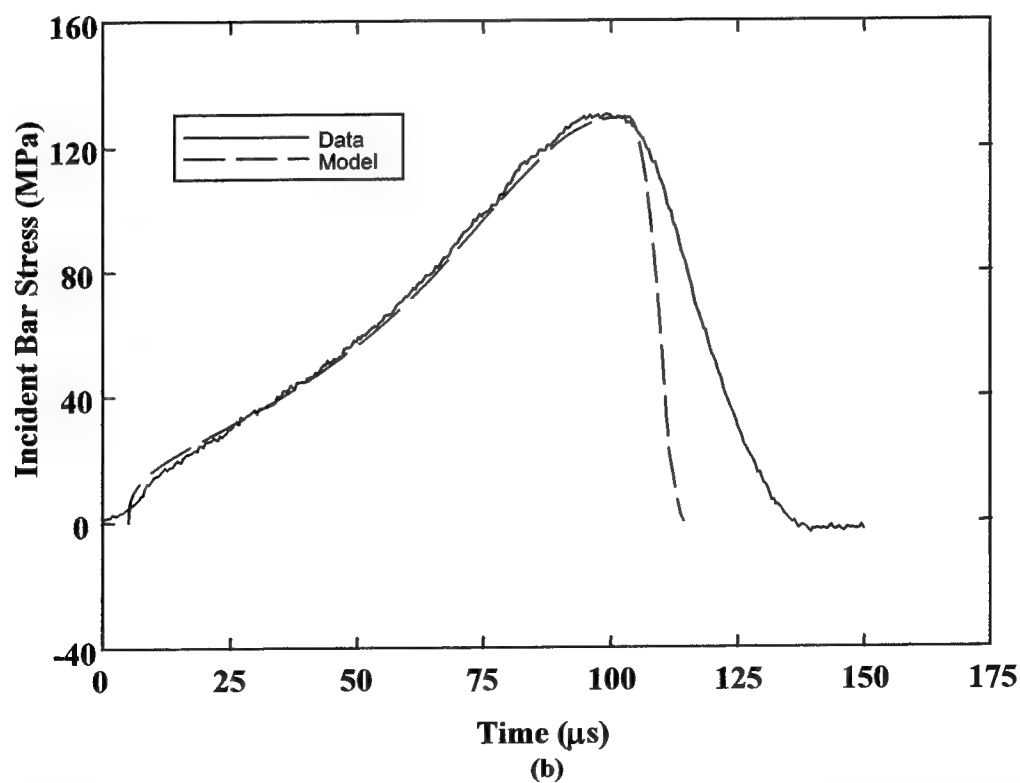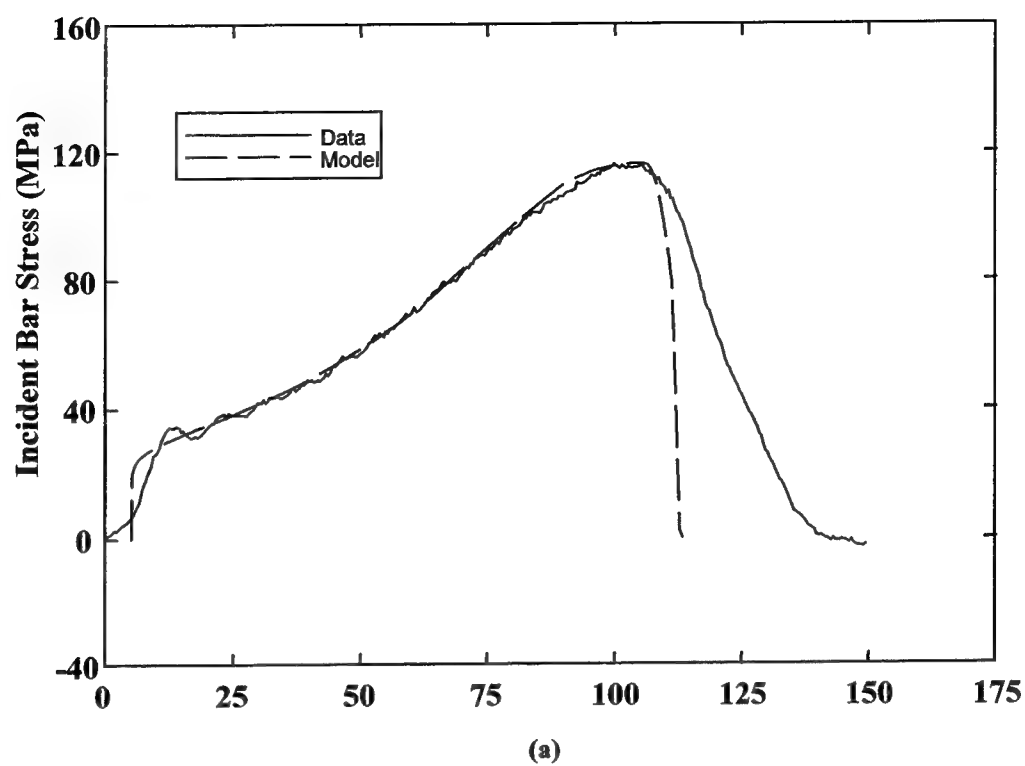
Figure B.2 Data and model predictions for nominal 3.2-mm-diameter by 1.6-mm-thick
(a) hard and (b) annealed C11000 copper pulse shaper impacted by a 50.8-mm-long
striker at a nominal velocity of 17.6 m/s
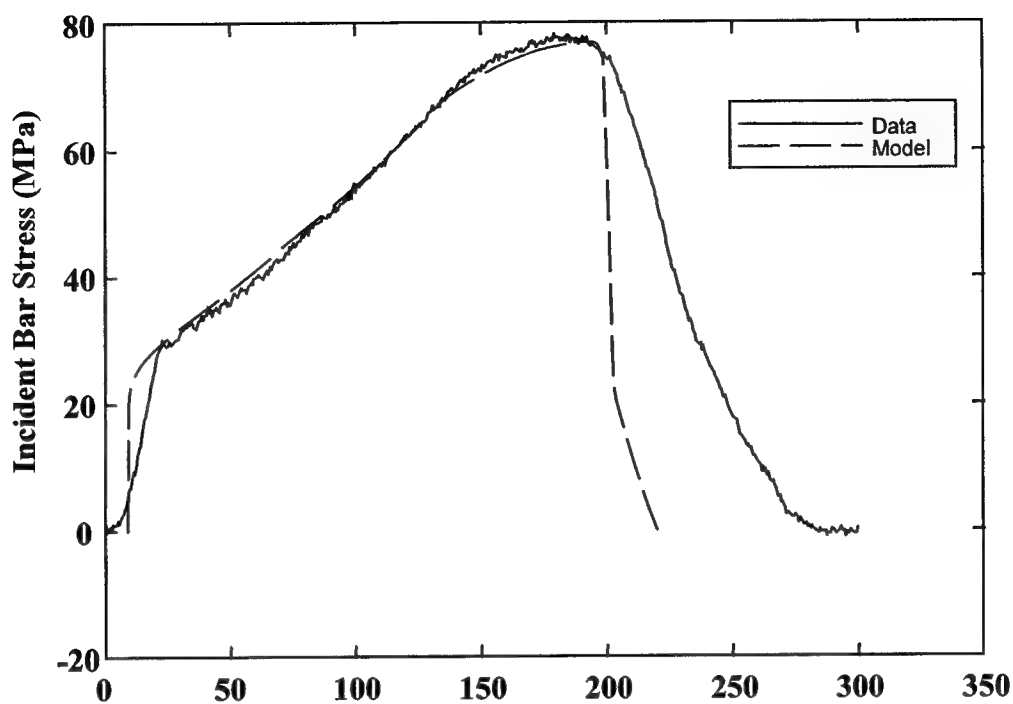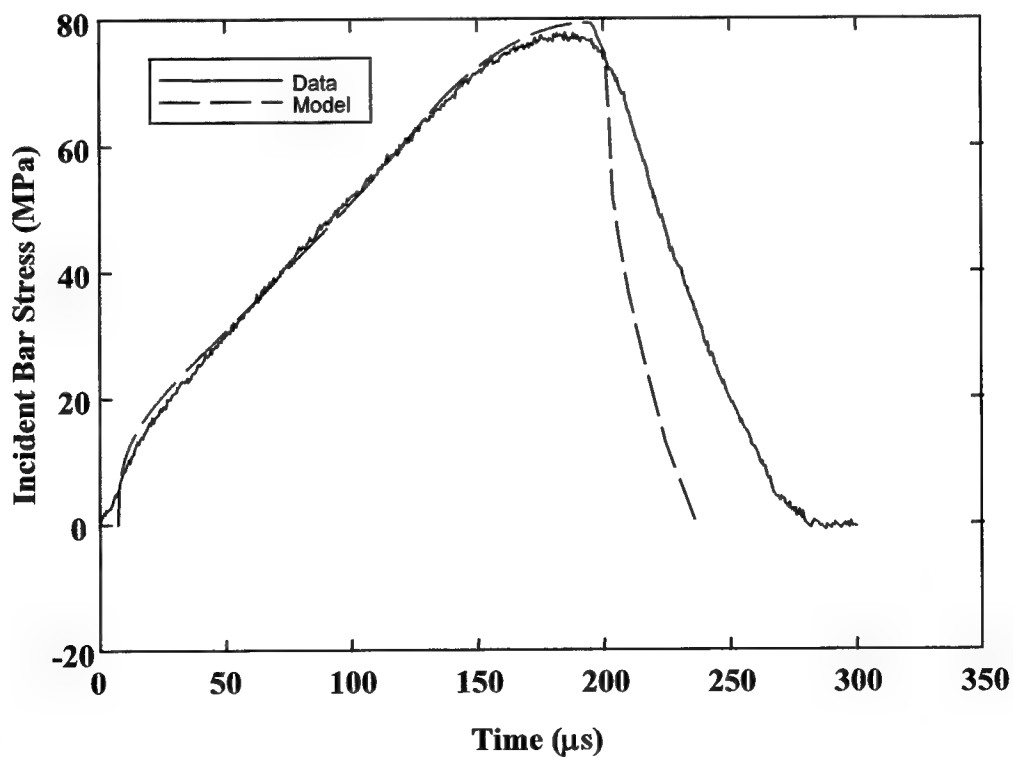
Figure B.3 Data and model predictions for nominal 3.2-mm-diameter by 1.6-mm-thick
(a) hard and (b) annealed C11000 copper pulse shaper impacted by a 152.4-mm-long
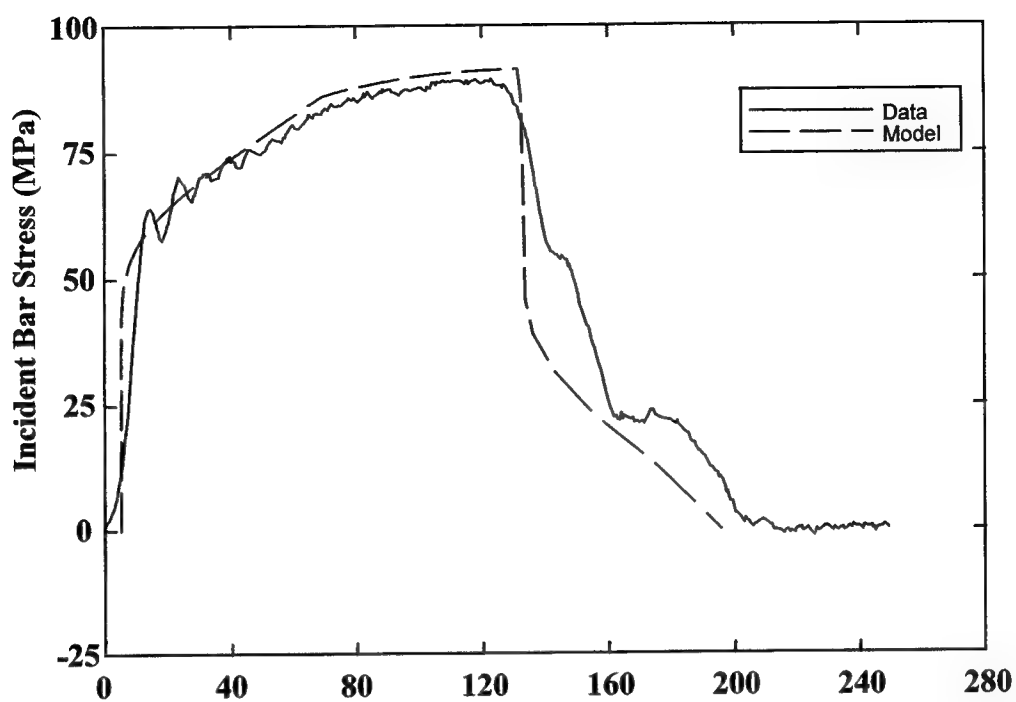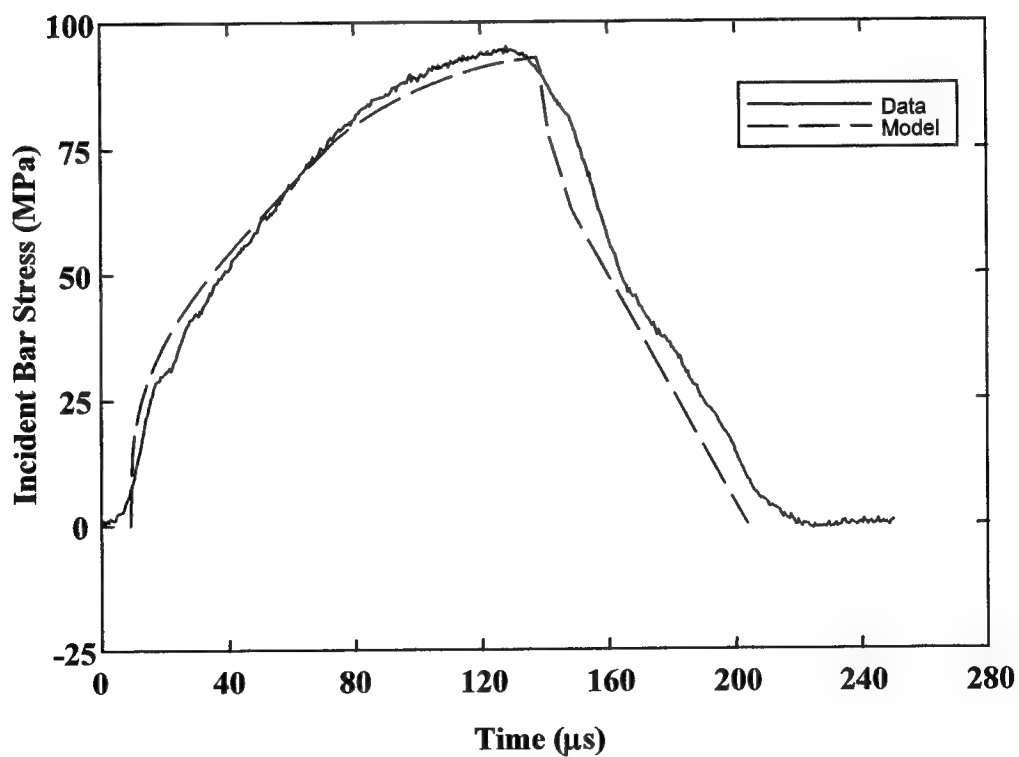striker at a nominal velocity of 8.8 m/s
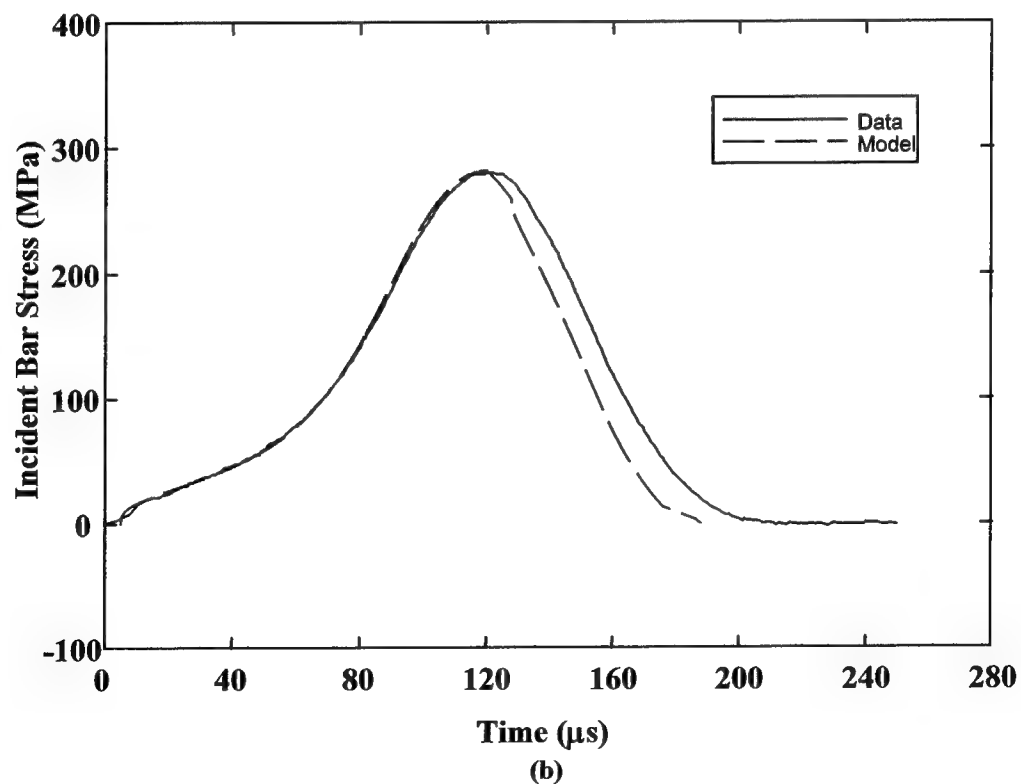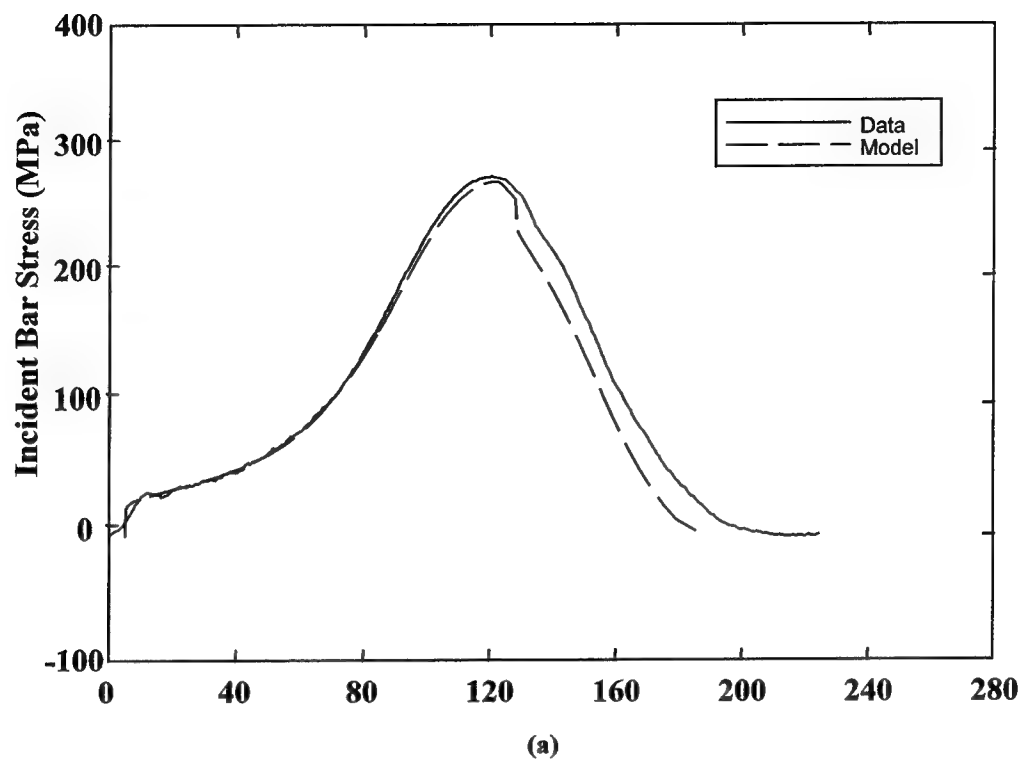
**Figure B.4 Data and model predictions for nominal 3.2-mm-diameter by 1.6-mm-thick
(a) hard and (b) annealed C11000 copper pulse shaper impacted by a 152.4-mm-long
striker at a nominal velocity of 17.5 m/s**
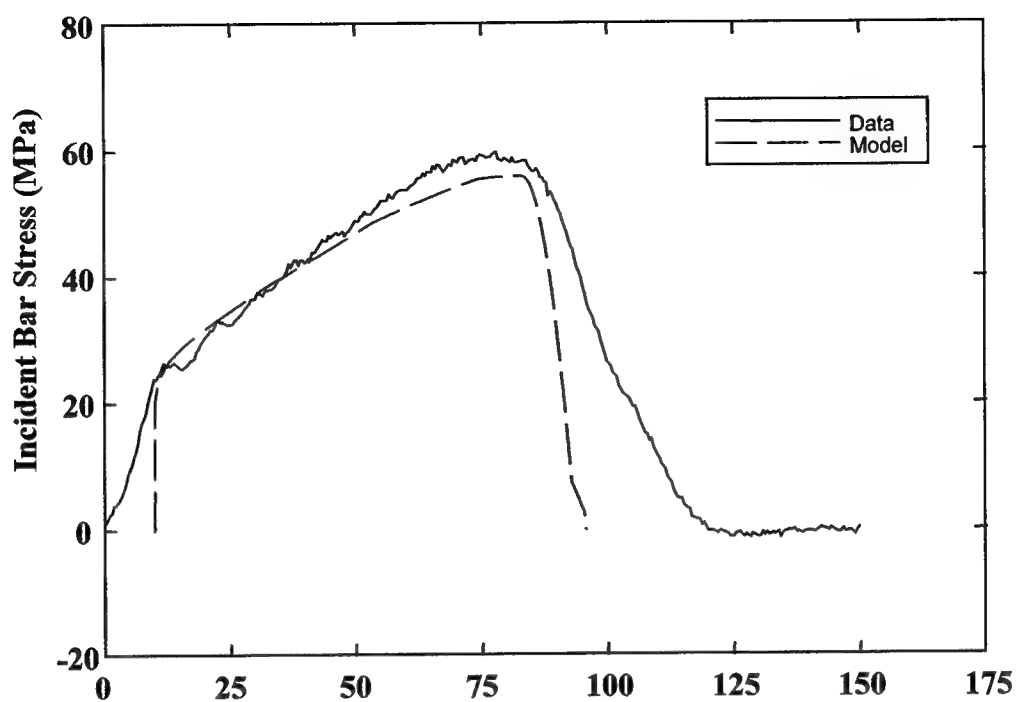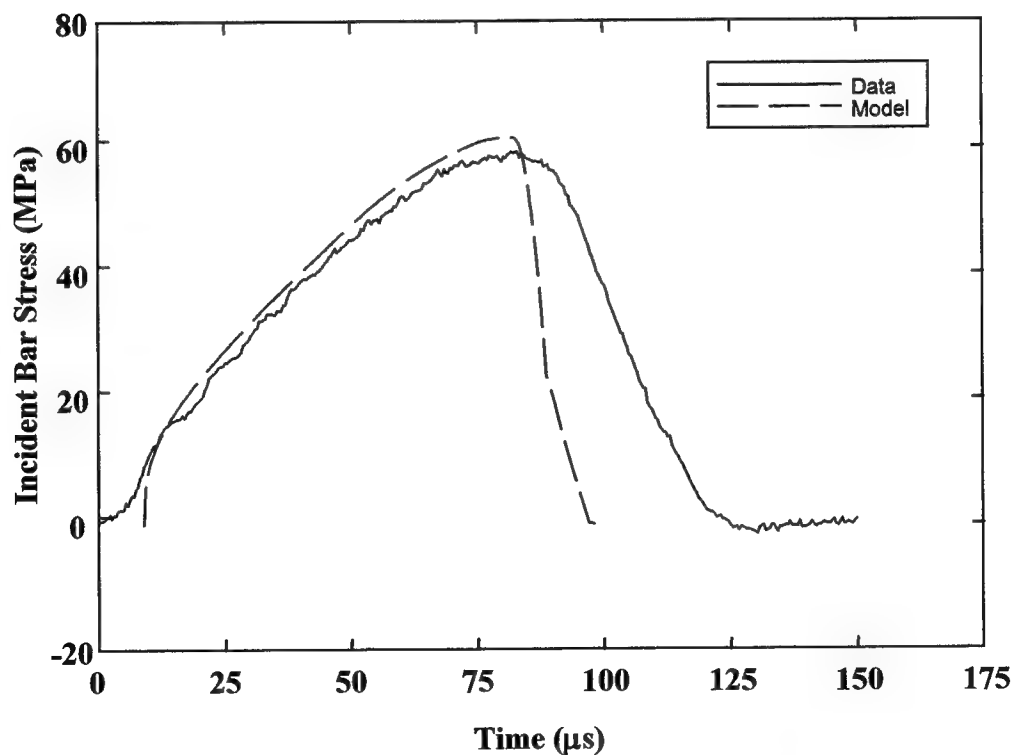
Figure B.5 Data and model predictions for nominal 3.2-mm-diameter by 0.8-mm-thick
(a) hard and (b) annealed C11000 copper pulse shaper impacted by a 50.8-mm-long
striker at a nominal velocity of 8.3 m/s

Figure B.6 Data and model predictions for nominal 3.2-mm-diameter by 0.8-mm-thick
(a) hard and (b) annealed C11000 copper pulse shaper impacted by a 50.8-mm-long
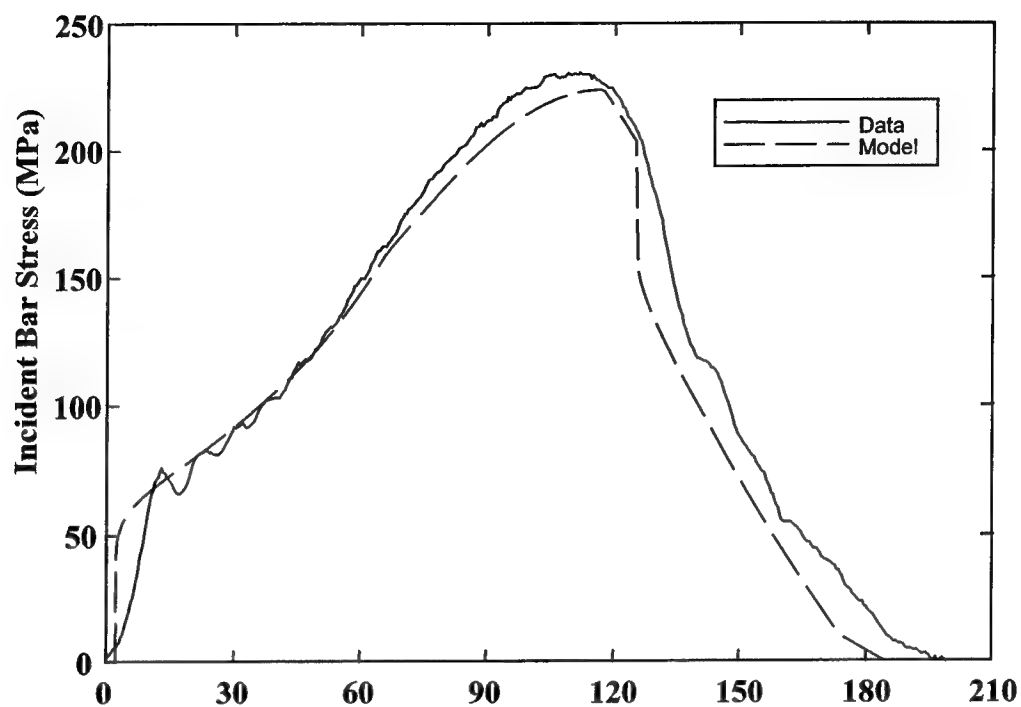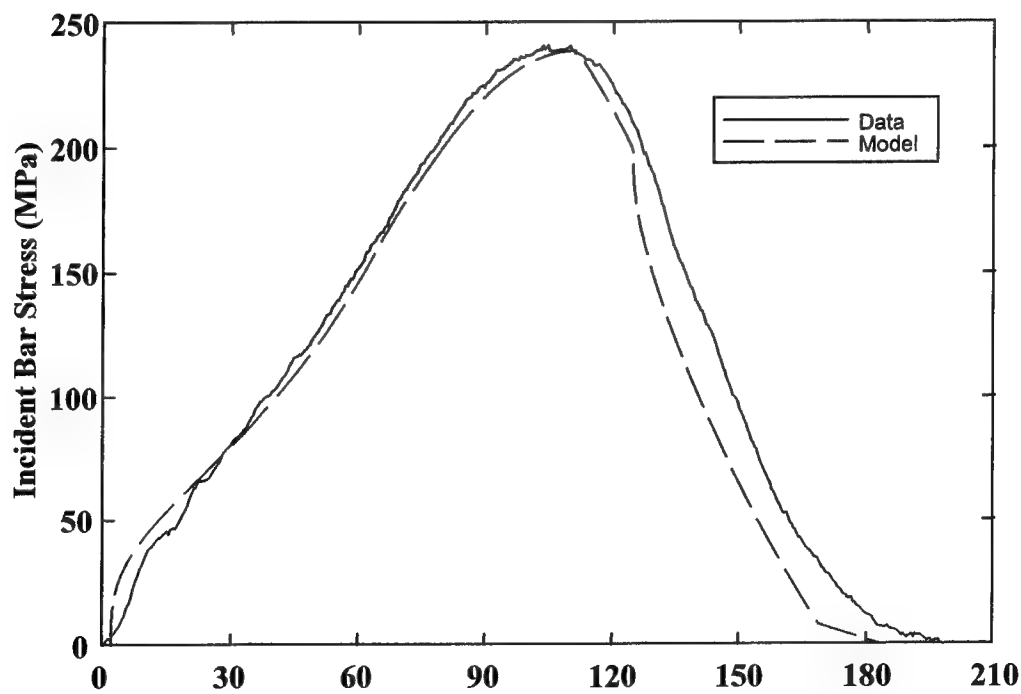striker at a nominal velocity of 17.5 m/s

Figure B.7 Data and model predictions for nominal 3.2-mm-diameter by 0.8-mm-thick
(a) hard and (b) annealed C11000 copper pulse shaper impacted by a 152.4-mm-long
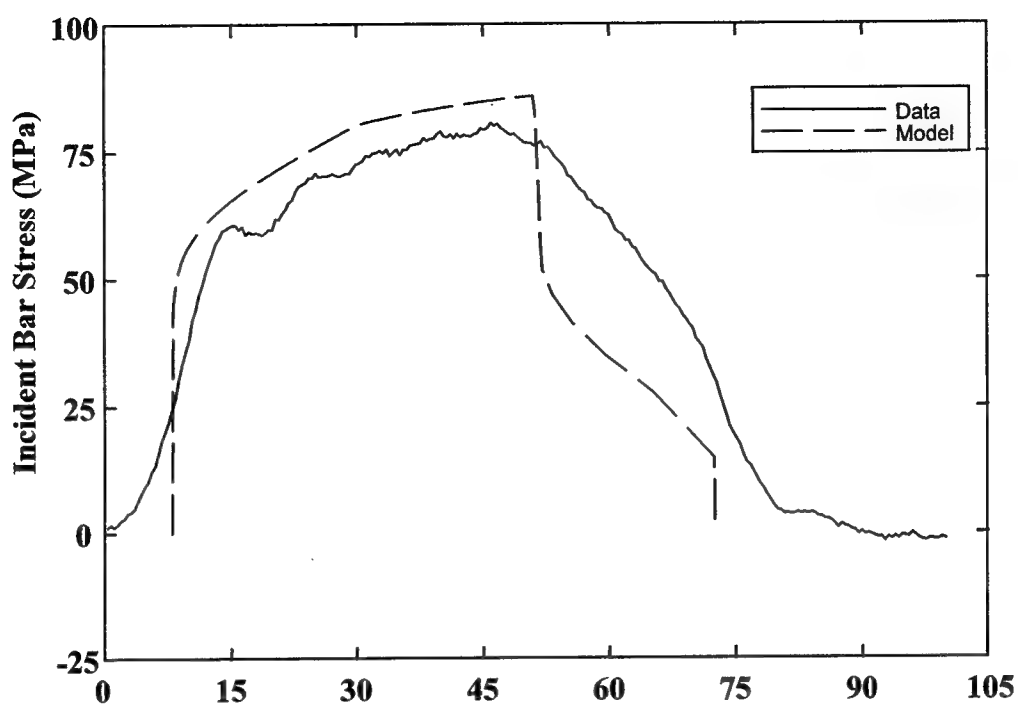striker at a nominal velocity of 8.7 m/s

Figure B.8 Data and model predictions for nominal 3.2-mm-diameter by 0.8-mm-thick
(a) hard and (b) annealed C11000 copper pulse shaper impacted by a 152.4-mm-long
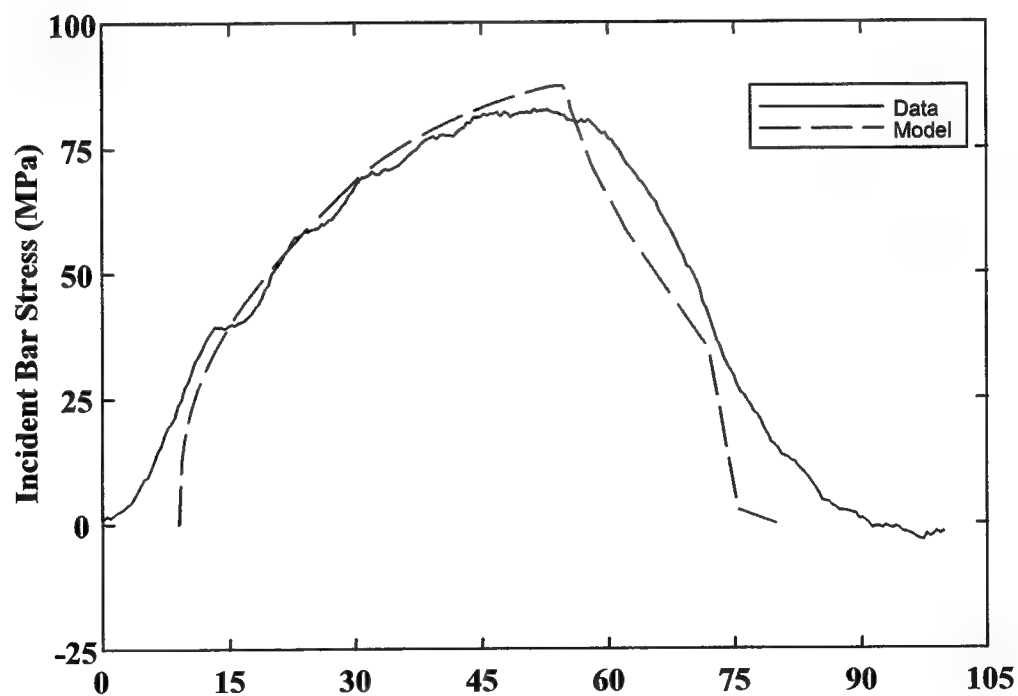striker at a nominal velocity of 17.5 m/s

Figure B.9 Data and model predictions for nominal 4.8-mm-diameter by 1.6-mm-thick
(a) hard and (b) annealed C11000 copper pulse shaper impacted by a 50.8-mm-long
striker at a nominal velocity of 8.5 m/s

Figure B.10 Data and model predictions for nominal 4.8-mm-diameter by 1.6-mm-thick (a) hard and (b) annealed C11000 copper pulse shaper impacted by a 50.8-mm-long striker at a nominal velocity of 17.7 m/s
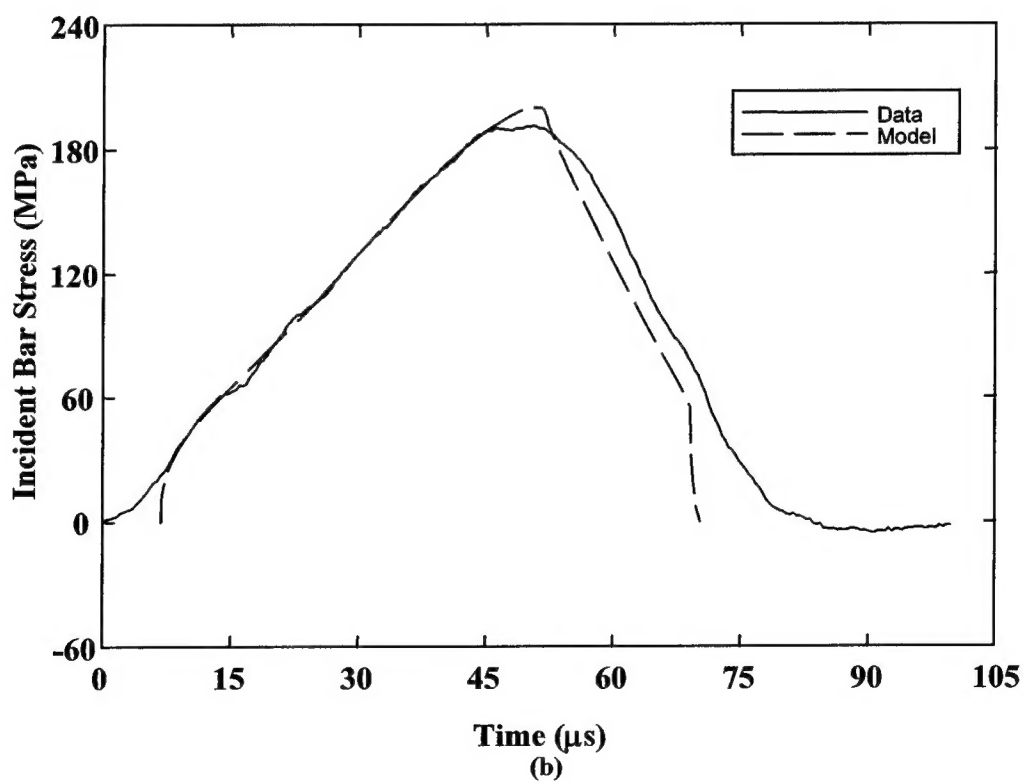
Figure B.11 Data and model predictions for nominal 4.8-mm-diameter by 1.6-mm-thick (a) hard and (b) annealed C11000 copper pulse shaper impacted by a 152.4-mm-long striker at a nominal velocity of 8.6 m/s
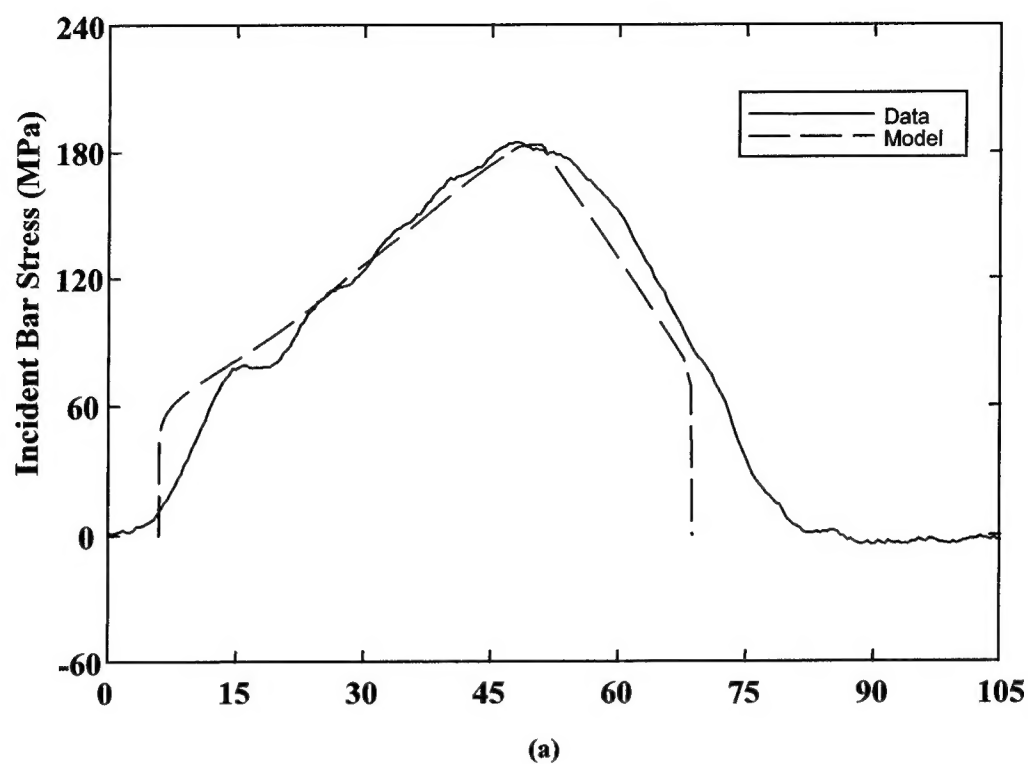
Figure B.12 Data and model predictions for nominal 4.8-mm-diameter by 1.6-mm-thick
(a) hard and (b) annealed C11000 copper pulse shaper impacted by a 152.4-mm-long
striker at a nominal velocity of 17.5 m/s

Figure B.13 Data and model predictions for nominal 4.8-mm-diameter by 0.8-mm-thick
(a) hard and (b) annealed C11000 copper pulse shaper impacted by a 50.8-mm-long
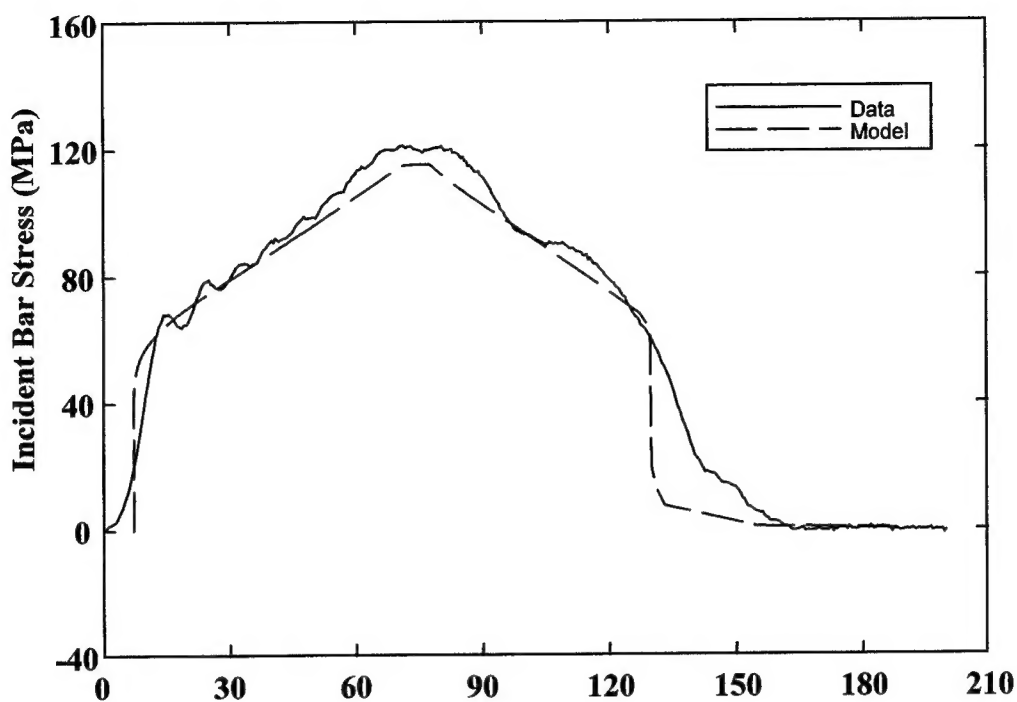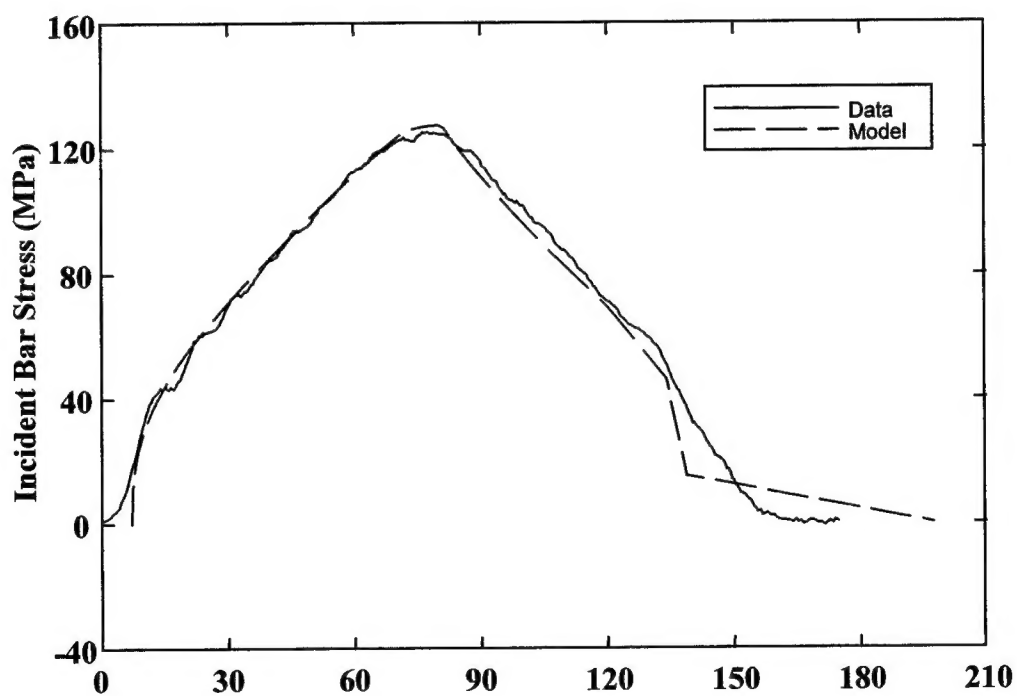striker at a nominal velocity of 8.7 m/s

Figure B.14 Data and model predictions for nominal 4.8-mm-diameter by 0.8-mm-thick
(a) hard and (b) annealed C11000 copper pulse shaper impacted by a 50.8-mm-long
striker at a nominal velocity of 17.7 m/s

Figure B.15 Data and model predictions for nominal 4.8-mm-diameter by 0.8-mm-thick (a) hard and (b) annealed C11000 copper pulse shaper impacted by a 152.4-mm-long striker at a nominal velocity of 8.6 m/s
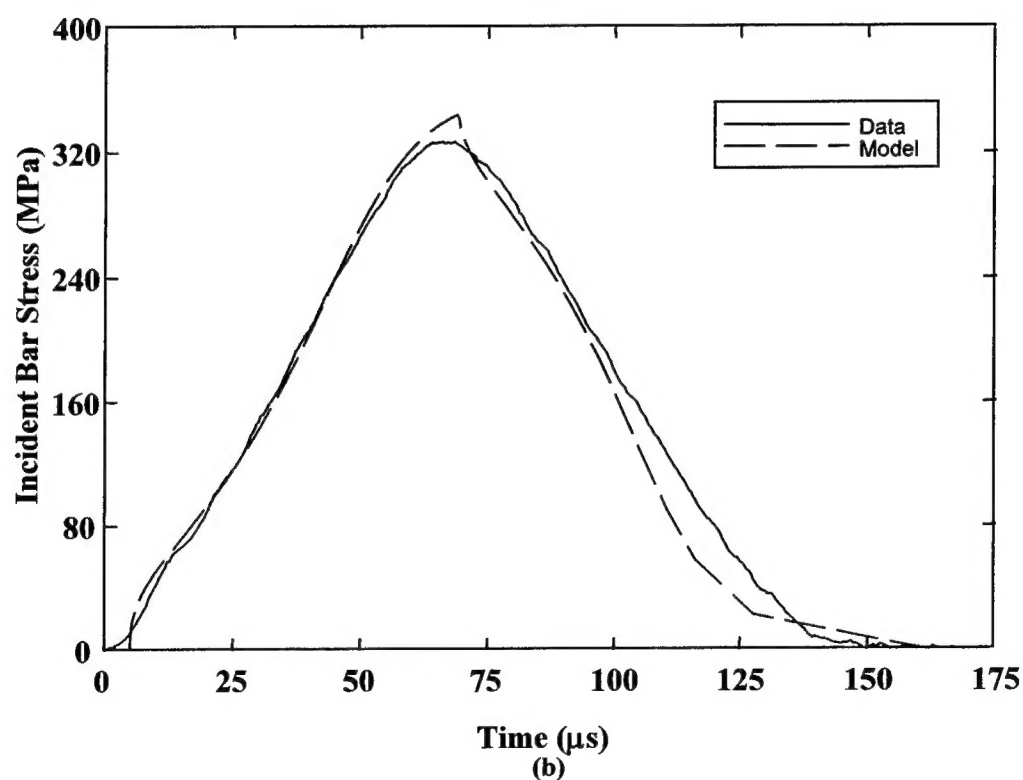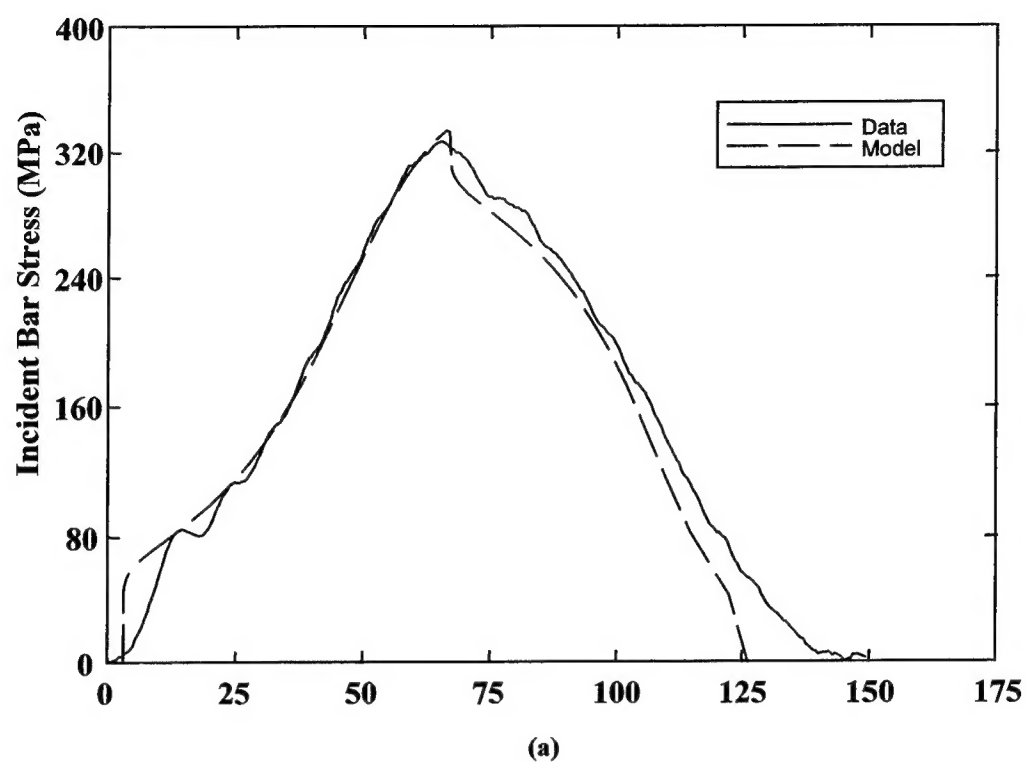
Figure B.16 Data and model predictions for nominal 4.8-mm-diameter by 0.8-mm-thick
(a) hard and (b) annealed C11000 copper pulse shaper impacted by a 152.4-mm-long
striker at a nominal velocity of 17.5 m/s

REPORT DOCUMENTATION PAGE

Public reporting burden for this collection of information is estimated to average 1 hour per response, including the time for reviewing instructions, searching existing data sources, gathering and maintaining the data needed, and completing and reviewing this collection of information. Send comments regarding this burden estimate or any other aspect of this collection of information, including suggestions for reducing this burden to Department of Defense, Washington Headquarters Services, Directorate for Information Operations and Reports (0704-0188), 1215 Jefferson Davis Highway, Suite 1204, Arlington, VA 22202-4302. Respondents should be aware that notwithstanding any other provision of law, no person shall be subject to any penalty for failing to comply with a collection of information if it does not display a currently valid OMB control number. **PLEASE DO NOT RETURN YOUR FORM TO THE ABOVE ADDRESS.**

1. REPORT DATE (DD-MM-YYYY)	2. REPORT TYPE	3. DATES COVERED (From - To)
May 2001	Final Report	

4. TITLE AND SUBTITLE

Dynamic Response of Brittle Materials from Penetration and Split Hopkinson Pressure Bar Experiments

5a. CONTRACT NUMBER

5b. GRANT NUMBER

5c. PROGRAM ELEMENT NUMBER

6. AUTHOR(S)

Danny J. Frew

5d. PROJECT NUMBER

5e. TASK NUMBER

5f. WORK UNIT NUMBER

7. PERFORMING ORGANIZATION NAME(S) AND ADDRESS(ES) AND ADDRESS(ES)

U.S. Army Engineer Research and Development Center
Geotechnical and Structures Laboratory
3909 Halls Ferry Road
Vicksburg, MS 39180-6199;

Sandia National Laboratories
1515 Eubank Blvd., SE
Albuquerque, NM 87185

8. PERFORMING ORGANIZATION REPORT NUMBER

ERDC/GSL TR-01-6

9. SPONSORING / MONITORING AGENCY NAME(S) AND ADDRESS(ES)

10. SPONSOR/MONITOR'S ACRONYM(S)

11. SPONSOR/MONITOR'S REPORT NUMBER(S)

12. DISTRIBUTION / AVAILABILITY STATEMENT

Approved for public release; distribution is unlimited.

13. SUPPLEMENTARY NOTES

14. ABSTRACT

Three sets of penetration experiments into limestone targets were conducted with geometrically similar, steel rod projectiles that had length-to-diameter ratios of 10- and 7.1-, 12.7-, and 25.4-mm-diameters. Results from these penetration experiments and previously developed penetration models suggested that the limestone target exhibited strain-rate sensitivity.

A modified split Hopkinson pressure bar facility (SHPB) was used to study the dynamic material responses of brittle materials, such as limestone, under a state of one-dimensional stress. The conventional split Hopkinson pressure bar apparatus was modified by shaping the incident pulse such that the samples are in dynamic stress equilibrium and have nearly constant strain rate over most of the test duration. A thin disk of annealed or hard C11000 copper is placed on the impact surface of the incident bar in order to shape the incident pulse. An analytical model and data show that a wide variety of incident strain pulses can be produced by varying the geometry of the copper disks and the length and striking velocity of the striker bar. The pulse shaping model predictions are in good agreement with measurements. Thus, this work presents analytical models and experimental techniques that provide procedures to obtain dynamic, compressive stress-strain data for brittle materials.

15. SUBJECT TERMS

Brittle materials	Projectile
Indiana Limeston	Split Hopkinson pressure bar
Penetration mechanics	Strain rate effects

16. SECURITY CLASSIFICATION OF:

a. REPORT	b. ABSTRACT	c. THIS PAGE	17. LIMITATION OF ABSTRACT	18. NUMBER OF PAGES	19a. NAME OF RESPONSIBLE PERSON
UNCLASSIFIED		UNCLASSIFIED		177	19b. TELEPHONE NUMBER (include area code)